INSTITUTE FOR OIL SANDS INNOVATION AT THE UNIVERSITY OF ALBERTA
Breakthrough Energy Research | Advanced Environmental Technologies

Imperial ALBERTA INNOVATES FACULTY OF ENGINEERING

IOSI PROJECT FINAL REPORT

Project Number	IOSI 2016-12
Project Title	Development of a rapid screening method to screen and classify MFT
Project Budget and Tenure	$100,975 (USD) January 1, 2018 to June 30, 2019
Principal Investigators	Cliff Johnston Purdue University, West Lafayette, Indiana cliffjohnston@purdue.edu
HQP	Mohammadhasan Sasar
Industrial Stewards	Abu Junaid, CNRL Robert Mahood, Imperial
Report Prepared by	Cliff Johnston
Date	Sept 30, 2019

DISCLAIMERS

Alberta Innovates (AI) and Her Majesty the Queen in right of Alberta make no warranty, express or implied, nor assume any legal liability or responsibility for the accuracy, completeness, or usefulness of any information contained in this publication, nor that use thereof infringe on privately owned rights. The views and opinions of the author expressed herein do not necessarily reflect those of AI or Her Majesty the Queen in right of Alberta. The directors, officers, employees, agents and consultants of AI and the Government of Alberta are exempted, excluded and absolved from all liability for damage or injury, howsoever caused, to any person in connection with or arising out of the use by that person for any purpose of this publication or its contents.

The University of Alberta makes no warranty, express or implied, nor assumes any legal liability or responsibility for the accuracy, completeness, or usefulness of any information contained in this publication, nor that use thereof infringes on privately owned rights. The views and opinions of the author expressed herein do not necessarily reflect those of the University of Alberta. The directors, officers, employees, agents, students and consultants of the University of Alberta are exempted, excluded and absolved from all liability for damage or injury, howsoever caused, to any person in connection with or arising out of the use by that person for any purpose of this publication or its contents.

EXECUTIVE SUMMARY

The growing inventory of Mature Fine Tailings (MFT) is the focus of large-scale efforts to reduce the volume through a range of treatment options. Analysis of MFTs generally requires detailed and time-consuming laboratory analyses to obtain properties needed for effective tailings management. This project explored the application of a mid-infrared (mid-IR) method to rapidly screen and monitor mature fine tailings to predict key properties that including Methylene Blue Index (MBI), bitumen and solids content using chemometric methods. The overall objective was to evaluate and develop a rapid screening method to predict key MFT properties without having to send samples out for analysis that could take hours to weeks. The long-term goal would be to use this technique to rapidly monitor MFT processing streams to improve efficiency of tailings treatment including dosage of flocculants, coagulants, and mixing energies.

New methods are needed to rapidly screen the growing inventory of MFT and to assist with MFT monitoring during processing. The mid-IR method developed in this project analyzed 'as is' MFT slurries in < 60 seconds. Real-time and near real-time methods are needed to provide feedback about changes in MFT properties during various stages of flocculation and coagulation to deliver and monitor the optimum amount chemical additives and targeted MFT properties such as clay-to-water ratio. Because MFT is a complex assemblage of clay minerals, water and bitumen, no single monitoring technique (densitometer, X-ray fluorescence, near-infrared (NIR) spectroscopy) can provide all of the information of interest to achieve this goal. Mid-IR methods provide a potentially useful method to monitor multiple targets that include MBI, bitumen and solids content. This project examined the ability of mid-IR to predict MBI, bitumen and solids content. Within the realm of optical sensing methods, mid-IR offers the benefit of observing fundamental vibrations, compared to overtones and combination bands observed in the NIR.

In this project, a mid-IR (MIR) chemometric method using mid-infrared spectroscopy was developed to rapidly predict MBI, bitumen and solids content in less than 60 seconds. A large number of MFTs were evaluated (34 different MFTs) representing a broad range of MFT properties from representative sources (Muskeg River Mine (MRM), Jackpine Mine (JPM), Kearl and Suncor). Analysis of each MFT was replicated with each MFT analyzed more than 10 times. This provided a robust data set to develop the MIR-based chemometric model. The model was evaluated on the basis of root mean square error (RMSEV) from a validation data set. The RMSEV values were 0.8 (MBI), 0.4 wt. % bitumen, and 1.5 wt. % solids. RMSEV values have the same units of measure as the property being predicted. For example, the average MBI value was 9.9 meq/100g with an uncertainty of ± 0.8 meq/100g. For bitumen and solids content, the average bitumen content is 1.9 ± 0.4 wt % bitumen, and the average solid content is 26.6 ± 1.5 wt. % solids.

The key results for this project are presented in Section 4.5 where the Partial Least Squares (PLS) results for prediction of key MFT properties is presented. In brief, 34 MFTs were analyzed with strong replication (10x for each MFT). This provided a robust data set to develop the chemometric model and determine the mid-IR-based error of property prediction. The RMSEV values were 0.8 (MBI), 0.43 wt. % bitumen, and 1.53 wt. % solids. RMSEV values have the same units of measure as the property being measured. The average MBI value, bitumen and solids content were 9.9 meq/100g, 1.9 wt % bitumen, and 26.6 wt % solids, respectively.

TABLE OF CONTENTS

LIST OF FIGURES

LIST OF TABLES

1 INTRODUCTION

Project conception

In collaboration with Robert Mahood at Shell's Technology Centre in Calgary in 2015, I analyzed about 100 diverse samples (Albian Samples) using mid-IR (MIR) and thermal analysis methods. These samples had been heavily characterized using XRD, MBI and particle size methods. Upon examining this data set, good predictive ability was found for some properties (e.g., MBI and kaolinite content) using MIR. One limitation of the earlier MIR analysis of the Albian Samples was that all of the materials analyzed were dried materials. This project was developed to using adapted MIR methods, coupled with chemometrics, to analyze MFT suspensions.

The project objectives are as follows:

1. Obtain a suitable number of MFTs from various operators that would be representative of the variation of MFT properties overall.
2. Identify a suitable 'rapid screening method' (RSM).
3. Develop sampling protocols and collect statistically relevant RSM data from sourced MFTs.
4. Develop and optimize predictive chemometric models to predict MBI, bitumen and solids content.
5. Validation of chemometric models and determination of root mean square errors from this validation data set (RMSEV) for MBI, bitumen and solids content.

Relevance to the oil sands industry and IOSI research themes.

New methods are needed to rapidly screen the growing inventory of MFT and to assist with MFT monitoring during processing. Real-time and near real-time methods are needed to provide feedback about changes in MFT properties during various stages of flocculation and coagulation to deliver and monitor the optimum amount chemical additives and targeted MFT properties such as clay-to-water ratio. As MFT is a complex assemblage of clay minerals, water and bitumen, no single monitoring technique (densitometer, X-ray fluorescence, NIR) can provide all of the information of interest to achieve this goal. This project evaluated a mid-IR-based method to predict and monitor multiple targets that include MBI, bitumen and solids content.

Within the realm of optical sensing methods, mid-IR offers the benefits of observing fundamental vibrations of water, clay and bitumen, compared to overtones and combination bands observed in the NIR. The overall theme is directed at being able to rapidly (< 60 seconds) scan MFT in slurry form and predict and monitor MFT properties. This information is complementary to NIR analysis and the mid-IR method may provide some advantages in quantifying bitumen content, MBI and potentially being able to screen for mineralogy.

2 BACKGROUND

The oil sand ores of northern Alberta provide a significant portion of the overall energy portfolio for North America. The presence of clay minerals create significant challenges in all aspects of bitumen extraction and recovery, processing of oil sand ores, and management of tailings, which is the focus of this proposal. Current Hot Water Extraction process for pit-mined oil sands produces substantial amounts of Mature fine tailings (MFT), complex assemblages of clay minerals and related mineral phases, water, and bitumen (Farkish and Fall, 2013; Johnston, 2018; Mikula et al., 1996). The growing inventory of MFT, which is currently in excess of 10^9 cubic meters, has resulted in significant effort by the industry as a whole to develop new methods to reduce the volume of MFTs through the addition of polymeric flocculants, coagulants (e.g., alum, gypsum), combination of 'stacked technologies', in a wide range of engineering solutions that include thin-lift drying, centrifugation, and solid-liquid separation technologies to achieve reclamation goals. Tailings management requires analysis of MFTs that includes detailed and time-consuming laboratory analysis to obtain key properties such as water chemistry, bitumen and clay content, solids/clay/water contents, particle size, and clay mineralogy during processing. Chemical additives are expensive and must be delivered in such a way to achieve optimum water release. This project seeks to explore rapid measurement technologies that could be deployed in-line or on-site to monitor MFT changes during processing.

Over many years of detailed study, countless methods have been exploited to characterize the biogeochemical, mineralogical composition and rheological properties of mature fine tailings (FTFC (Fine Tailings Fundamentals Consortium), 1995; Wang et al., 2014; Yong and Sethi, 1978). Although a significant body of knowledge exists on the characterization of 'oil sands clay minerals', much of this work has relied focused on one particular dimension of characterization. For example, detailed mineralogical analysis investigations typically remove bitumen through Dean Stark extraction and analyze the samples dry powders. The goal of the project was to develop a rapid scanning method to examine MFT 'as is' in slurry form where both process water and fugitive bitumen are present and are quantification targets.

There has been tremendous growth in the area of chemometrics to predict properties of complex materials using optical methods (Esbensen et al., 2018). Since these methods were first developed in late 1960's in the field of econometrics (Geladi and Kowalski, 1986), these methods are now well established in many disciplines of chemical analysis. In brief, these methods apply statistical methods to look at complex data sets (e.g., optical spectra) to predict chemical properties. Application of these methods to tailings is not fully developed but are beginning to appear (Marrero et al., 2015; Martin et al., 2015; Mohseni et al., 2011).

Oil sands applications of these types of methods include efforts to analyze solvent diluted bitumen using NIR spectroscopy (Long et al., 2004), analysis of naphthenic acids in water using mass spectrometry (Grewer et al., 2010), online monitoring of bitumen conversion using mid-IR (Tefera et al., 2017), and the analysis of oil sands core samples and mine facies (Shchepetkina et al., 2017; Speta et al., 2015).

For oil sands tailings, Entezari and coworkers using NIR reflectance data to predict clay content and methylene blue indices (MBI) of tailings (Entezari et al., 2017a; Entezari et al., 2017b). In both of these papers, the samples were dried for up to a week prior to analysis. A similar approach of looking at dried materials was reported earlier (Johnston and Omotoso, 2013). In order to address the overall goal of this project, the current gap in knowledge is our understanding of the

characteristics of mature fine tailings in slurry form, especially in real time (as they exist in tailing ponds or in process streams).

3 EXPERIMENTAL

3.1 Materials

A total 34 MFTs were evaluated in this project from four different sources (MRM, JPM, Kearl and Suncor). The MFTs are listed in Table 4.1 and their properties are summarized in Tables 4.2 and 4.3. Chemical analysis data (MBI, wt % solids and bitumen) were provided by Canadian Natural Resources Limited (CNRL) (MRM and JPM samples), Imperial Oil (Kearl samples) and Suncor. The MBI values reported for the MRM and JPM samples used the UV-visible method, which are typically 15-20% higher compared to observer-dependent Halo Titration method. We acknowledge that not all of the MBI values were obtained using the same method and that the UV-visible data generally report larger MBI values. In addition, some analyses (solids and bitumen content and MBI) were conducted at Purdue on some samples. There was good agreement between the operator-supplied data and that collected at Purdue.

3.1.1 MFT sampling method

Given the heterogeneous nature of the MFTs, the tendency of this material to segregate during storage, and the small sample size required for many of the tests, it was necessary to develop procedures for consistent sampling of the MFTs. This procedure includes agitating the source using a Red Devil paint shaker for 5 minutes followed by transferring ~100 mL of MFT to a flask with a magnetic stir bar. The sample is mixed with the magnetic stirrer before an aliquot is used. This last step is particularly important because an oil sheen tends to form on the surface of MFTs while at rest which can reduce the repeatability of the spectra. These steps are illustrated in Figure 3.1. In addition, a detail SOP is included in Appendix1.

3.2 MFT characterization tests:

3.2.1 Solid content measurement:

In geotechnical engineering the dry weight of a given soil or slurry sample is traditionally obtained after oven drying at 110°C for 24 hours. The solid content is reported as the ratio of weight after oven drying to total weight. Some publications use solid content and mineral content interchangeably to refer to the mineral portion of the MFT. However, since oven drying does not result in evaporation of bitumen, the solid content in this document refers to the total solids (mineral and bituminous organics). When referring to the mineral portion of the slurry, the term mineral content is used.

3.2.2 Methylene Blue Index test:

The slurry method outlined by SGS Canada Inc. Oil sands was used to obtain repeatable methylene blue adsorption index (MBI) values. In this method, 0.006 M methylene blue in de-ionized water is titrated in 1 mL increments into a well-dispersed aqueous dispersion of MFT. A drop of the

solution is placed on a Whatman 42 ash less filter paper after each titration until a persistent blue halo is observed around the drop. The blue halo indicates the presence of free cations in the solution after the clay surface is saturated with methylene blue cations. The MBI value can be used to estimate the clay portion of the total minerals in MFT. This method was used to determine the MBI values for MFTs in group 1. To ensure consistency, we performed MBI test on S1730 and S1727. The results were as follows:

- S1730 (reported: 6.8, Measured: 6.9)
- S1727 (reported: 6.9, Measured: 7)

Given the tests performed at Purdue resulted in fairly close MBI to operator-supplied values, this test was not repeated for the all of the MFTs listed in Table 4.1.

3.2.3 Bitumen content:

Dean Stark method was used to determine the amount of bitumen (oil), water and solids. In this method, a known mass of material is refluxed by toluene in a Dean & Stark Soxhlet apparatus. The water from the sample is distilled and retained in a trap, while toluene is continuously condensed and recycled. The Dean Stark method outlined by the COSIA fines measurement working group (COSIA, 2014) is used in this document to report bitumen, water and mineral content as weight %. In other words, bitumen content is defined as the mass of bitumen over the total mass of the tailing. Dean stark test was performed on Suncor and MRM MFTs. Operator-supplied bitumen contents for the other MFTs were used (Table 4.1).

3.3 IR Spectroscopy:

Several FTIR sample presentation methods were evaluated in the preliminary portion of this project. These included diffuse reflectance (DR-FTIR), mid-IR and NIR transmission using a variable path length cell (VPLC), single bounce attenuated total reflectance (1BATR), and a nine-bounce horizontal trough ATR method. These are summarized briefly below.

3.3.1 Mid-IR and NIR spectroscopy

All spectra were obtained using a Thermo-Scientific Model 6700 FTIR spectrometer. In the mid-IR region, a liquid nitrogen cooled detector was used with a KBr beamsplitter. In general, 64 scans were obtained using an optical resolution of 4 cm^{-1} with a sampling interval of 2 cm^{-1}. For the NIR measurements, spectra were obtained using an InGaAs detector and a CaF_2 beamsplitter.

3.3.2 Diffuse Reflectance FTIR analysis

In this method, the MFT sample is first dried and pulverized using mortar and pestle. The resulting dry powder is then mixed with KBr in a 1:20 ratio, mixed using a wig-L-bug mixer. FTIR spectra are then collected and ratioed against a pure KBr sample. The main advantage of DR-FTIR is that it provides the most diagnostic information about the type of clays and bitumen present. The

disadvantages of DR-FTIR include (1) the pathlength is not well defined, (2) sample preparation procedure is time consuming, and most importantly (3) the samples must be dried.

3.3.3 Variable pathlength transmission cell

A variable pathlength transmission (VPT) cell was used in conjunction with both KBr and CaF_2 beamsplitters and MCT and InGaAs detectors to examine MFT in slurry form in both the mid-IR and NIR regions. Spectra were obtained at pathlengths ranging from 150 to 600 μm. Figure 3.2 shows the variable pathlength cell used for these measurements.

3.3.4 Single bounce attenuated total reflectance FTIR (ATR-FTIR):

A single reflection attenuated total reflectance FTIR (1BATR-FTIR) cell was used to analyze MFT (Figure 3.3). The internal reflection element in this cell is diamond which has excellent optical transmission from far-IR to NIR regions. As shown, a drop of an MFT slurry was placed on the crystal (Figure 3.3) and the spectra were ratioed against the spectrum of pure H_2O. The advantages of this cell are wide optical window and rugged diamond crystal. The disadvantage is the method lack sensitivity because it is a single bounce cell. Replication tests were not consistent with the cell.

3.3.5 Nine bounce HATR-FTIR analysis of MFTs.

Spectra were obtained using a 15-reflection horizontal trough attenuated total reflectance (HATR) cell using a ZnSe internal reflection element crystal at a 45 degree angle of incidence (Figure 3.4). The 'trough' of the HATR cell could hold a volume of about 2 mL and spectra were collected in the spectral region from 700 to 4000 cm^{-1}. In order to evaluation reproducibility, each HATR-FTIR test was replicated 10x.

3.4 Chemometrics

The collected spectra from HATR-FTIR were analyzed using Unscrambler X 10.5 (CAMO Software, Woodbridge, NJ). This software enabled us to analyse the data using Principal Component Analysis (PCA) and Partial Least Square (PLS) analysis. The data was analyzed both as is and after pre-processing techniques were used to refine the spectra for better modeling results. Pre-processing methods used included, multiplicative scatter correction (MSC), standard normal variate (SNV), orthogonal signal correction (OSC), 2^{nd} derivative in combination with Savitzky-Golay smoothing.

We have grouped all of the collected spectra in a dataset which is represented by a matrix of 344 rows and 1744 columns. Rows correspond to the different samples (MFTs) and columns correspond to the spectra as well as MFT characteristics, namely, MBI, solids and bitumen contents.

A total of six models were developed using the PLS algorithm with Unscrambler 9.0 (CAMO Software, Woodbridge, NJ) to identify the effects of different levels data preprocessing on prediction of solids contents, MBI and bitumen content. More information on how this dataset is split between calibration and validation datasets is presented in section 4.3.

4 RESULTS AND DISCUSSION

4.1 Preliminary spectral analysis of MFTs

Several spectroscopic methods were evaluated for this project which included DR-FTIR, 1BATR-FTIR in both the Mid-IR and NIR spectral regions, variable pathlength transmission studies in the NIR (VPT-NIR), and HATR-FTIR. The HATR-FTIR method was selected for this study and preliminary results from the other methods are discussed briefly below.

4.1.1 Diffuse Reflectance FTIR analysis

In prior work, we employed diffuse reflectance FTIR (DR-FTIR) to characterize MFTs and their interaction with polymeric flocculants (Johnston and Omotoso, 2013; Johnston et al., 2017). A representative DR-FTIR spectrum of MFT from Suncor's STP is shown in Figure 4.1. The main features include the ν(OH) and ν(SiO) stretching bands of the clay minerals present, the ν(CH) bands of bitumen and residual organics, and bands indicating the presence of water and carbonate. Replicated DR-FTIR spectra were collected for this project to evaluate the suitability of this method to meet project objectives. Replicated spectra of CNRL sample S1730 are shown in Figure 4.2 and a six-panel figure showing replicated spectra for samples S1725, S1727, S1729, S1730, S1731 and S1734 are shown in Figure 4.3. As shown in Figure 4.1, the spectral features of the clay minerals and bitumen and clearly observed. In this case, the diagnostic ν(OH) bands of kaolinite at 3695, 3668, 3652 and 3620 cm^{-1} are observed. The area of the ν(CH) bands in the 3100 to 2750 cm^{-1} region were integrated and ratioed against the area of the clay ν(OH) bands. This ratio is plotted against the bitumen contents of the samples in Figure 4.4 with a Pearson correlation coefficient of 0.89 and a p-value < 0.05 (significant at the 0.05 level). The advantage of this method is that clay and bitumen features are resolved. The disadvantages are that the sample must be dried, the distribution of bitumen is strongly heterogeneous, and the spectra do not reflect any information about percent solids. Thus, this method was ruled out as a potential Rapid Screening Method (RSM).

4.1.2 Single bounce attenuated total reflectance FTIR (ATR-FTIR) analysis of MFTs

We then focused only on methods that could be used with MFT suspensions 'as is'. The first method was the 1BATR method. In this case, a diamond internal reflection element (IRE) is used in the ATR cell is used with 45-degree incident geometry. The penetration depth is quite small (less than 10 microns). A schematic of this diagram is shown in Figure 4.5. The 'as received' (wet) slurry of S1730 is shown by the blue trace in Figure 4.6. This spectrum 'looks' different from the DR-FTIR spectra shown in Figures 4.1-3 due to the presence of water. The strong bands at 3400 and 1630 cm^{-1} are due to the presence of H_2O and correspond to the ν(OH) and δ(H-O-H) bands of H_2O. The ν(CH) and δ(CH_2) deformation bands of bitumen are present. Weak ν(SiO) bands are present in the slurry spectrum (blue trace). Upon drying the sample, the H_2O bands are lost and the clay bands become prominent in the ν(OH) and ν(SiO) regions (red trace). The bitumen bands

have essentially the same intensity in the wet versus dry spectra (Figure 4.6). Replicated spectra of samples S1730 are shown in Figures 4.7 and 4.8. The spectra showed poor reproducibility. Depending the sample, the ν(OH) intensity varied from 0.32 to 0.40 and the bitumen bands in the ν(CH) region showed strong to almost no absorbance. Because of the heterogeneous distribution of bitumen, spectra are quite variable even among replicates of the same sample. ATR-FTIR spectra of six MFTs are shown in Figure 4.9. The bitumen contents of these samples ranged from 1.6 to 2.4% bitumen. The spectra showed poor correlation with bitumen content. The 1BATR-FTIR method was not viewed to be a viable method going forward due to poor reproducibility.

4.1.3 1BATR study of MFT in the NIR

Combined MIR and NIR spectra of sample ES2790 are shown in Figure 4.10. These spectra are shown in Figure 4.11 in both the MIR (Figure 4.11A) and NIR (Figure 4.11B). Although spectral features are shown out to 7500 cm^{-1}, NIR features are very weak – showing only spectra features of H_2O. This is because the pathlength of the 1BATR-FTIR cell is < 10 microns. This method does show the relative intensity differences between the fundamental vibrations in the MIR and the overtone and combination bands observed in the NIR (Figure 4.10). This method lacks sensitivity and was ruled out as a potential RSM.

4.1.4 Near-IR analysis of slurry MFTs in a variable pathlength transmission cell.

A variable pathlength transmission (VPT) cell was used in conjunction with a CaF_2 beamsplitter and a InGaAs detector to examine MFT in the NIR region. VPT-NIR spectra of H_2O in the 4000 to 11000 cm^{-1} region are shown in Figure 4.12A. The intensity of the 6902 cm^{-1} H_2O band was plotted versus the pathlength of the cell showing a highly correlated Beer's law response (Figure 4.12B). VPT-NIR spectra of sample S1729 are shown in Figures 4.13A-C. Spectra were obtained at pathlengths ranging from 150 to 600 μm. Using the longer pathlengths, clay features are also observed at 4530 and 7000 cm^{-1}. This method was not viewed as a viable method going forward because loading the samples into the cell was complicated, cleaning the cell between samples was difficult, and establishing a consistent pathlength was challenging.

4.1.5 9 bounce HATR-FTIR analysis of MFTs.

HATR spectra of MFT were obtained using the cell shown in Figure 3.4. Replicated HATR-FTIR spectra of sample ES2356 are shown in Figure 4.14. The spectra are qualitatively similar to the 1BATR-FTIR spectra of MFT discussed in Section 4.1.2 and in Figure 4.6. In general, reproducibility of the HATR-FTIR spectra was quite good. A total of 10 spectra are overlaid in Figure 4.14 in gray and their average is shown by the black trace. Similar results were obtained on all 34 of the MFT samples received (Appendix III). 'As is' spectra of MFTs could be obtained in less than 60 seconds. Cleaning the cell was relatively easy and a total of at least 10 replicates were obtained by repeated sampling, cleaning and sample presentation. Because the spectra were highly reproducible, the HATR method was selected as the RSM for this project.

4.2 Selected properties of mature fine tailings (MFTs)

Selected properties of the 34 MFTs investigated in this project are listed in Table 4.1. Descriptive statistics of the selected properties are listed in Tables 4.2 and 4.3. The mean weight percent solids is 26.6% with a standard deviation (σ) of 7.8. The mean MBI value is 9.9 (σ = 2.5) and the mean weight percent bitumen is 1.9 (σ = 1.3). Figure 4.15 presents a histogram and normal distribution curve (upper portion) and box plot (lower portion) for weight percent solids. Similar plots are shown for MBI and weight percent bitumen in Figures 4.16 and 4.17. Based on the box plots shown in Figures 4.15 and 4.17, the Pond 2/3 sample is an outlier (outside of the 5-95th percentile range) for both weight percent solids and weight percent bitumen.

4.2.1 Selected spectral comparisons

Prior to conducting chemometric analysis, it is useful to compare selected pairings of HATR-FTIR spectra to observe what spectral regions are influenced by the property in question. Figure 4.18 compares the HATR-FTIR spectra of the samples with the lowest (ES4368) and highest (Pond 2/3) weight percent solids content. The ES4368 spectrum has the highest intensity in the ν(OH) region around 3400 cm^{-1} and the lowest intensity in the ν(SiO) region around 1000 cm^{-1}. In contrast, Pond 2/3 has the highest intensity in the ν(SiO) region and a slightly lower intensity in the ν(OH) region. These observations are expected as samples with the highest weight percent solids would be expected to have the highest intensity of the ν(SiO) bands. Figure 4.19 compares the sample with the highest MBI (ES2356) to the lowest MBI values (ES4372). In this case, the spectra are quite similar. For weight percent bitumen (Figure 4.20), the high-bitumen content spectrum (Pond 2/3) has discernable features in the ν(CH) region around 3000-2800 cm^{-1} and in the –CH2 deformation region between 1350-1500 cm^{-1}. These features are absent in the low-bitumen samples (FFT#3).

Based upon this 'visual' analysis, weight percent solids is expected to be directly proportional to the intensity of the ν(SiO) bands and inversely proportional to the intensity of the ν(OH) bands of H_2O. Weight percent bitumen is expected to be proportional to intensity in the ν(CH) region. There were no clear spectral regions visible 'by eye' that were apparent between the low- and high-MBI spectra. This is not uncommon in PCA / PLS modeling of complex mixtures where property prediction occurs in spectral regions throughout the spectrum.

4.3 Chemometric modeling – organizing the data.

For both principal component analysis (PCA) and partial least square (PLS) modeling, the collected spectra were organized into two calibration and two validation data sets. The overall project collected 344 spectra obtained from 34 different MFTs. Each MFT was analyzed a minimum of 10 times. Chemometric modeling relies heavily upon having a representative set of data to validate the model. Two approach were used to achieve this goal. In **Set 1**, the 1st, 2nd, 4th, 5th, 7th, 8th, and 10th samples for a given MFT was used as calibration files. The 3rd, 6th and 9th samples were used as validation files. This resulted in 244 calibration files and 100 validation files. This data set was 'reduced' into **Set 2** by averaging calibration samples for a given MFT into a single sample (the average of the 1st, 2nd, 4th, 5th, 7th, 8th, and 10th samples). Similarly, the 3rd, 6th and 9th replicates were averaged into single validation files. Thus, in **Set 2** there were 34 calibration samples and 34 validation samples. This organization is shown in Figure 4.21 where each labeled box (e.g., S1725) represents on MFT listed in Table 3.1. In **Set 1** each yellow cell corresponds to

one replicated sample used as a calibration file. Similarly, each gold shaded cell corresponds to one replicated sample used as a validation file. The source of each MFT is represented by the background shading indicating the source of the MFT (MRM, JPM, Suncor or Kearl). **Set 2** was obtained by averaging each of the yellow cells into one sample to be used as a calibration file, and each gold cell was averaged into one sample to be used as a validation file.

4.4 Principal component analysis (PCA) of MFTs

Principal component analysis (PCA) was used to analyze data **Set 1** and **Set 2.** PCA results for data **Set 1** (244 calibration and 100 validation files) are shown in Figure 4.22 where 96.9% of the variability was explained using 4 principal components. Several pretreatments, including multiplicative scatter correction (MSC), standard normal variate (SNV), and 2nd derivative + SNV were evaluated. The PCA results for both Set 1 and Set 2 are summarized in Table 4.3. In terms of goodness of fit, the MSC correction applied to the reduced data set, accounting for 97.6% of variation using 3 principal components, was the best model. Keep in mind there is a trade-off between the number of factors and the percent variability accounted for. The goal is to account for the maximum percent variability using the smallest number of factors. A PCA plot showing the results for Set 1 are shown in Figure 4.23; the results for Set 2 are shown in Figure 4.24. The samples show clear groupings among the difference MFT sources. PCA is a type of qualitative exploratory data analysis (EDA) and can be used to reveal the hidden structure within large data sets. Overall, the positive results obtained here provide justification for additional quantitative chemometric analysis using the Partial Least Square (PLS) method. It is useful to examine the first two principal components of **Set 2** shown in Figures 4.25-4.26, respectively. The first principal component (Figure 4.25), accounts for about 65% of variability, shows strong positive clay bands and negative water bands. Meaning, a positive score is a sample with high clay/solids content and low water content. The second principal component (Figure 4.26) shows positive bitumen features and negative clay features. The overall performance of the PCA model using various pre-processing methods are summarized in Figures 4.27-4.28.

4.5 Partial Least Squares (PLS) analysis of MFT

4.5.1 Prediction of solids content

The PCA results showed that there was sufficient variation among the HATR-FTIR spectra of the different MFTs to warrant analysis of the data using partial least squares (PLS). Partial Least Squares Regression (PLSR), also sometimes referred to as Projection to Latent Structures or just PLS, models both the X- (spectra) and Y-matrices (MFT properties) simultaneously to find the *latent (or hidden)* variables in X (spectra) that will best predict the latent variables in Y (MFT properties). These PLS components are similar to principal components and will be referred to as *factors.* In PLS, a 'predicted versus reference plot' shows the overall performance of the model. Because the model builds a relationship based on a 'leave one out' method, all PLS modeling was based on **Set 2**. Using PLS to model **Set 1** is not justified because only one of 10 replicates would be 'left out'.

The predicted versus reference plot from **Set** 2 for prediction of weight % solids is shown in Figure 4.29. The model used no sample pre-treatment (raw spectra) and the model recommended use of 4 factors. The model was evaluated on the basis of the validation data set shown by the red data points. In this case, the goodness of fit criteria were a R^2 value of 0.92 and a root mean square

error of the validation (RMSEV) data of 2.16 weight % solids. RMSEV values have the same units of measure as the property being predicted. Results for several pretreatments are presented in Table 4.5. Prediction of weight % solids using the different pre-processing treatments is summarized in Figure 4.30. The highest R^2 value (0.96) and lowest RMSEV value (1.53 wt% solids) was obtained using an orthogonal signal correction (OSC) using 5 factors. The predicted versus reference plot using OSC is shown in Figure 4.31. These results can be understood on the basis of RMSEV. The average weight percent solids of the 34 MFTs was 26.6 % with 1.53 RMSEV..

4.5.2 Prediction of MBI

The predicted versus reference plot from **Set** 2 for prediction of MBI is shown in Figure 4.32. This model using an OSC pre-processing step and 4 factors. The model was evaluated on the basis of the validation data set shown by the red data points. In this case, the goodness of fit criteria were a R^2 value of 0.90 and a root mean square error of the validation (RMSEV) data of 0.8 meq/100 g. Results for several pretreatments are presented in Table 4.6 and in Figure 4.33. The average MBI value of the 34 MFTs was 9.9 with an RMSEV of 0.8.

4.5.3 Prediction of bitumen content

The predicted versus reference plot from **Set** 2 for prediction of weight % bitumen is shown in Figure 4.34. This model used OSC and 4 factors which was similar to results obtained using the 2^{nd} derivative GapSeg 7-5 using 6 factors (Figure 4.35). The model was evaluated on the basis of the validation data set shown by the red data points. In this case, the goodness of fit criteria were a R^2 value of 0.89 and a root mean square error of the validation (RMSEV) data of 0.43 wt. % bitumen. Results for several pretreatments are presented in Table 4.7 and in Figure 4.35. The average wt. % bitumen is 1.9 with an RMSEV of 0.43.

To summarize all results: a large number of MFTs were evaluated (34 different MFTs) representing a broad range of MFT properties from representative sources (MRM, JPM, Kearl and Suncor). Analysis of each MFT was replicated with each MFT being analyzed more than 10 times. This provided a robust data set to develop the chemometric model and determine the mid-IR-based error of property prediction. The model was evaluated on the basis of root mean square error from a validation data set (RMSEV). The RMSEV values were 0.8 (MBI), 0.4 wt. % bitumen, and 1.5 wt. % solids. RMSEV values have the same units of measure as the property.

5 CONCLUSIONS AND RECOMMENDATIONS

5.1 Conclusions

A new rapid screening mid-IR method was developed to rapidly screen and predict key MFT properties based on analysis and benchmarking of 34 different MFTs. A high degree of replication (10x) was used and resulted in robust calibration and validation data sets. Key results were prediction of MBI, weight % bitumen, and weight % solids with RMSEV values of 0.8, 0.4 and 1.53, respectively (same as units of measure). Mid-IR is a complementary method to NIR and may offer some advantages in detecting bitumen and differences in clay mineralogy,

possibly water quality. The key advance represented by this study was a detailed analysis of 'as supplied' MFTs in suspension form. Much of the prior methodology examined samples which had been dried. In this study, spectra and sampling methods were developed to rapidly analyze MFT suspension that showed high reproducibility and consistent results using both PCA and PLS methods.

5.2 Recommendations for Future Work

This project developed a laboratory mid-IR method to rapidly predict MBI, bitumen and solids content. In a related COSIA-member sponsored work, NIR methods and instrumentation is being developed. Mid-IR and NIR are complementary methods with each method having a unique set of advantages and disadvantages. NIR data can be collected 'remotely' with fiber optic sensing up to 35 meters.

Recommendations

1. Conduct a direct comparison of on-line NIR and on-site mid-IR methods using the same samples. Because mid-IR methodologies measure fundamental vibrations, these methods may provide improved predictability of MBI and bitumen content over NIR.
2. Explore recent advances to develop 'in line' and fiber optic sensing for mid-IR analysis.
3. This project focused on 3 MFT properties: MBI, bitumen and solids content. Because the clay bands are readily observed in the mid-IR, explore the ability of this method to monitor changes in clay mineralogy (e.g., kaolinite-to-illite ratio).

6 ACKNOWLEDGEMENTS

Cliff Johnston would like to acknowledge the numerous helpful conversations with Abu Junaid and Robert Mahood, and the generous financial support provided by IOSI and COSIA.

7 HIGHLY QUALIFIED PERSONNEL TRAINED

This project supported one Ph.D. student in geotechnical engineering at Purdue University. Mohammadhasan Sasar.

8 REFERENCES

Entezari, I., Rivard, B., Geramian, M., Lipsett, M.G., 2017a. Predicting the abundance of clays and quartz in oil sands using hyperspectral measurements. Int. J. Appl. Earth Obs. Geoinf. 59, 1-8.

Entezari, I., Rivard, B., Lipsett, M.G., 2017b. Estimation of methylene blue index in oil sands tailings using hyperspectral data. Canadian Journal of Chemical Engineering 95, 92-99.

Esbensen, K.H., Swarbrick, B., Westad, F., 2018. Multivariate data analysis. An introduction of multivariate analysis, process analytical technology and quality by design, 6th ed. CAMO Software.

Farkish, A., Fall, M., 2013. Rapid dewatering of oil sand mature fine tailings using super absorbent polymer (SAP). Minerals Engineering 50-51, 38-47.

FTFC (Fine Tailings Fundamentals Consortium), 1995. Advances in oil sands tailings research. Alberta Department of Energy.

Geladi, P., Kowalski, B.R., 1986. Partial Least-Squares Regression - A Tutorial. Analytica Chimica Acta 185, 1-17.

Grewer, D.M., Young, R.F., Whittal, R.M., Fedorak, P.M., 2010. Naphthenic acids and other acid-extractables in water samples from Alberta: What is being measured? Science of the Total Environment 408, 5997-6010.

Johnston, C.T., 2018. Surface chemistry of oil-sands clay minerals, in: Omotoso, D., Hockley, D. (Eds.), Introduction to Oil Sands Clays. The Clay Minerals Society, Chantilly, VA, pp. 33-60.

Johnston, C.T., Omotoso, O., 2013. Baseline Studies of the Surface Chemistry of Oil Sands Clay Minerals. Final report submitted to CONRAD in 2013.

Johnston, C.T., Santagata, M., Bobet, A., Sasar, M., 2017. Polymer-MFT Interactions: from surface chemistry to rheology.

Long, Y.C., Dabros, T., Hamza, H., 2004. Analysis of solvent-diluted bitumen from oil sands froth treatment using NIR spectroscopy. Canadian Journal of Chemical Engineering 82, 776-781.

Marrero, J., Coto, O., Goldmann, S., Graupner, T., Schippers, A., 2015. Recovery of Nickel and Cobalt from Laterite Tailings by Reductive Dissolution under Aerobic Conditions Using Acidithiobacillus Species. Environmental Science & Technology 49, 6674-6682.

Martin, M., Janneck, E., Kermer, R., Patzig, A., Reichel, S., 2015. Recovery of indium from sphalerite ore and flotation tailings by bioleaching and subsequent precipitation processes. Minerals Engineering 75, 94-99.

Mikula, R.J., Kasperski, K.L., Burns, R.D., MacKinnon, M.D., 1996. Nature and fate of oil sands fine tailings. American Chemical Society, Washington DC.

Mohseni, S., Marzban, A., Sepehr, S., Hosseinkhani, S., Karkhaneh, M., Azimi, A., 2011. Investigation of some heavy metals toxicity for indigenous Acidithiobacillus ferrooxidans isolated from Sarcheshmeh copper mine. Jundishapur Journal of Microbiology 4, 159-166.

Shchepetkina, A., Speta, M., Gingras, M.K., Rivard, B., Pemberton, S.G., 2017. Hyperspectral imaging as an aid for facies analysis in massive-appearing sediments: a case study from the middle McMurray Formation. Bulletin of Canadian Petroleum Geology 65, 262-278.

Speta, M., Rivard, B., Feng, J.L., Lipsett, M., Gingras, M., 2015. Hyperspectral imaging for the determination of bitumen content in Athabasca oil sands core samples. Aapg Bulletin 99, 1245-1259.

Tefera, D.T., Agrawal, A., Jaramillo, L.M.Y., de Klerk, A., Prasad, V., 2017. Self-Modeling Multivariate Curve Resolution Model for Online Monitoring of Bitumen Conversion Using Infrared Spectroscopy. Industrial & Engineering Chemistry Research 56, 10756-10769.

Wang, C., Harbottle, D., Liu, Q.X., Xu, Z.H., 2014. Current state of fine mineral tailings treatment: A critical review on theory and practice. Minerals Engineering 58, 113-131.

Yong, R.N., Sethi, A.J., 1978. Mineral particle interaction control of tar sand sludge stability. Journal of Canadian Petroleum Technology 17, 76-83.

9 LIST OF PUBLICATIONS AND PATENT FILING/APPLICATION

Surface and Interface Chemistry of Clay Minerals. Schoonheydt R, Johnston CT, Bergaya F, editors. Developments in Clay Science. 9: Elsevier; 2018. p. 1-420 pages. ISBN 978-0-08-102432-4.

Schoonheydt RA, Johnston CT, Bergaya F. 1 - Clay minerals and their surfaces. In: Schoonheydt R, Johnston CT, Bergaya F, editors. Developments in Clay Science. 9: Elsevier; 2018. p. 1-21.

Johnston CT. 4 - Clay mineral–water interactions. In: Schoonheydt R, Johnston CT, Bergaya F, editors. Developments in Clay Science. 9: Elsevier; 2018. p. 89-124.

Johnston CT. Surface chemistry of oil-sands clay minerals. In: Omotoso D, Hockley D, editors. Introduction to Oil Sands Clays. CMS Workshop Lectures. 22. Chantilly, VA: The Clay Minerals Society; 2018. p. 33-60.

Johnston CT. Infrared studies of clay mineral-water interactions. In: Gates WP, Kloprogge JT, Madejova J, Bergaya F, editors. Infrared and Raman spectroscopies of clay minerals. Developments in Clay Science. 8. Amsterdam: Elsevier; 2017. p. 288-309.

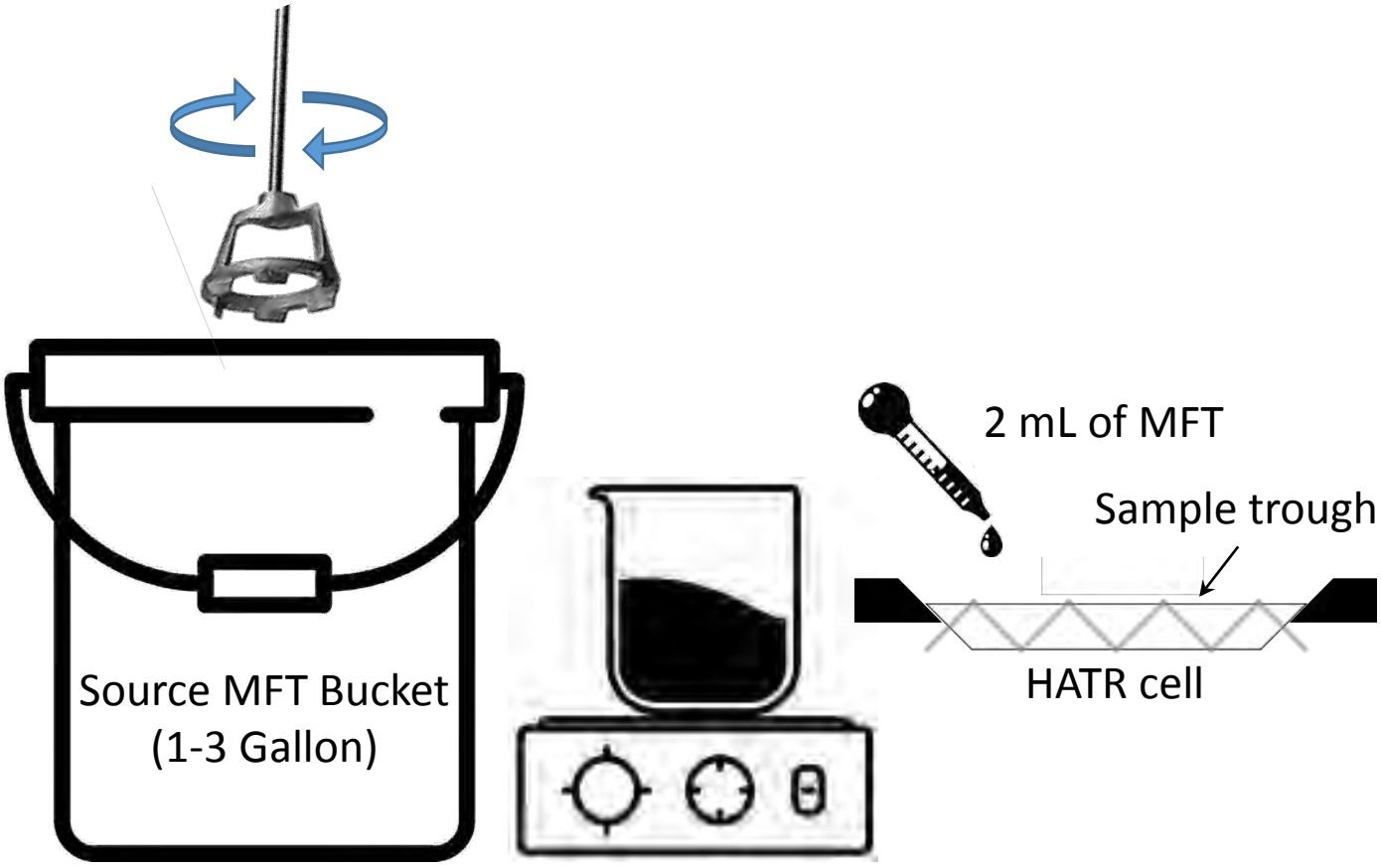

Figure 3.1 Sketch of subsampling method for the HATR-FTIR method which includes using a magnetic stirrer to ensure homogenous subsampling and a pipette to transfer MFT onto HATR trough

Variable Pathlength Cell (VPC)

Figure 3.2 Variable Pathlength Cell (VPC). By rotating the outer "sleeve" the pathlength range can be adjustable from a (theoretical) minimum of 0.00mm to 6.000mm maximum in increments of 0.005mm. A Vernier scale indicator helps keep track of the pathlength (the distance between the two windows of the VPLC that contains the fluid).

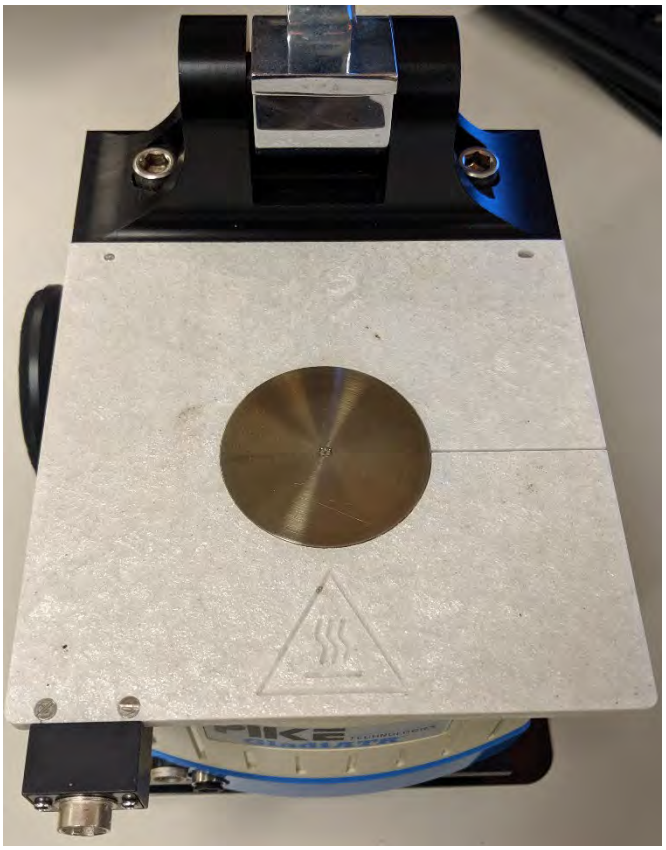

Figure 3.3 Gladi-ATR cell. Clean empty cell on the left. Zoomed in view of the cell window with a drop of MFT on the window ready to collect sample spectrum (top right).

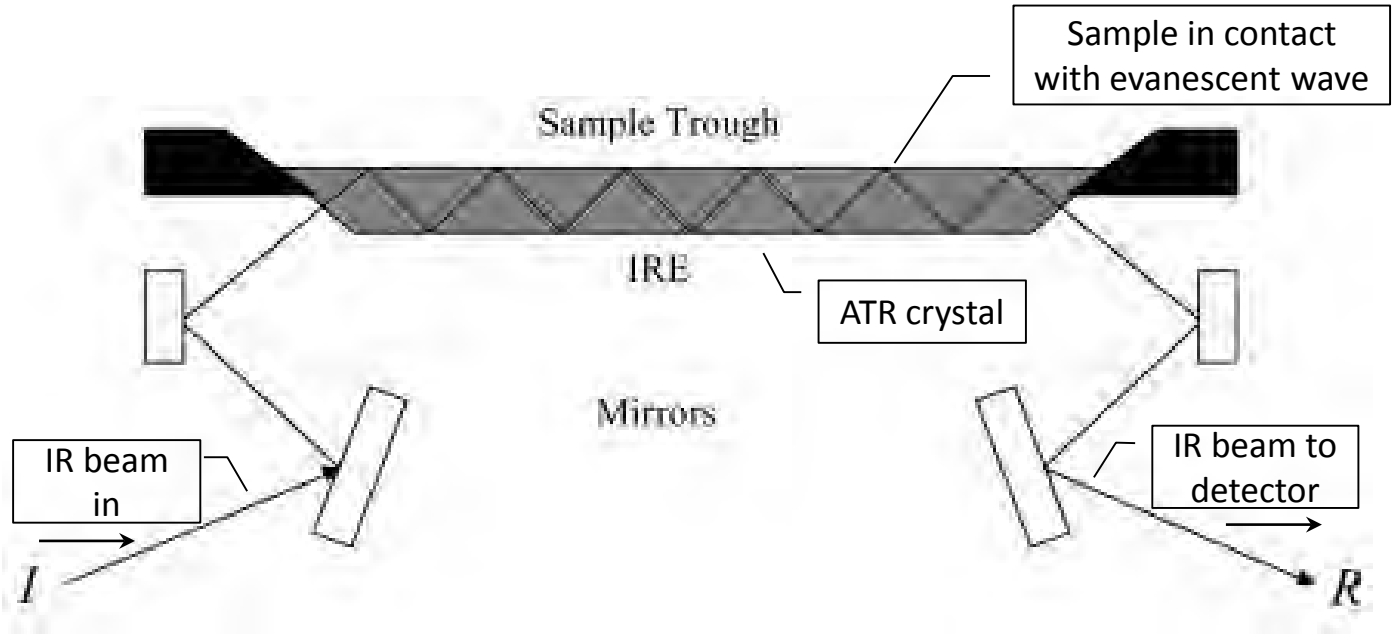

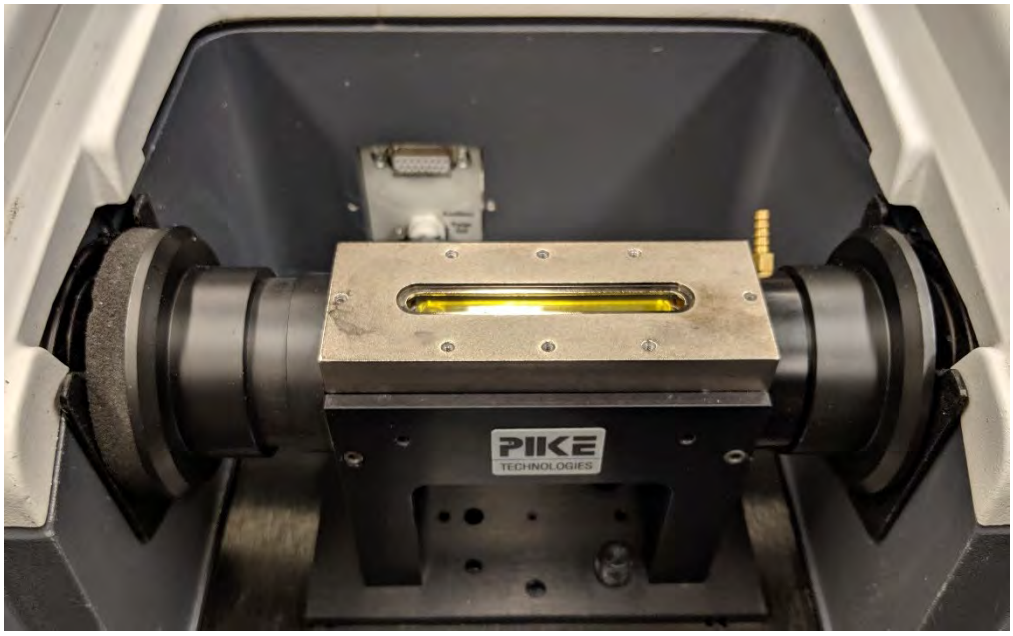

HATR cell setup cleaned and ready for the collection of background spectra

Figure 3.4 Horizontal trough ATR cell. Cell geometry was a 45 degree angle of incidence and a ZnZe IRE was used. Approximately 2 mL of MFT was paced in the cell with a total pathlength of about 12 microns .

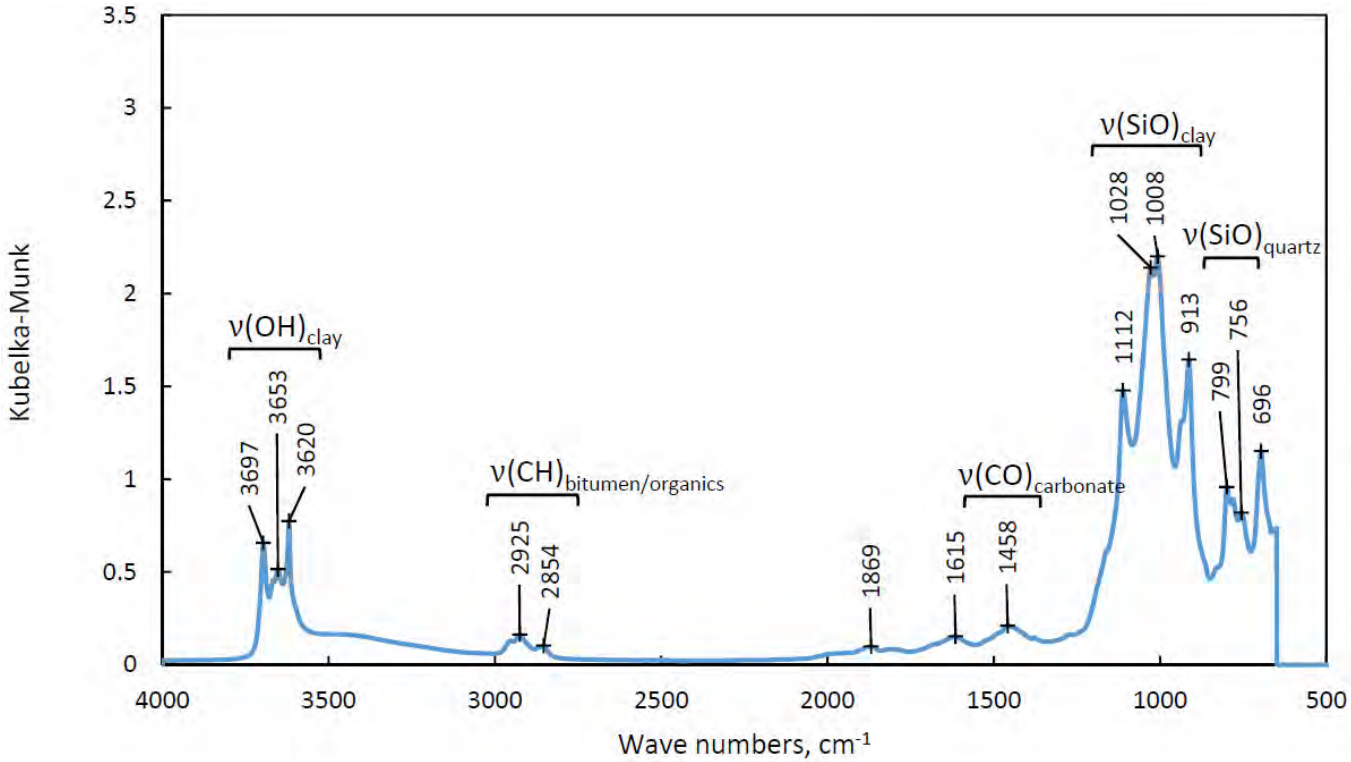

Figure 4.1 DR-FTIR spectrum of dried MFT (STP) in the 4000 to 700 cm-1 region. Vibrational bands of the clay constituents are observed in the O-H stretching and Si-O stretching regions, residual bitumen is observed in the C-H stretching region. Additionally, bands are observed indicating the presence of quartz and carbonates. Water was removed from this sample prior to analysis and this spectrum does not show the presence of H_2O.

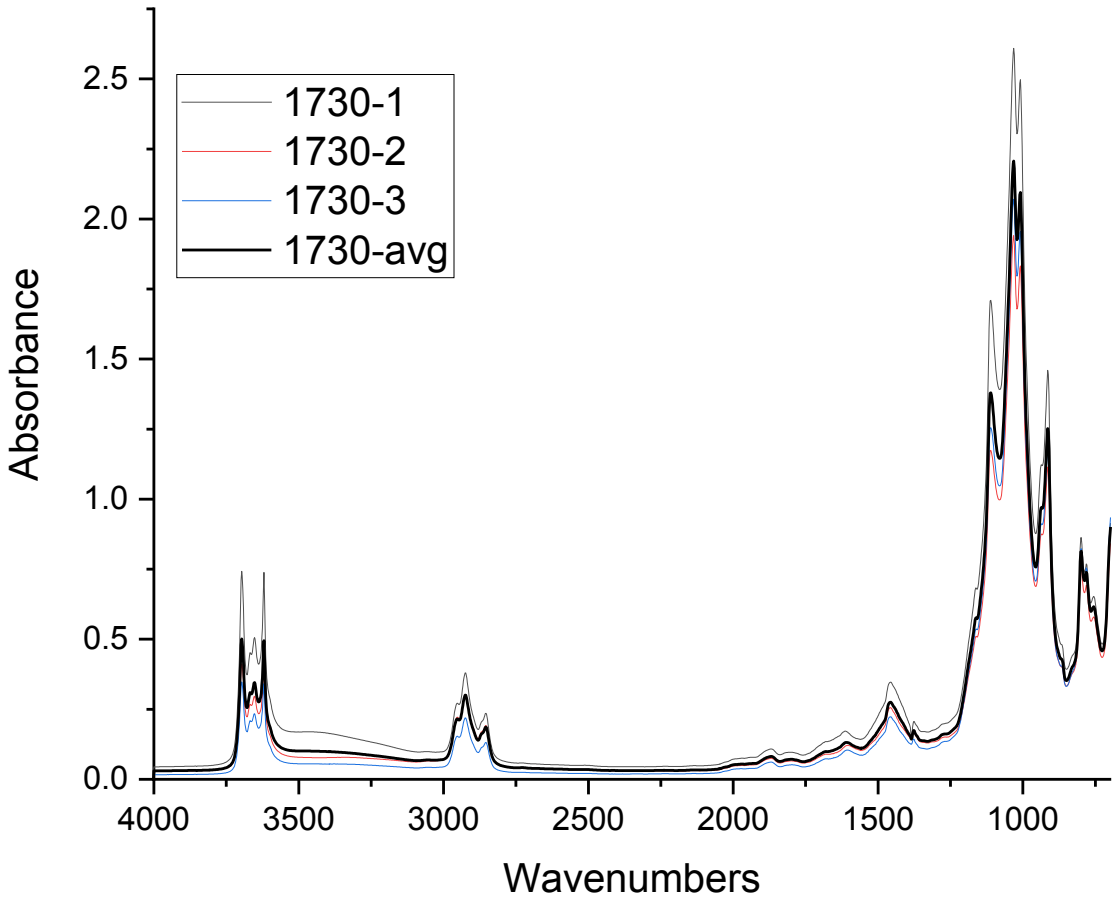

Figure 4.2 DR-FTIR spectrum of sample S1730. Three replicated spectra are shown along with the average of the three files (bold black curve) in 4000 to 700 cm-1 region.

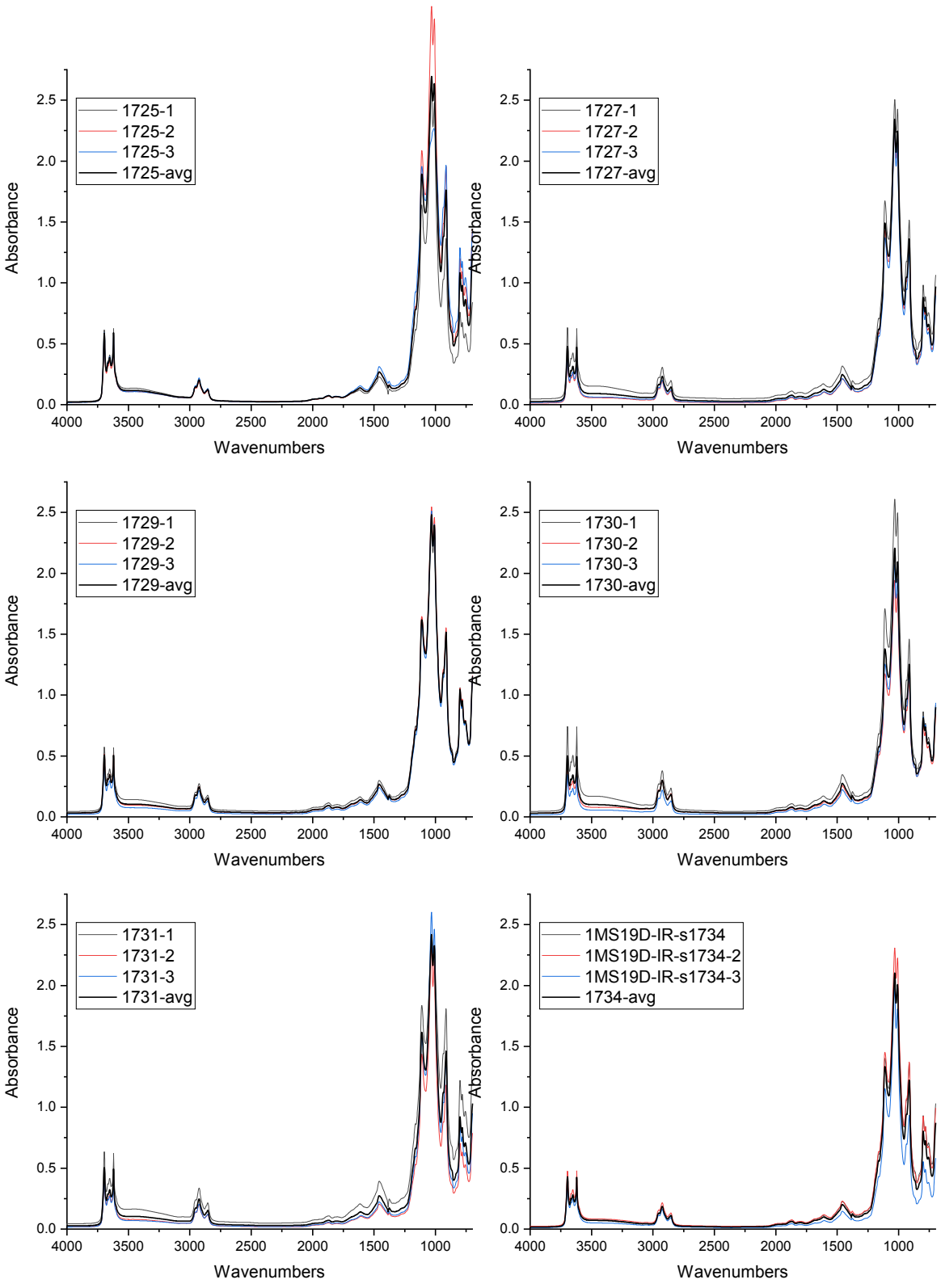

Figure 4.3 Six panel composite plot – showing samples 1725, 1727, 1729, 1730, 1731, and 1734 in the 4000 to 700 cm-1 region.

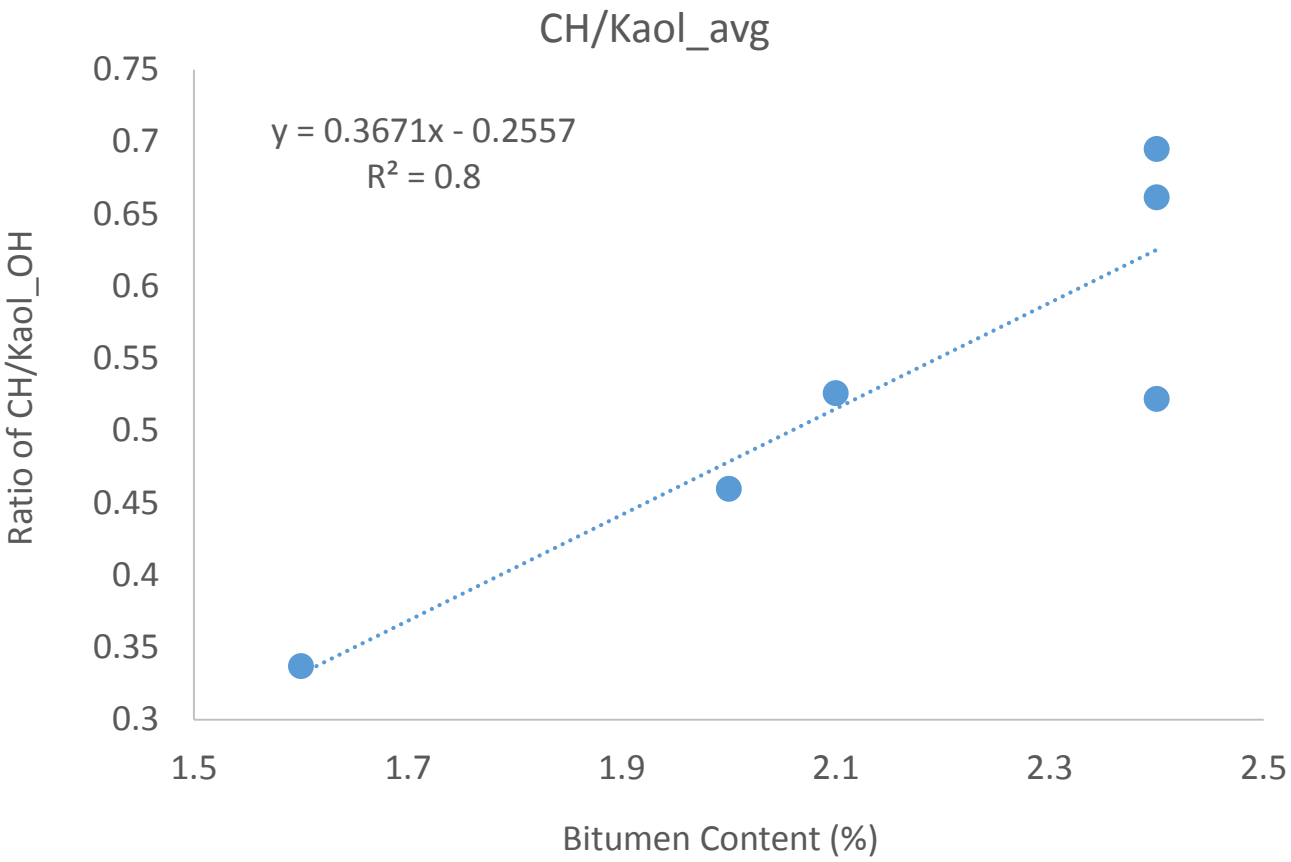

Figure 4.4 Plot of the spectral area ratio of (CH/Kaol) bands from the DR-FTIR spectra to bitumen content.

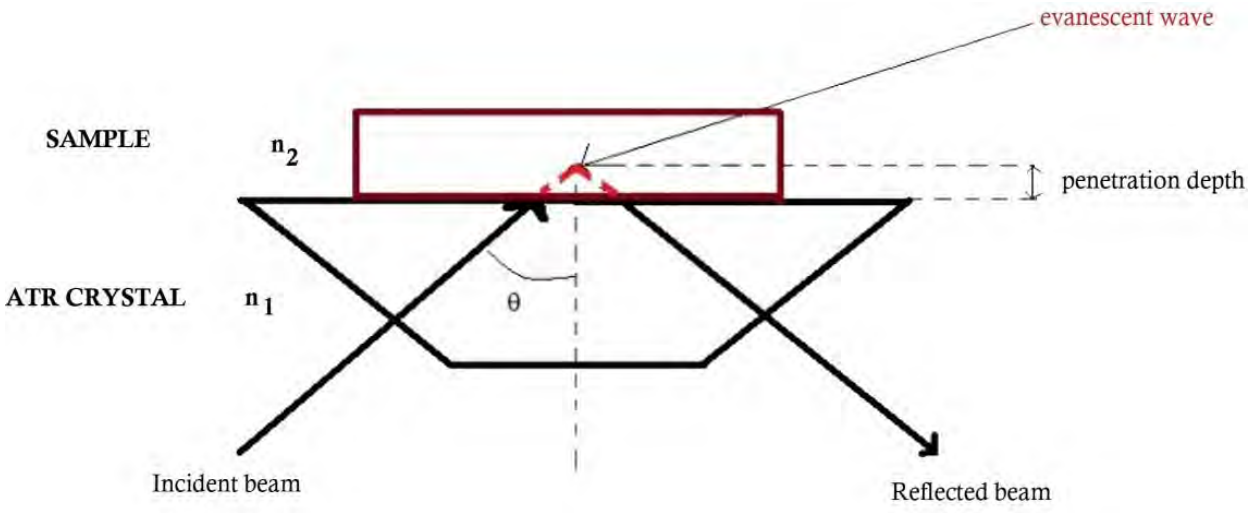

Figure 4.5 Schematic diagram of a horizontal ATR sampling accessory illustrating the important parameters (Simonescu, 2012).

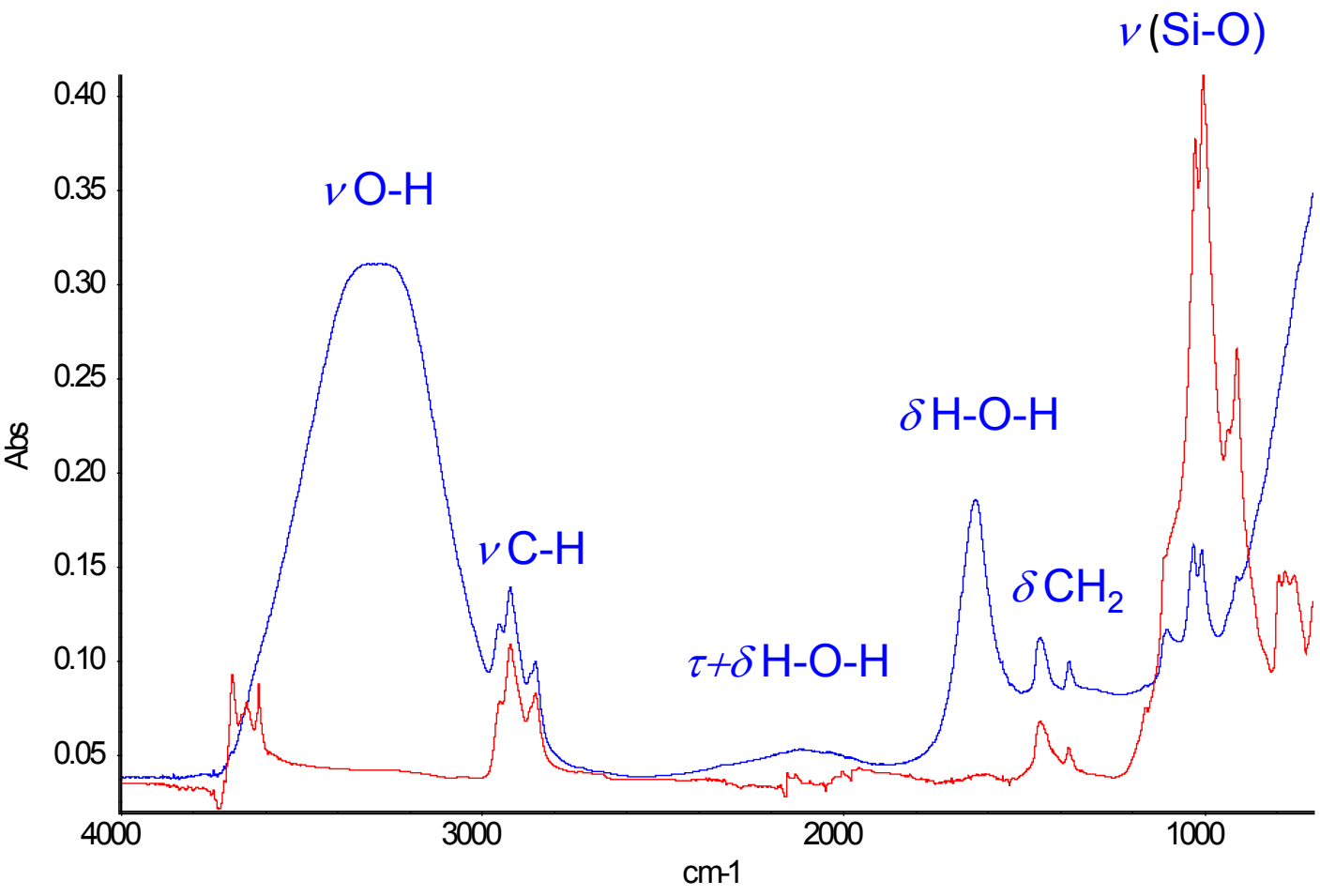

Figure 4.6 Gladiator ATR-FTIR spectra of sample 1730 in the wet (blue) and dry (red) state in 4000 to 700 cm-1 region.

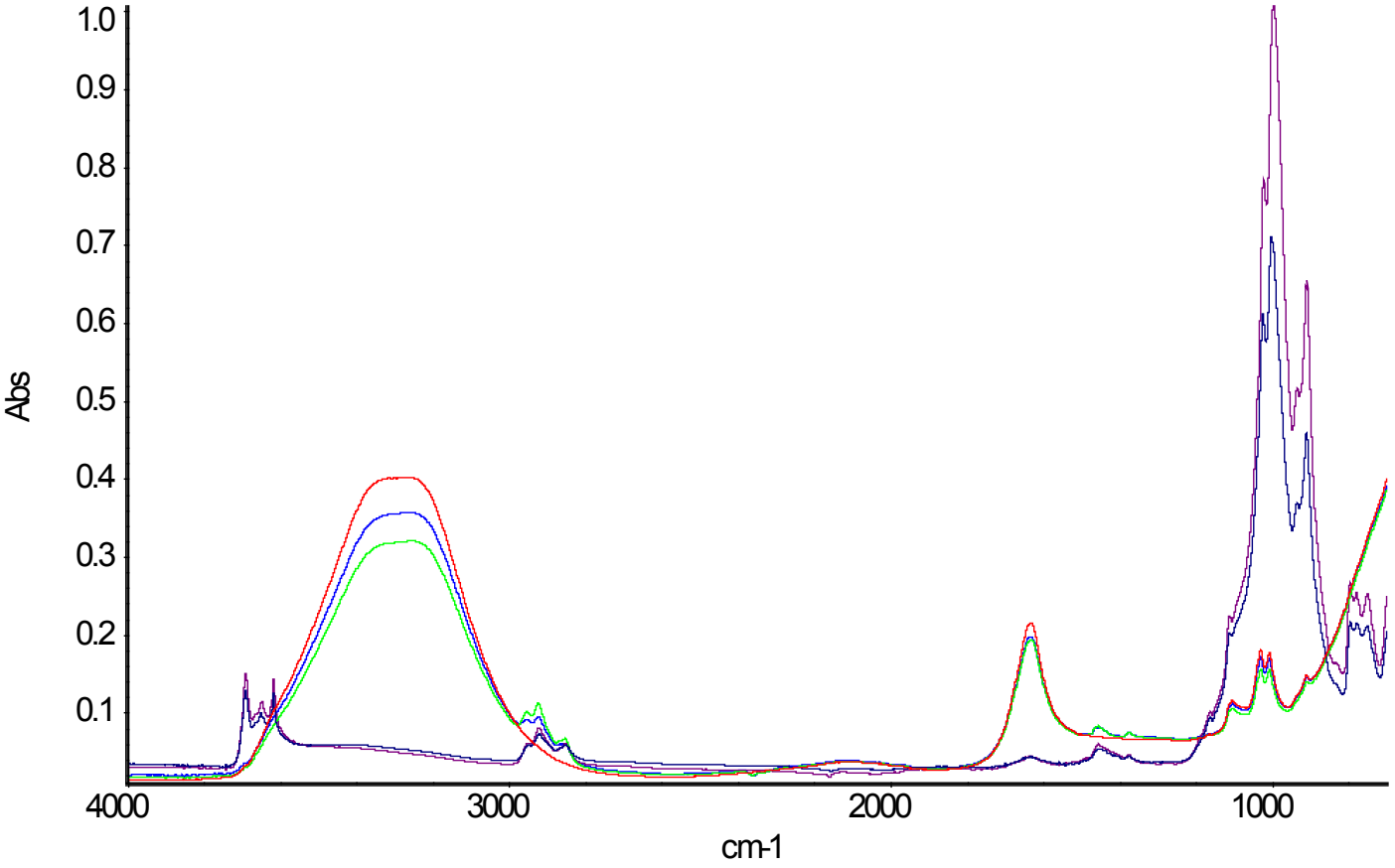

Figure 4.7 Gladiator ATR-FTIR spectra of replicated spectra for sample 1730 in the wet and dry state in 4000 to 700 cm-1 region.

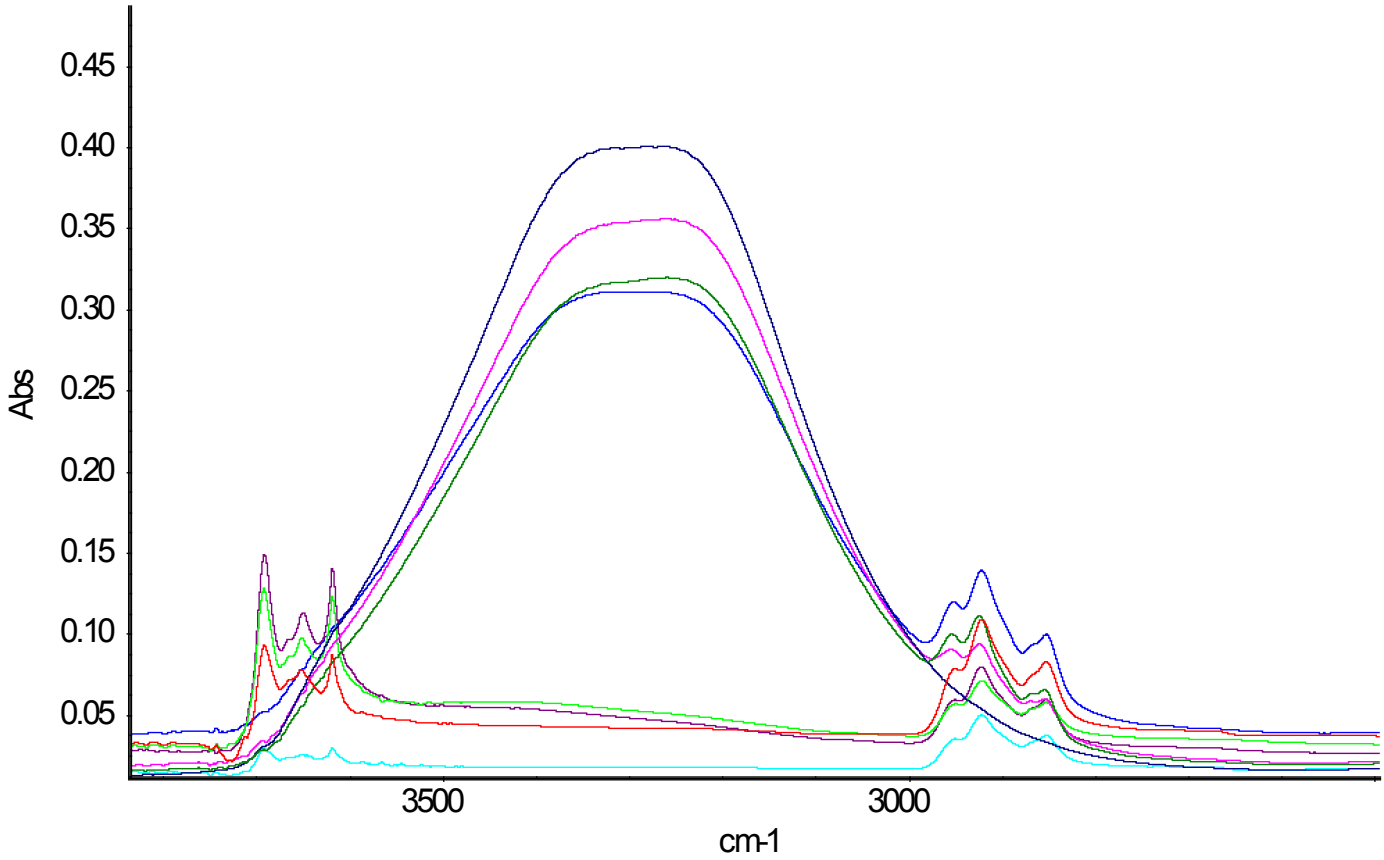

Figure 4.8 Replicated gladiator ATR-FTIR spectra of sample 1730 in the wet and dry state in 4000 to 2500 cm-1 region.

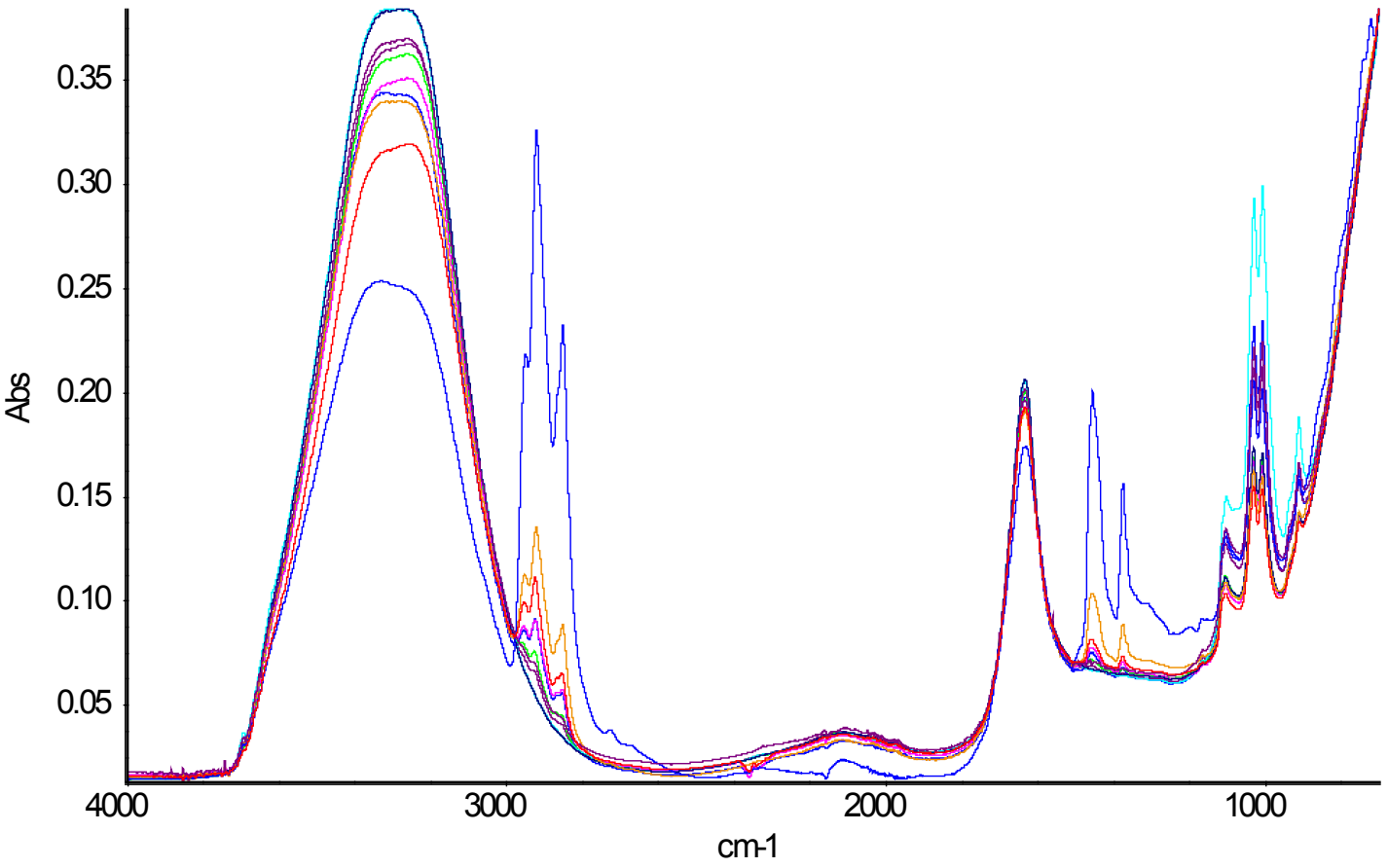

Figure 4.9 Gladiator ATR-FTIR spectra wet spectra of S1725,1727, 1729, 1730, 1731 and 1734 in the 4000 to 700 cm-1 region.

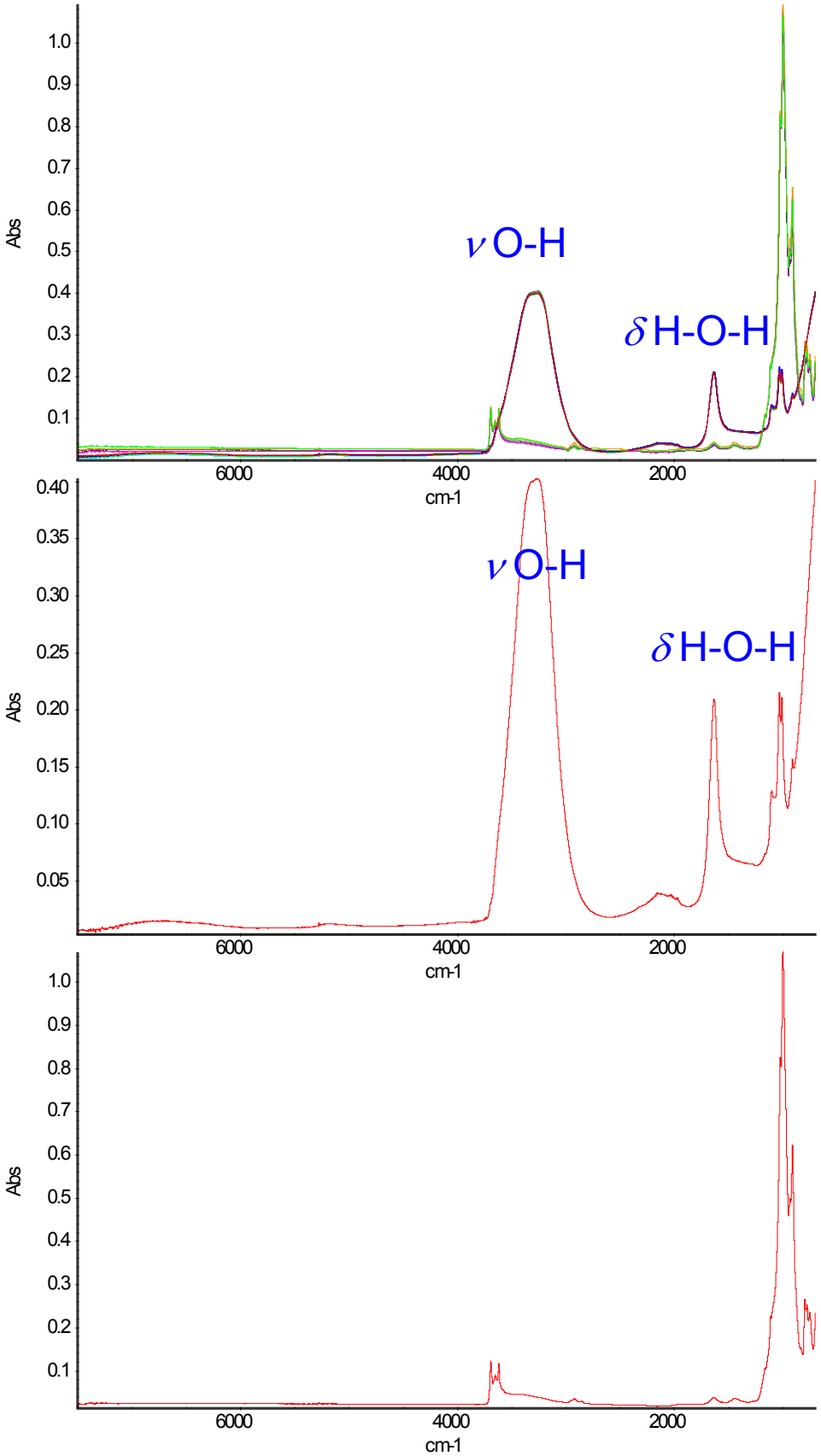

Figure 4.10 Gladiator ATR-FTIR MFT samples 2790 in both wet and dry forms in the 700 to 7500 cm-1 region

Figure 11A

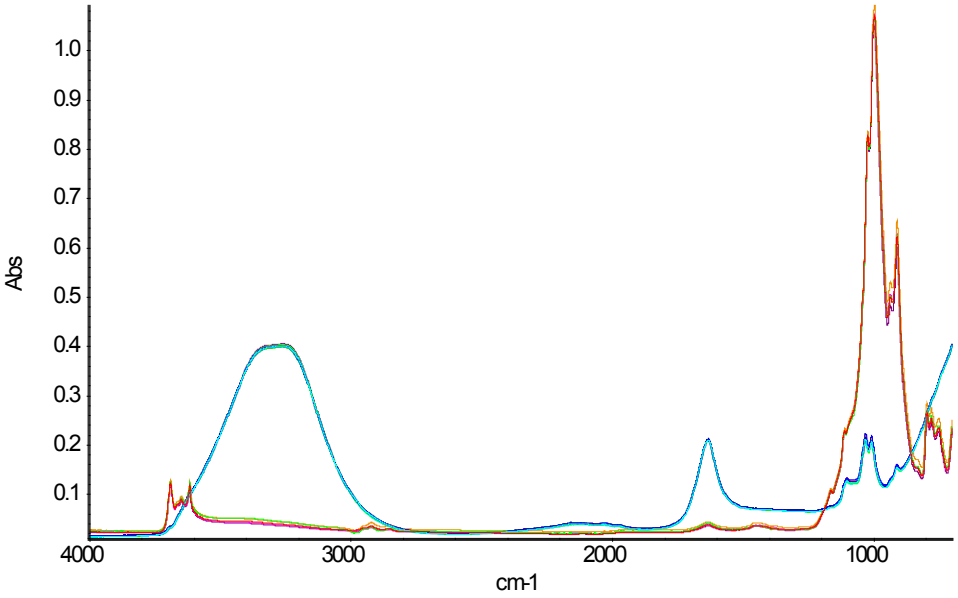

Figure 11B

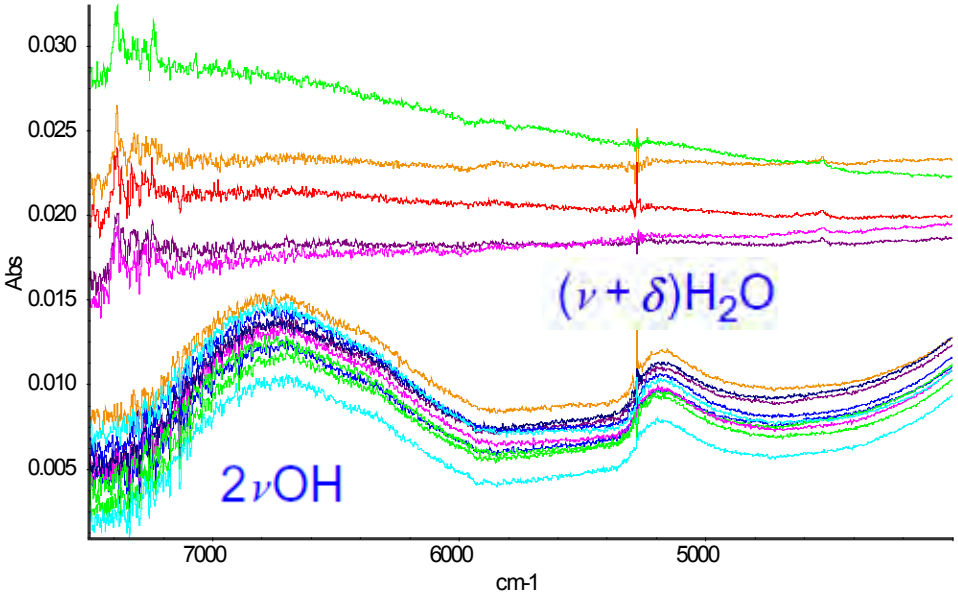

Figure 4.11 Gladiator ATR-FTIR MFT samples 2790 in both wet and dry forms in the 4000 to 700 cm-1 region and in the 7500 to 4000 cm-1 region.

A)

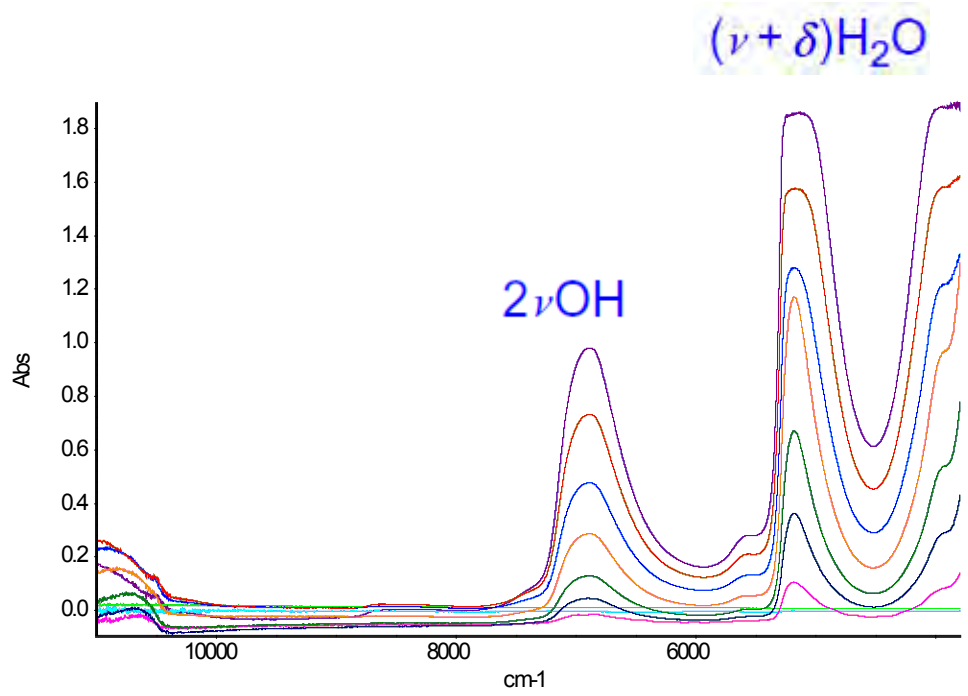

B)

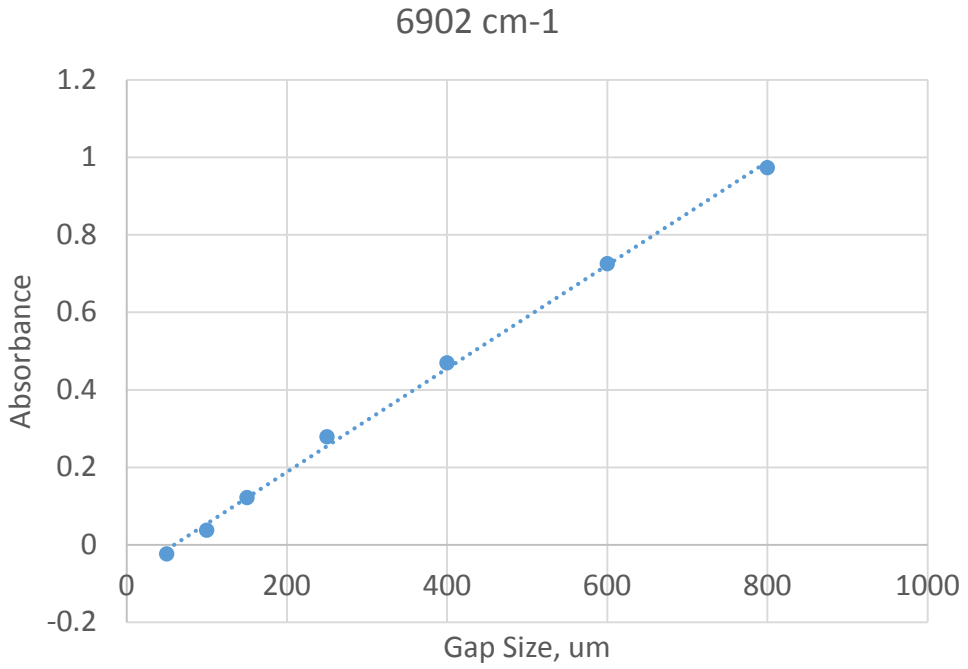

Figure 4.12 Variable path transmission cell spectra of water ranging from 0 to 800 micron pathlength. Spectra were obtained using a CaF2 beamsplitter and InGaAs detector. Beer's law plot of 6902 cm-1 band.

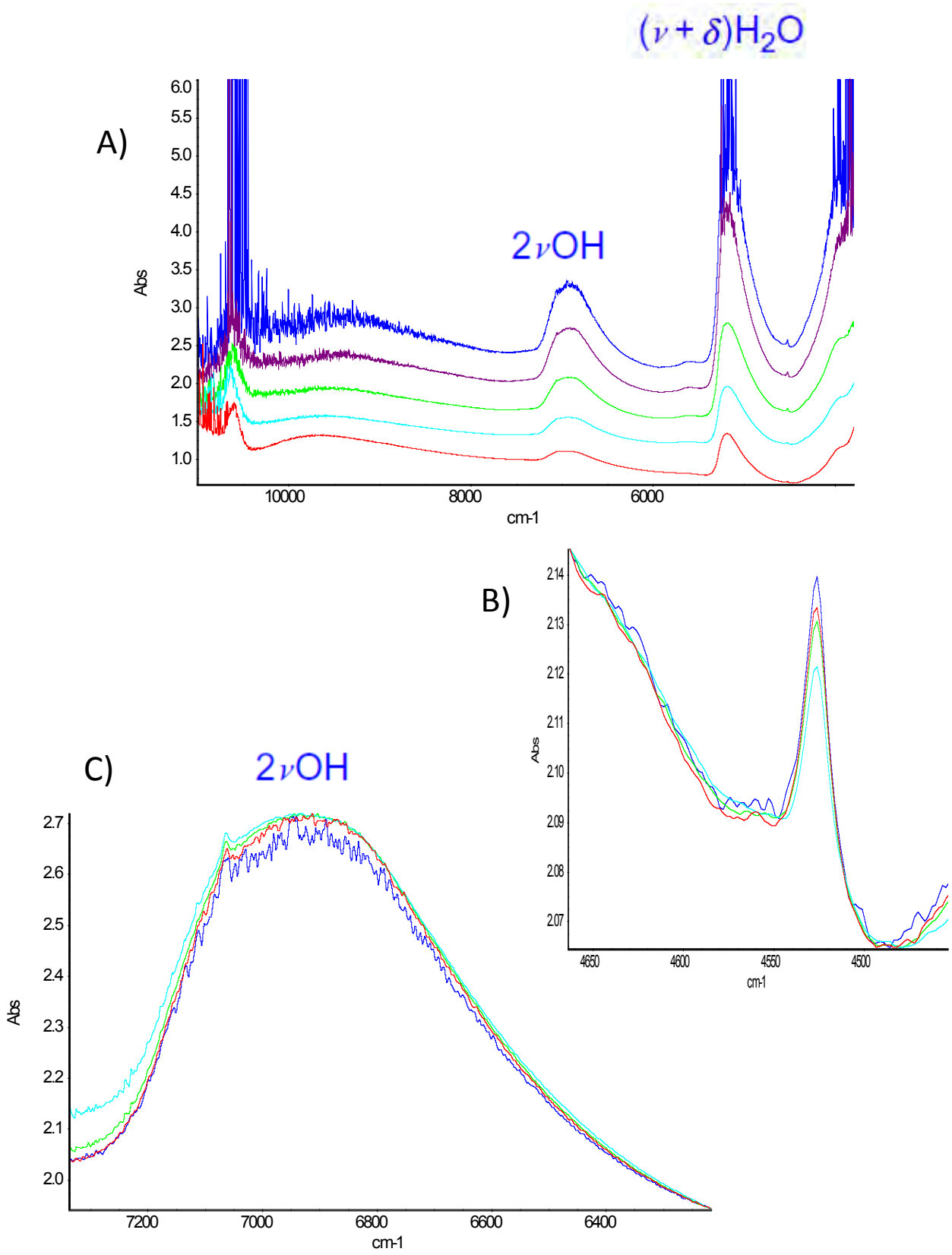

Figure 4.13 Variable path transmission cell spectra of MFT (S1729) ranging from 150 to 600 micron pathlength. Spectra were obtained using a CaF2 beamsplitter and InGaAs detector.

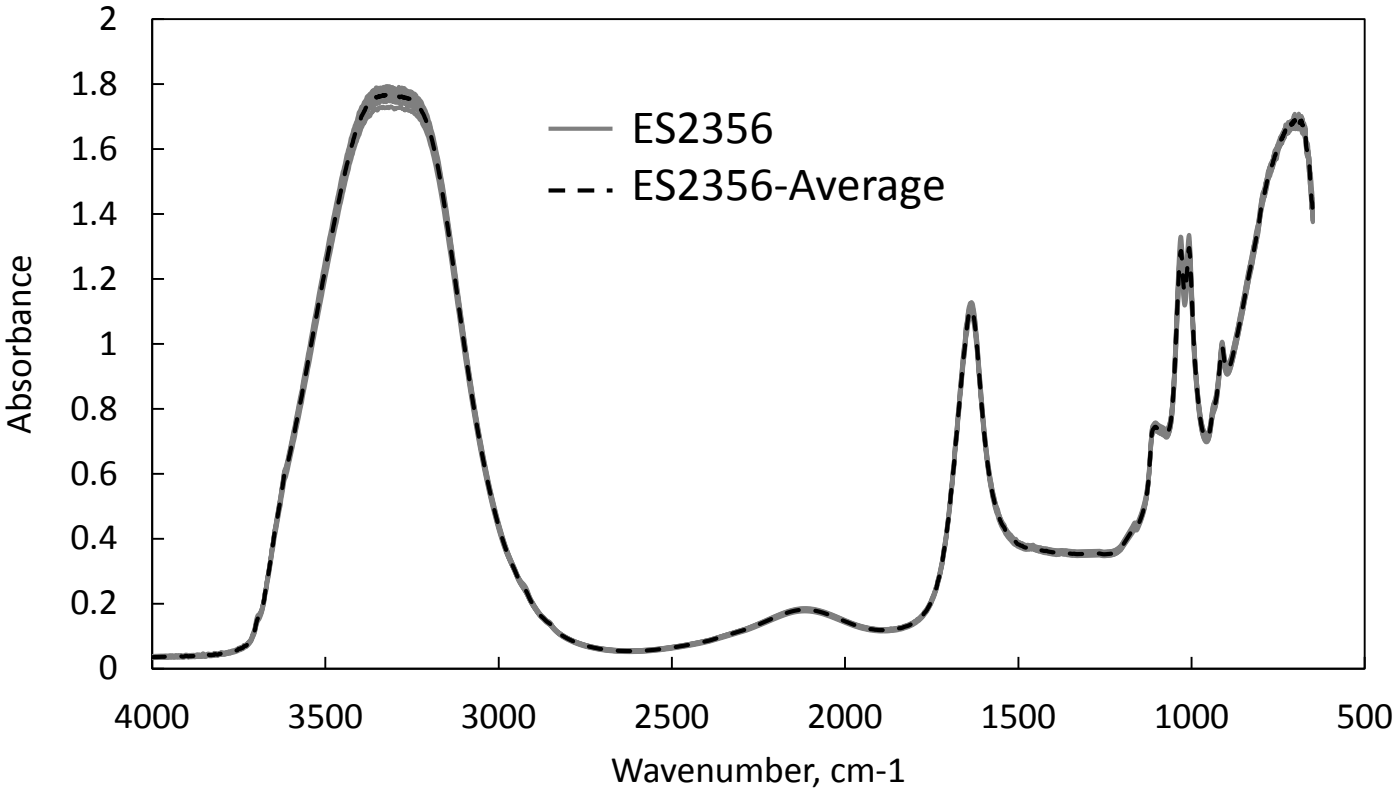

Figure 4.14 Replicated HATR-FTIR spectra of sample ES2356 are shown in the 700 to 4000 cm^{-1} spectral region. A total of 10 spectra are shown on a common scale in gray. The average of the 10 individual spectra is shown by the black bold-dashed line.

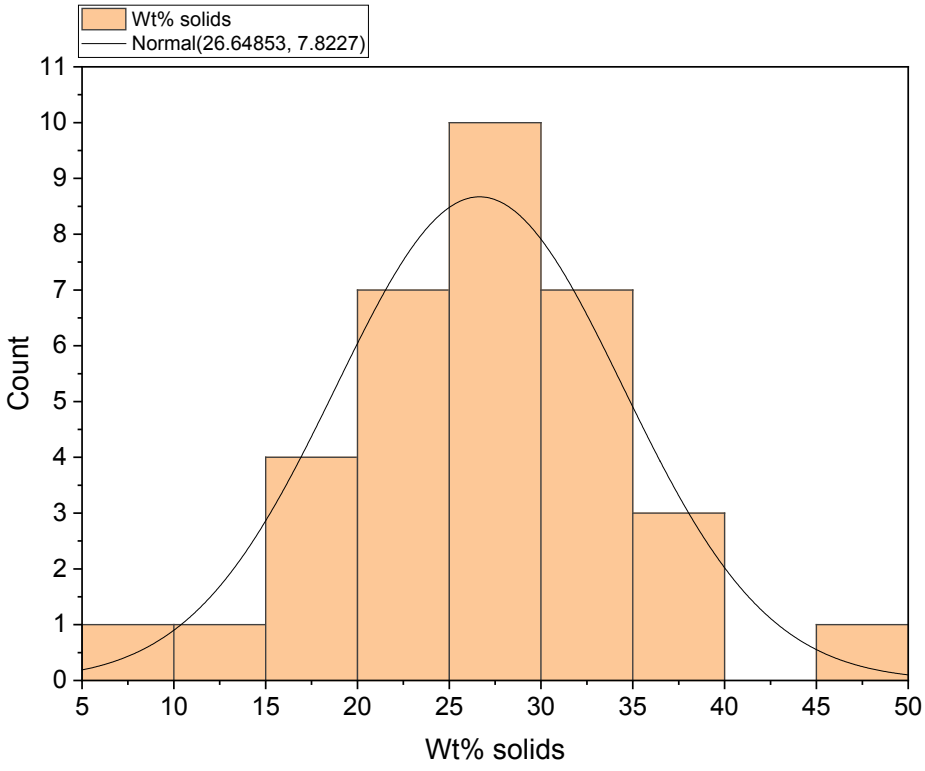

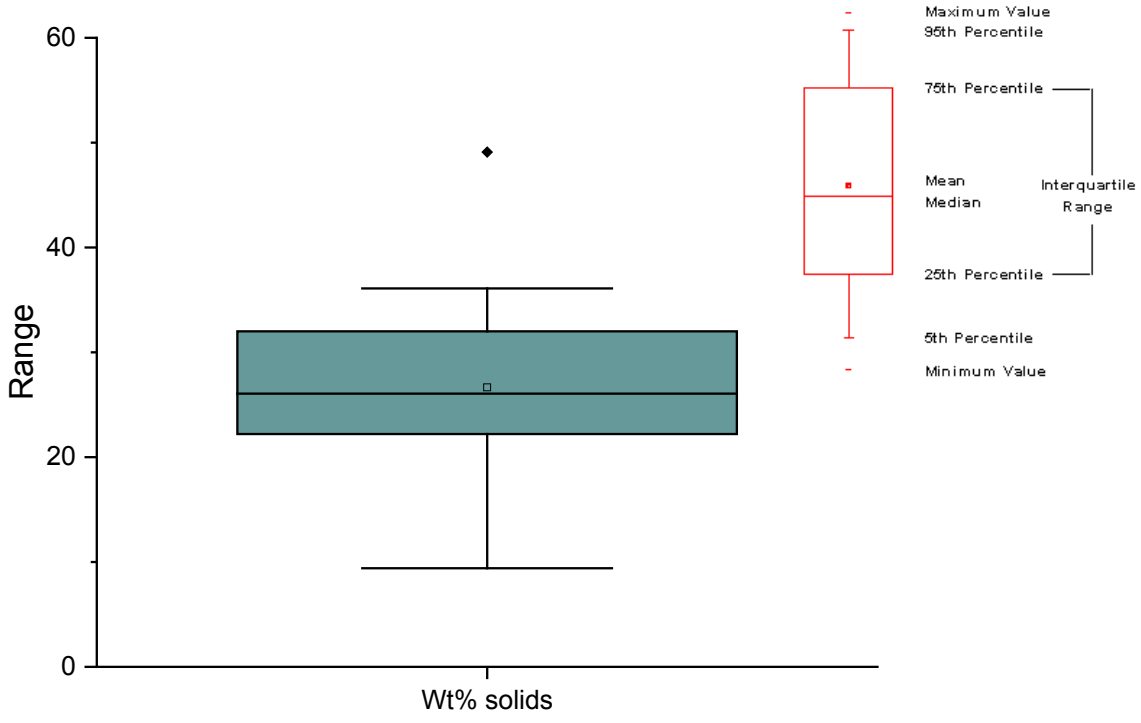

Figure 4.15 Histogram of weight percent solids showing normal distribution mean and full width at half maxima. Also shown is a box plot showing median value, box showing 25th and 75th percentiles, the whiskers represent the 5th and 95th percentiles. The diamonds are outliers.

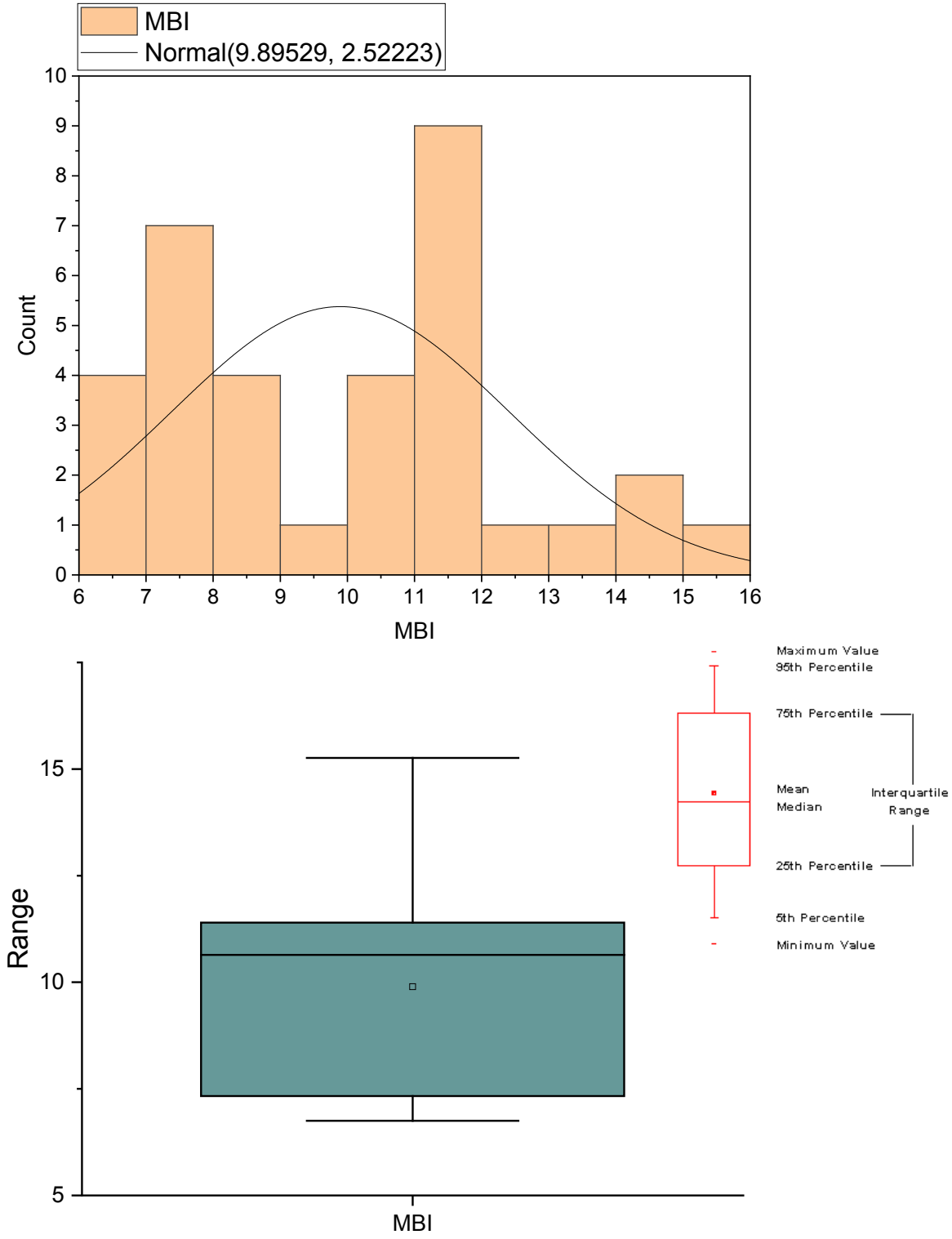

Figure 4.16 Histogram of MBI values showing normal distribution mean and full width at half maxima. Also shown is a box plot showing median value, box showing 25th and 75th percentiles, the whiskers represent the 5th and 95th percentiles.

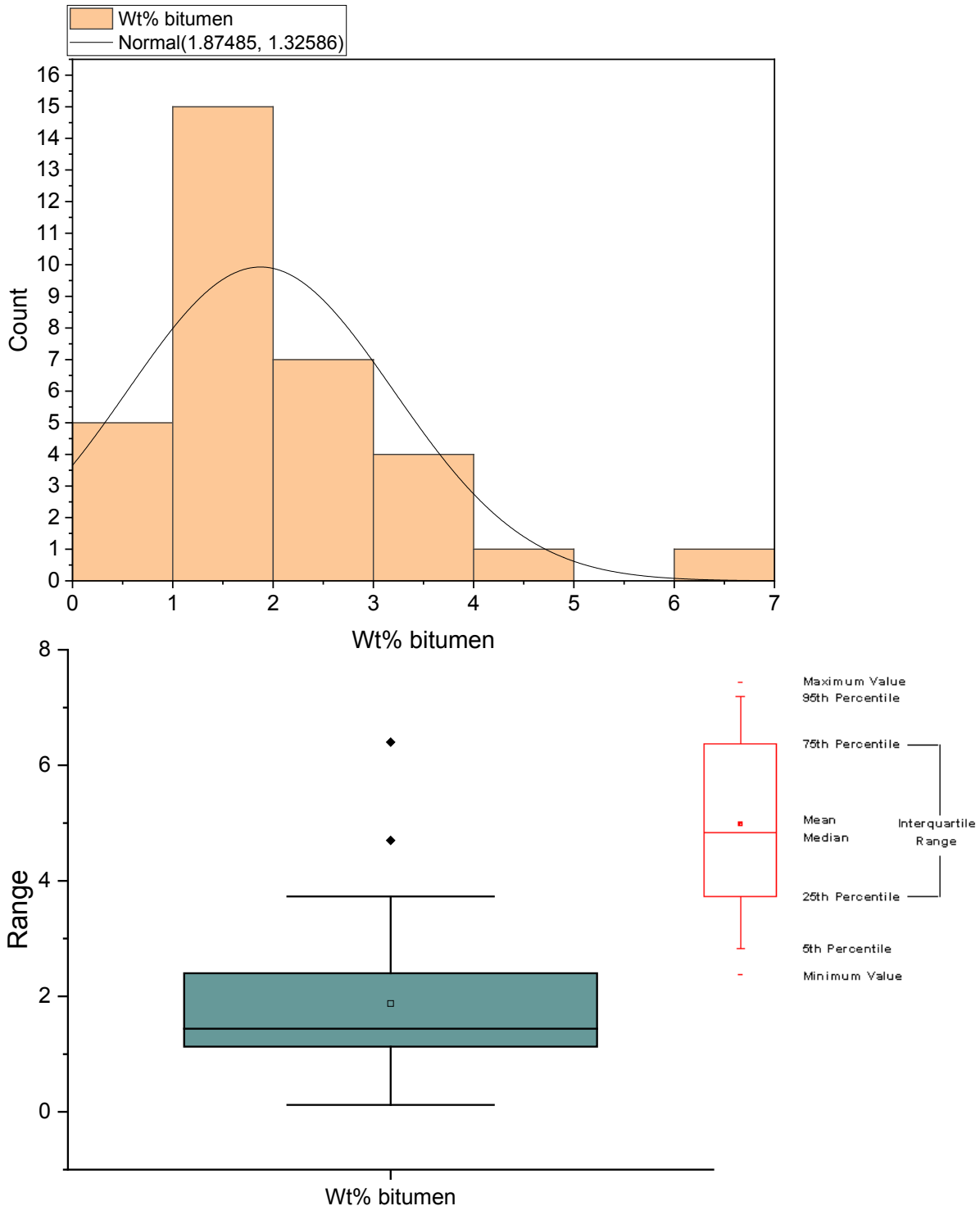

Figure 4.17 Histogram of weight percent bitumen showing normal distribution mean and full width at half maxima. Also shown is a box plot showing median value, box showing 25th and 75th percentiles, the whiskers represent the 5th and 95th percentiles. The diamonds are outliers.

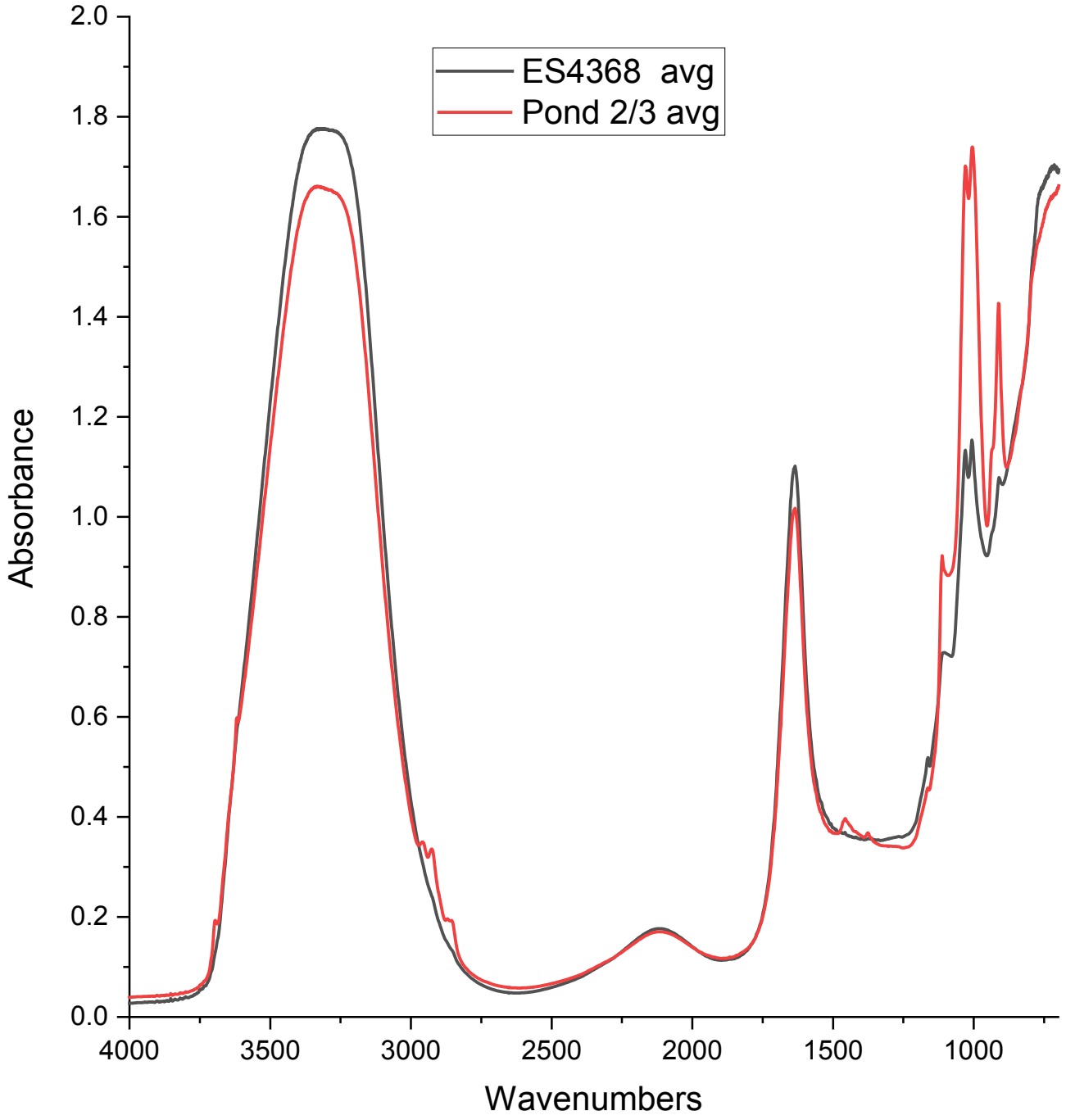

Figure 4.18 Comparison of HATR-FTIR spectra of samples ES4368 (lowest weight percent solids – black) to Pond 2/3/ (highest weight percent solids – red). Each spectrum plotted is the average of 10 replicated spectra.

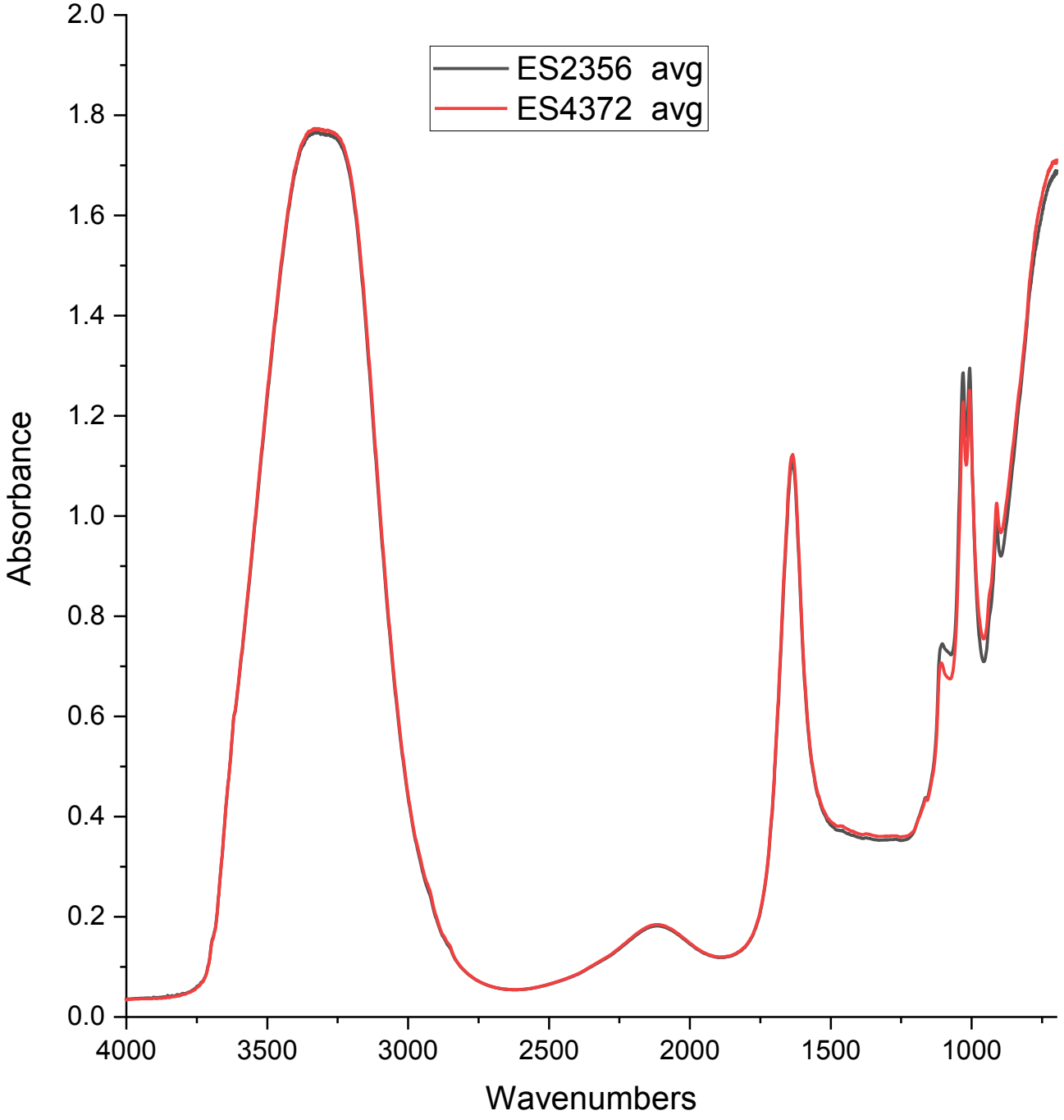

Figure 4.19 Comparison of HATR-FTIR spectra of samples ES2356 (highest MBI- black) to ES4372 (lowest MBI – red). Each spectrum plotted is the average of 10 replicated spectra.

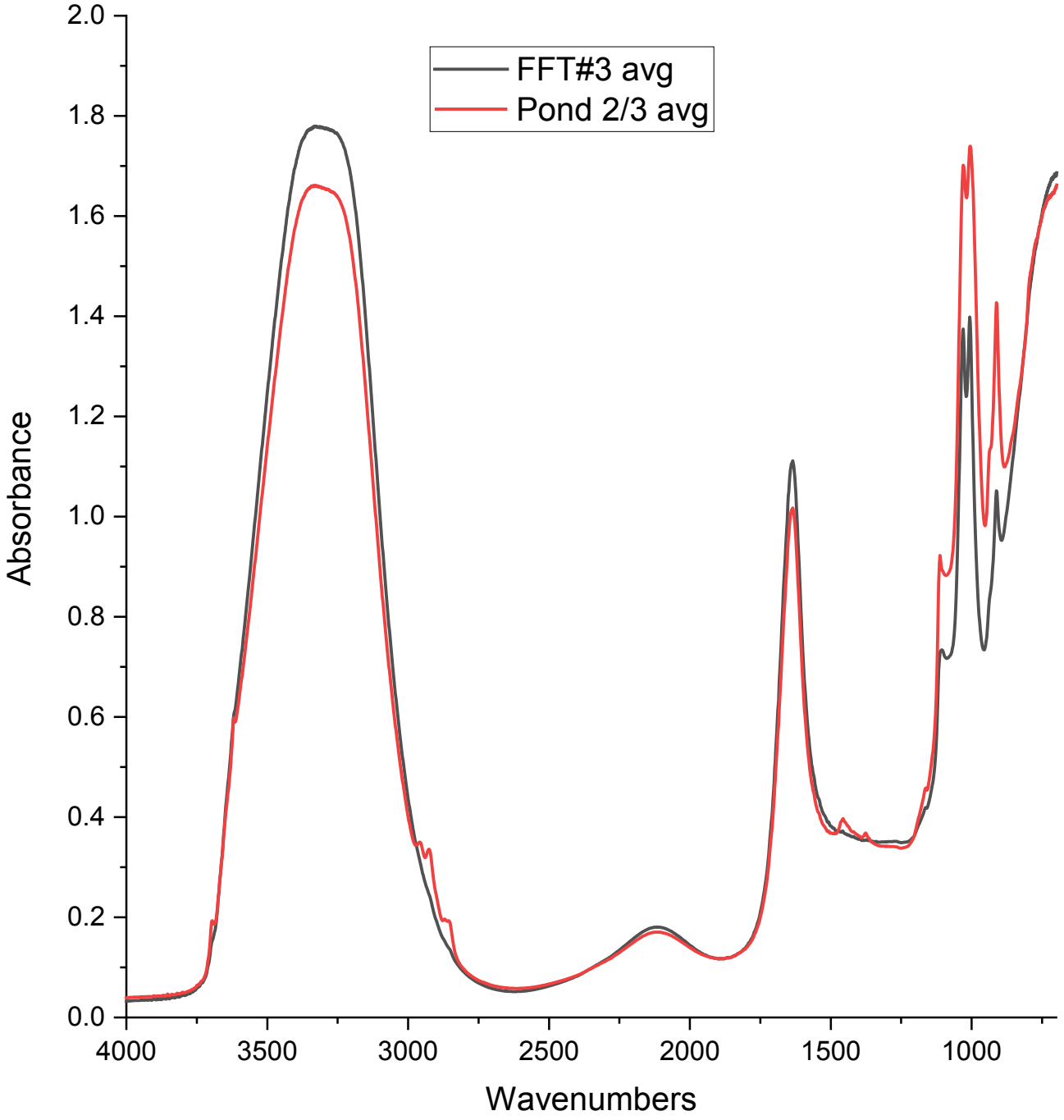

Figure 4.20 Comparison of HATR-FTIR spectra of samples Pond 2/3 (highest weight percent bitumen - red) to FFT3 (lowest weight percent bitumen – black). Each spectrum plotted is the average of 10 replicated spectra.

Figure 4.21 Graphical representation of 34 MFT samples. Each MFT was analyzed a minimum of 10 times, producing a total of 344 samples. The yellow cells were used as calibration files and gold cells were used as validation files in Set 1, corresponding to 244 calibration files and 100 validation files. Set 2 reduced this data set by taking the average of each of the yellow cells for a given MFT as a calibration file, and the average of each of the gold cells as a validation file. This resulted in 34 calibration files and 34 validation files.

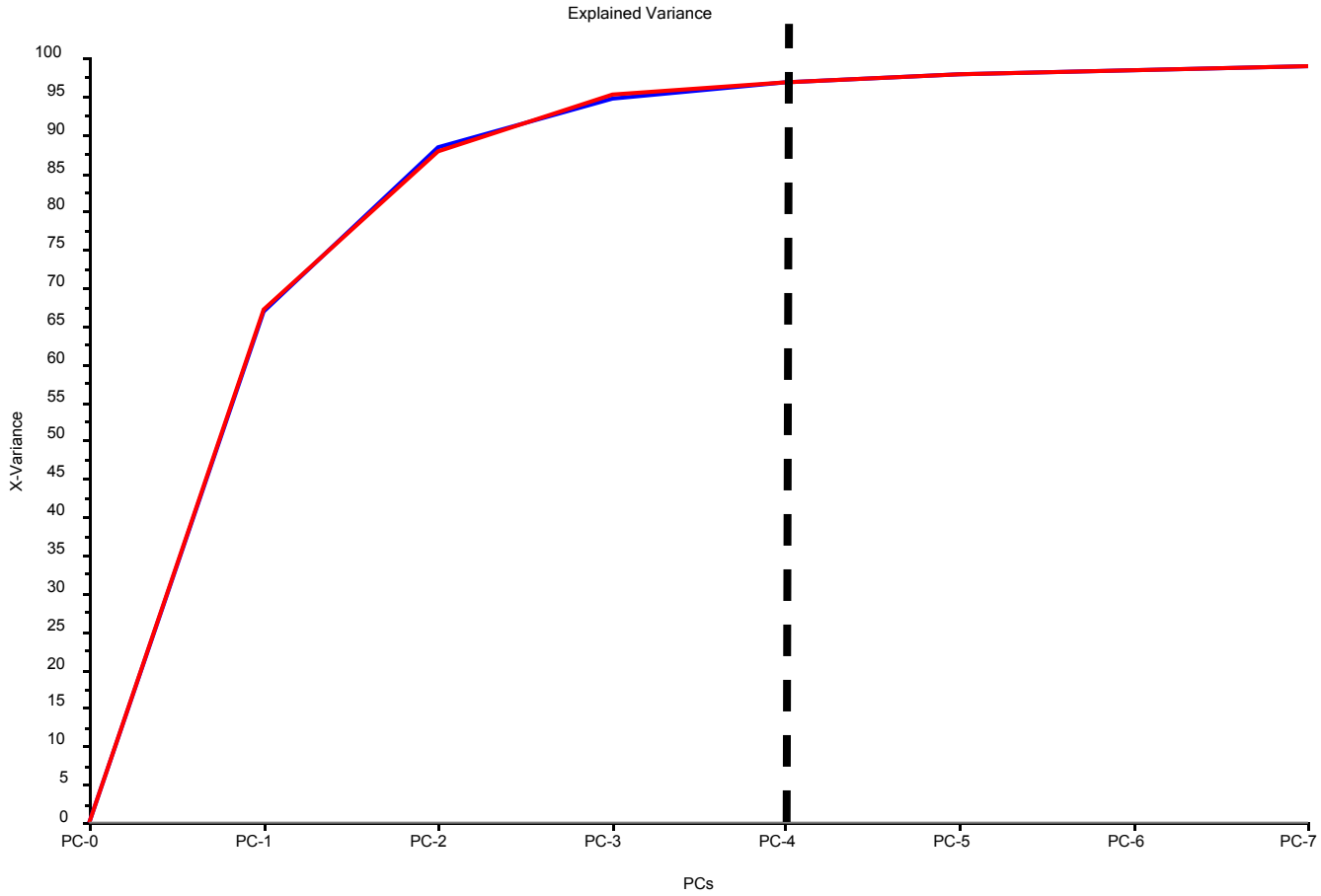

Figure 4.22 Principal component analysis of data **Set 1** (244 calibration and 100 validation files) in the 4000 to 700 cm-1 region. No pretreatment was applied to data. For this model, 4 principal components were recommended and this accounted/explained for 96.9% of the variability for the validation data set (red curve).

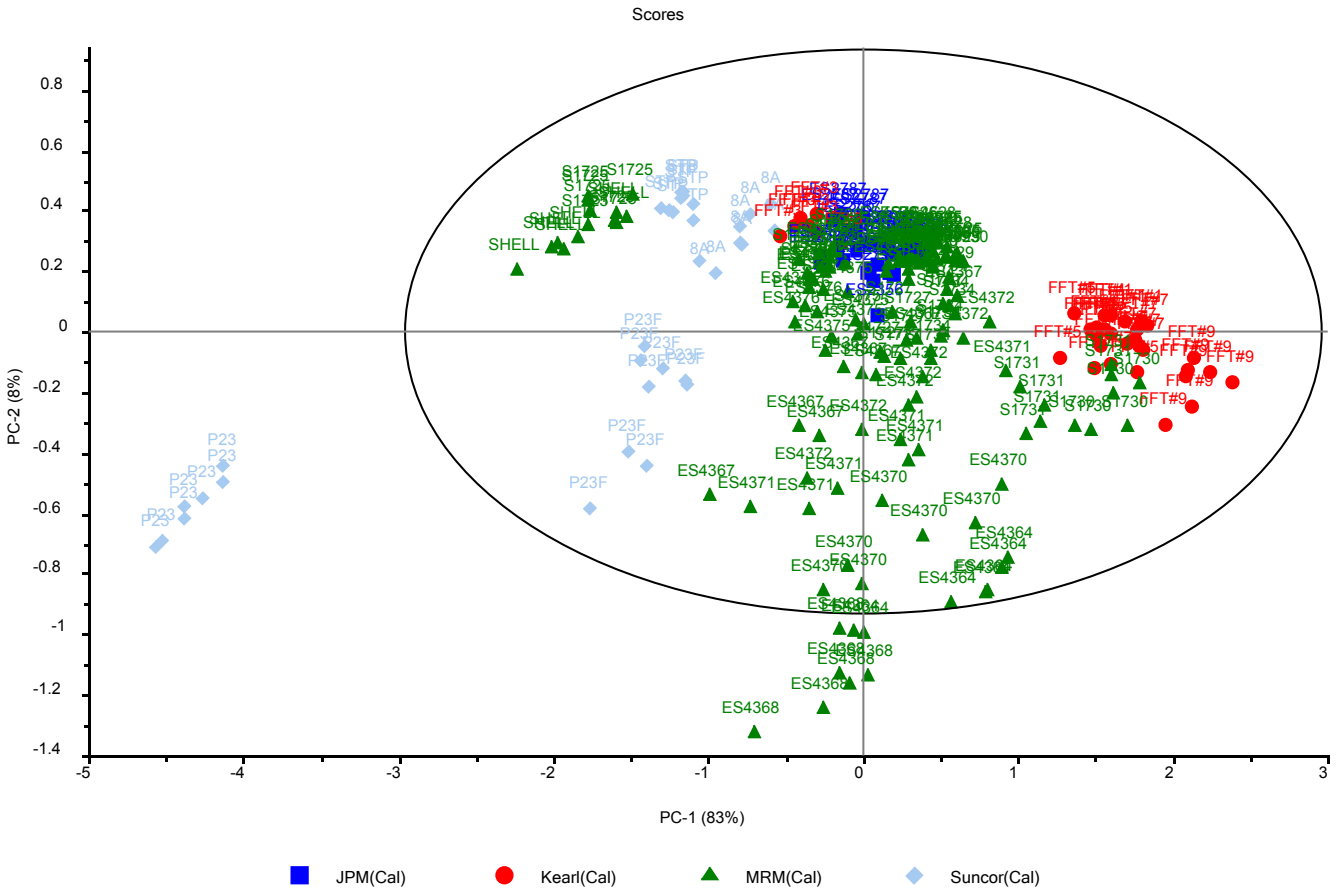

Figure 4.23 PCA plot of MFT data Set 1 in the 4000 to 700 cm-1 region showing principal component 1 (accounting for 83% of the variability) versus principal component 2 (accounting for 8%). The source of the MFTs is indicated and the labels indicate the particular sample.

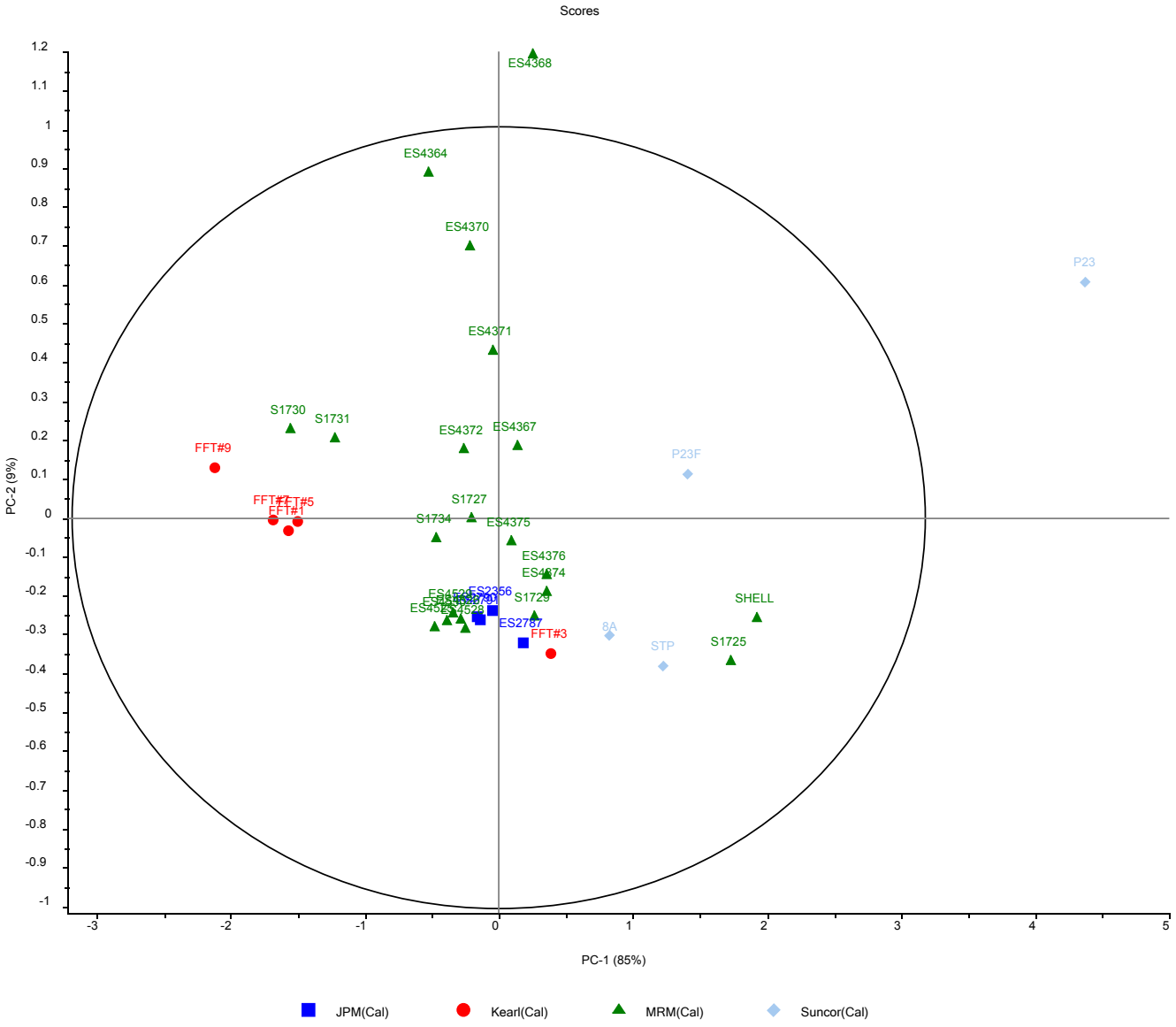

Figure 4.24 PCA plot of reduced MFT data (Set 2) in the 4000 to 700 cm-1 region showing principal component 1 (accounting for 85% of the variability) versus principal component 2 (accounting for 9%). The source of the MFTs is indicated and the labels indicate the particular sample.

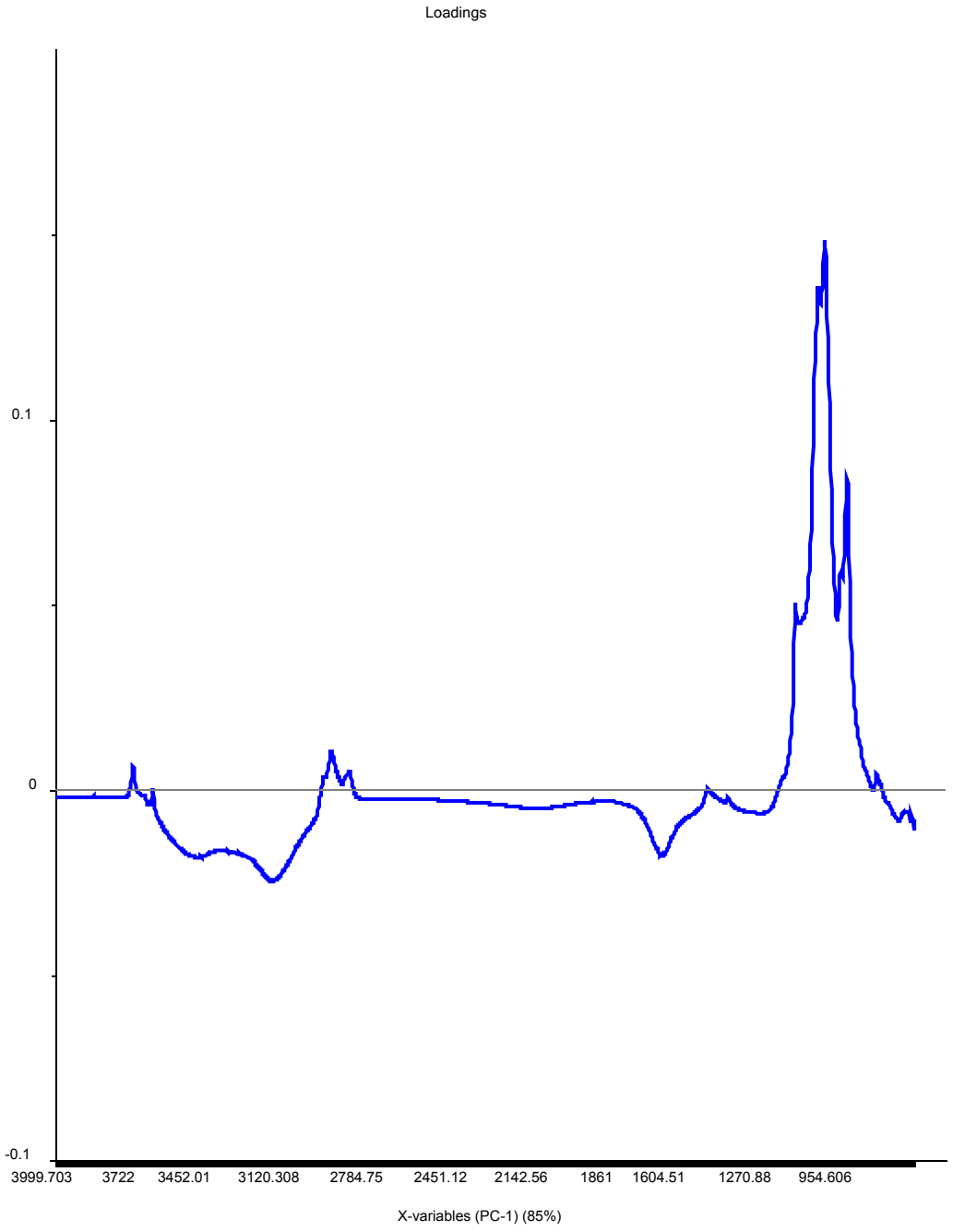

Figure 4.25 Principal component 1 from the PCA analysis of all reduced data set in the 4000 to 700 cm-1 region. This principal component accounts for 85% of variability. The component shows clay bands are positively correlated and water bands are negatively correlated.

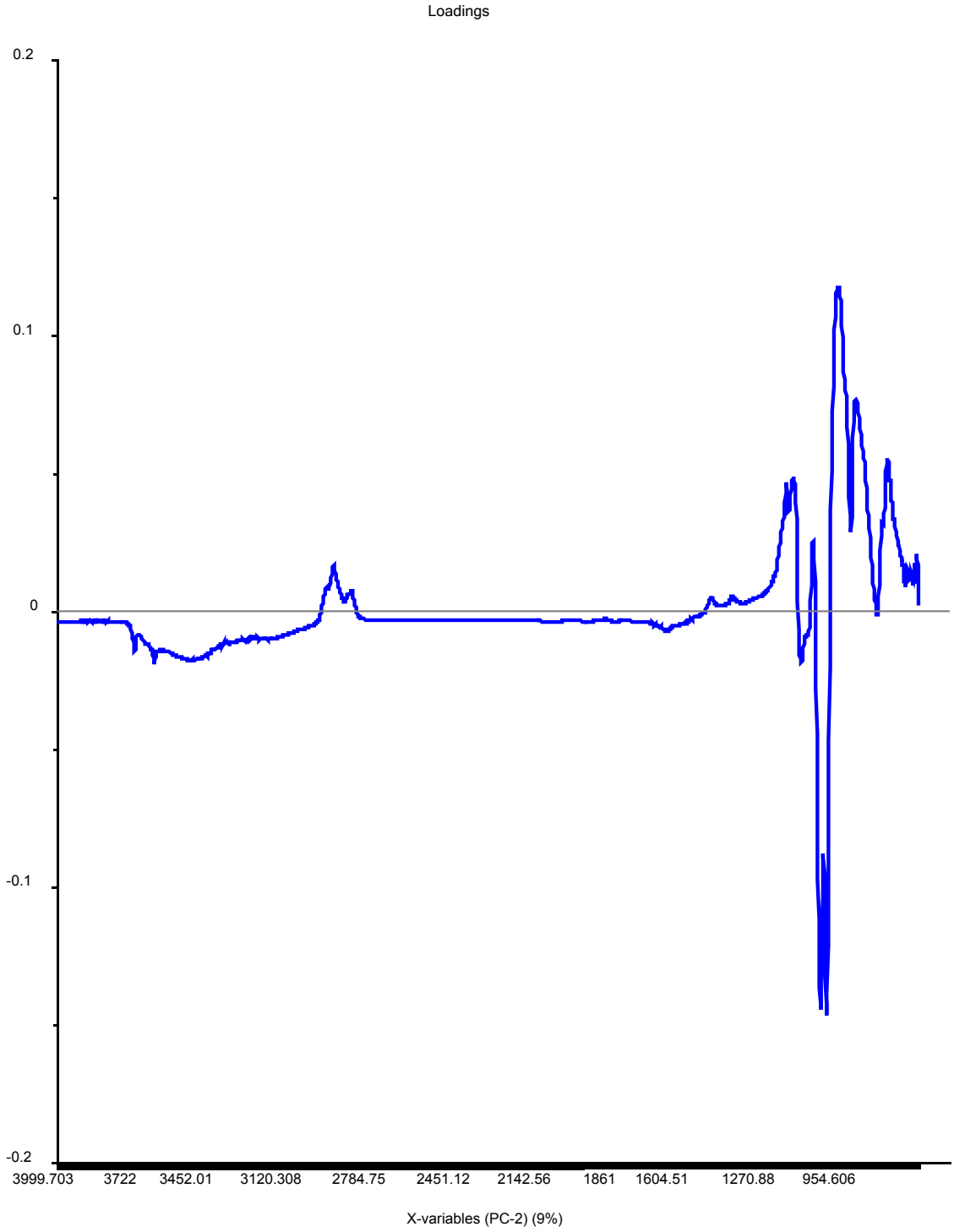

Figure 4.26 Principal component 2 from the PCA analysis of all MFT data (340 spectra) in the 4000 to 700 cm-1 region. This principal component accounts for 21% of variability. The component shows organic bands are positively correlated and water bands are negatively correlated.

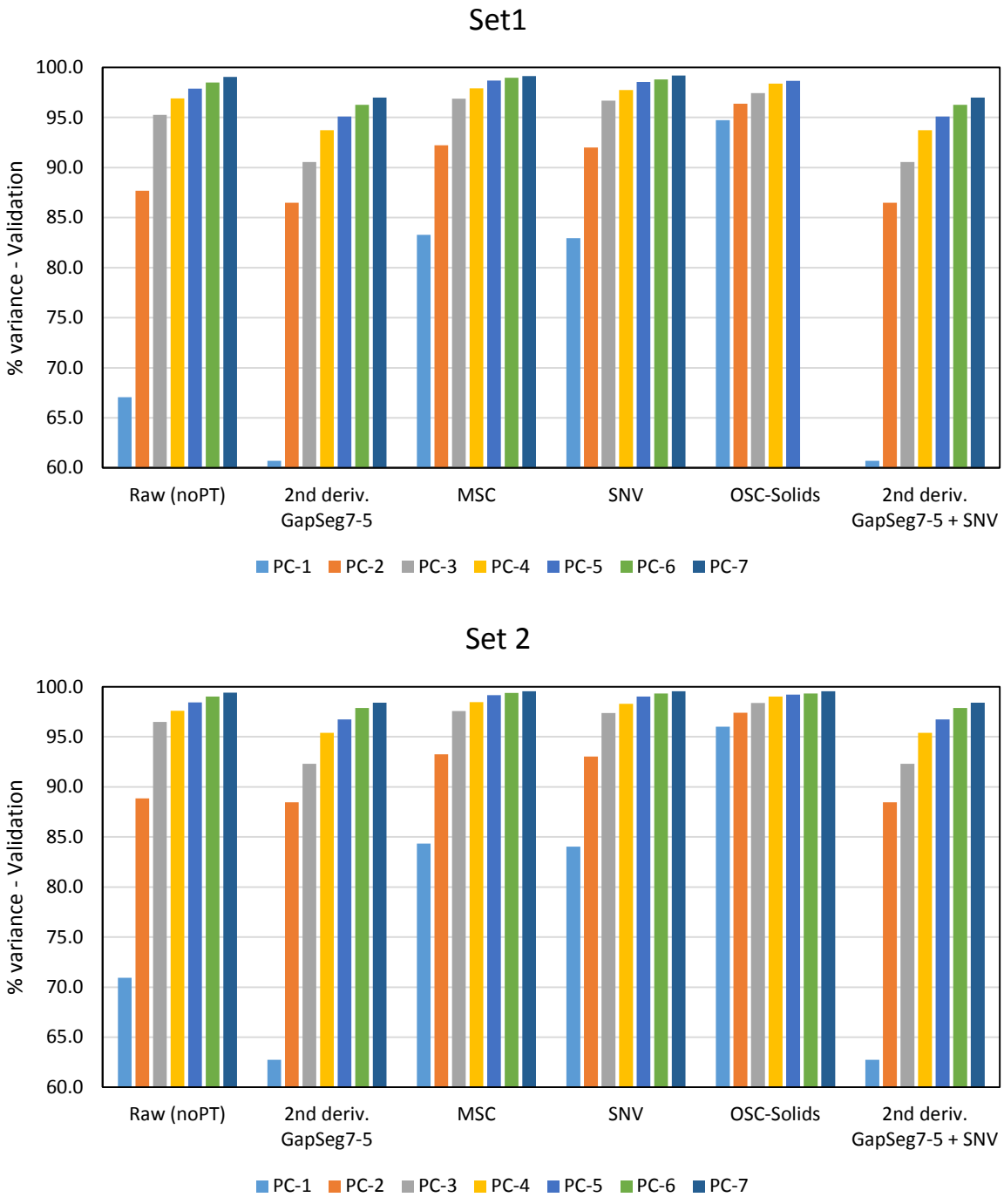

Figure 4.27 Principal Component analysis data sets 1 and 2 files) in the 4000 to 700 cm^{-1} region. This chart is visualizing the data presented in Table 4.4.

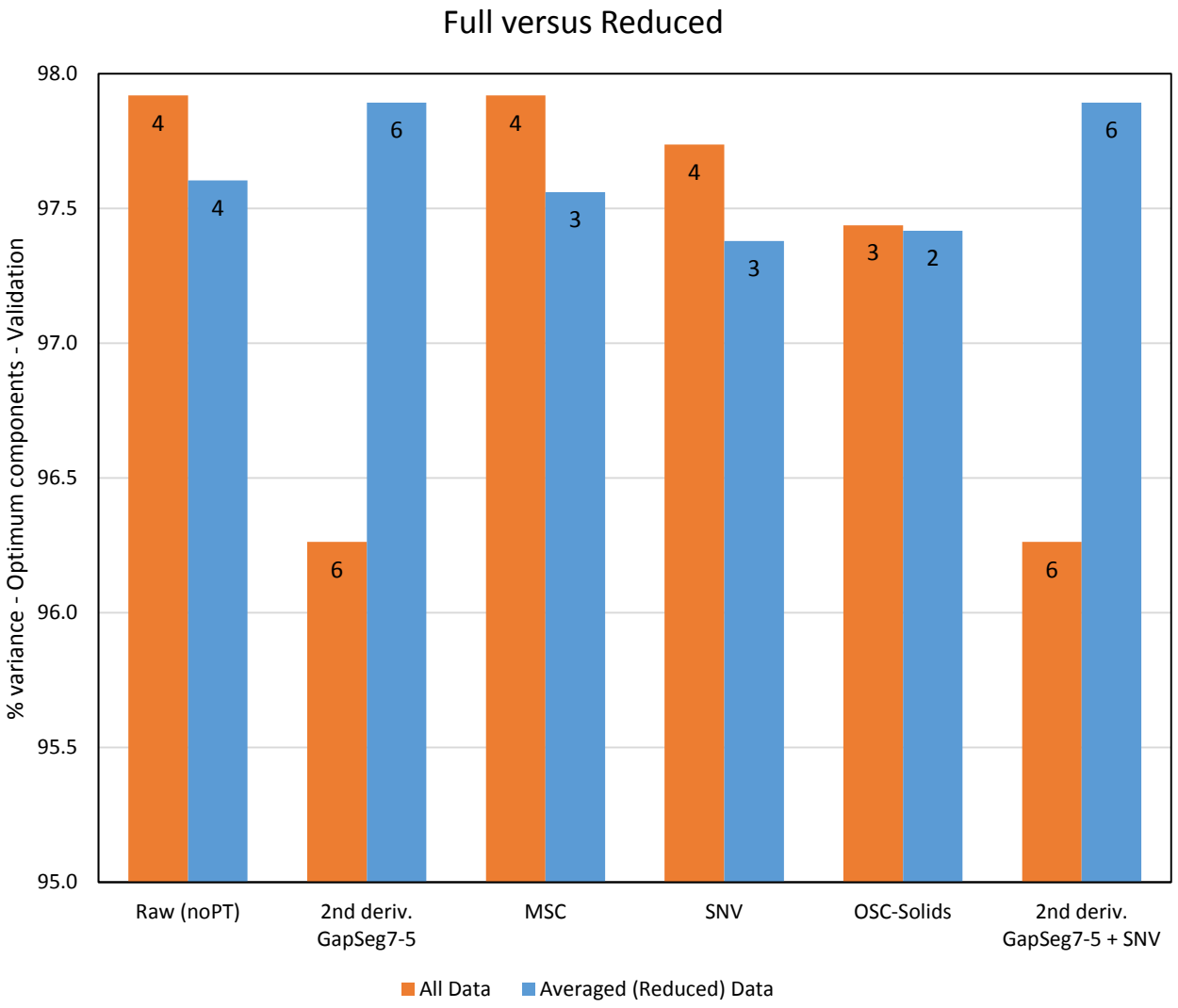

Figure 4.28 Principal Component analysis of the data set 1 (orange) and data set 2 (blue). % variance of the optimum factor is reported. The number in the column shows the optimum # component.

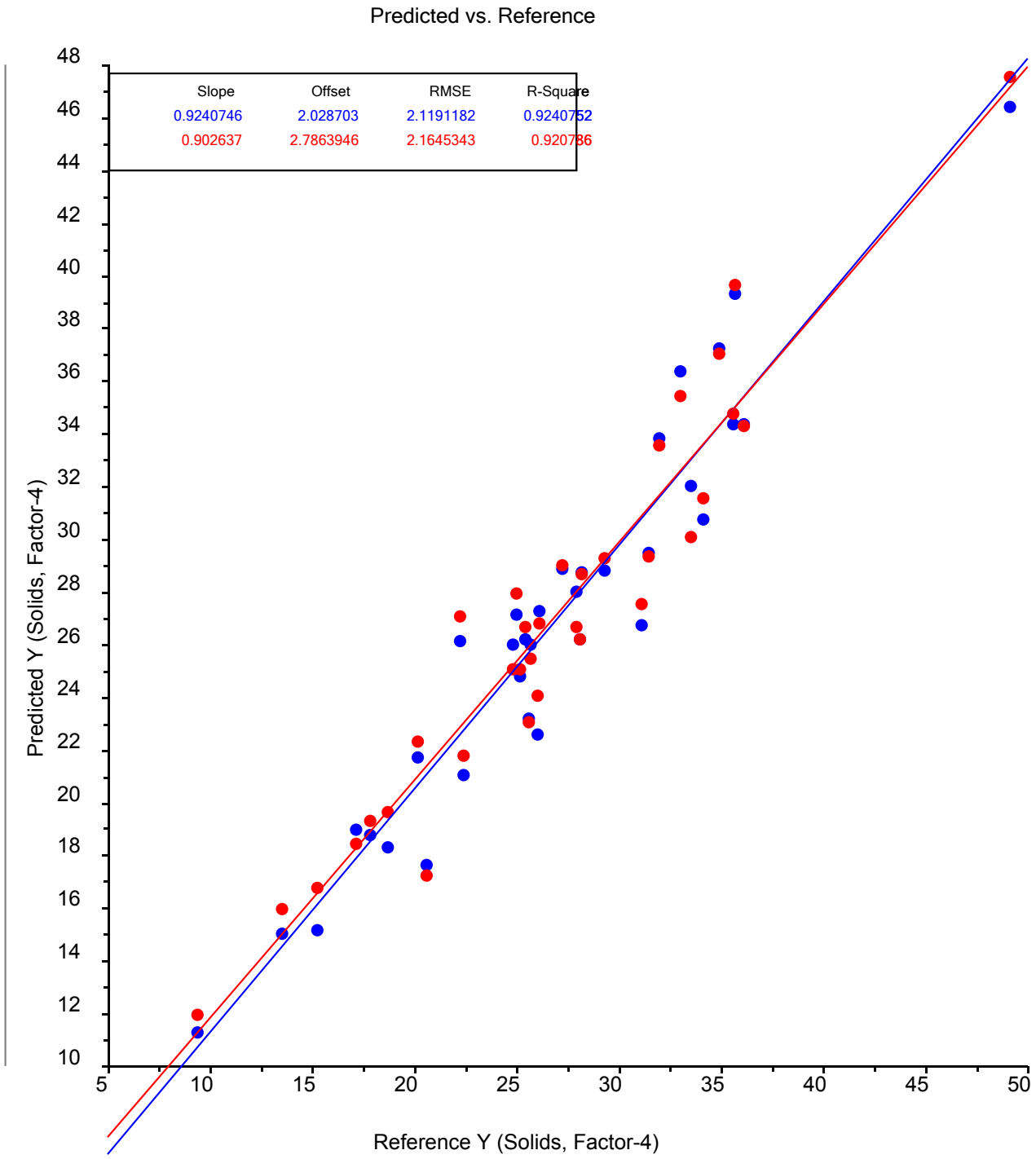

Figure 4.29 Plot of predicted vs reference solids content. No spectral pre-treatment was applied with a number of 4 factors.

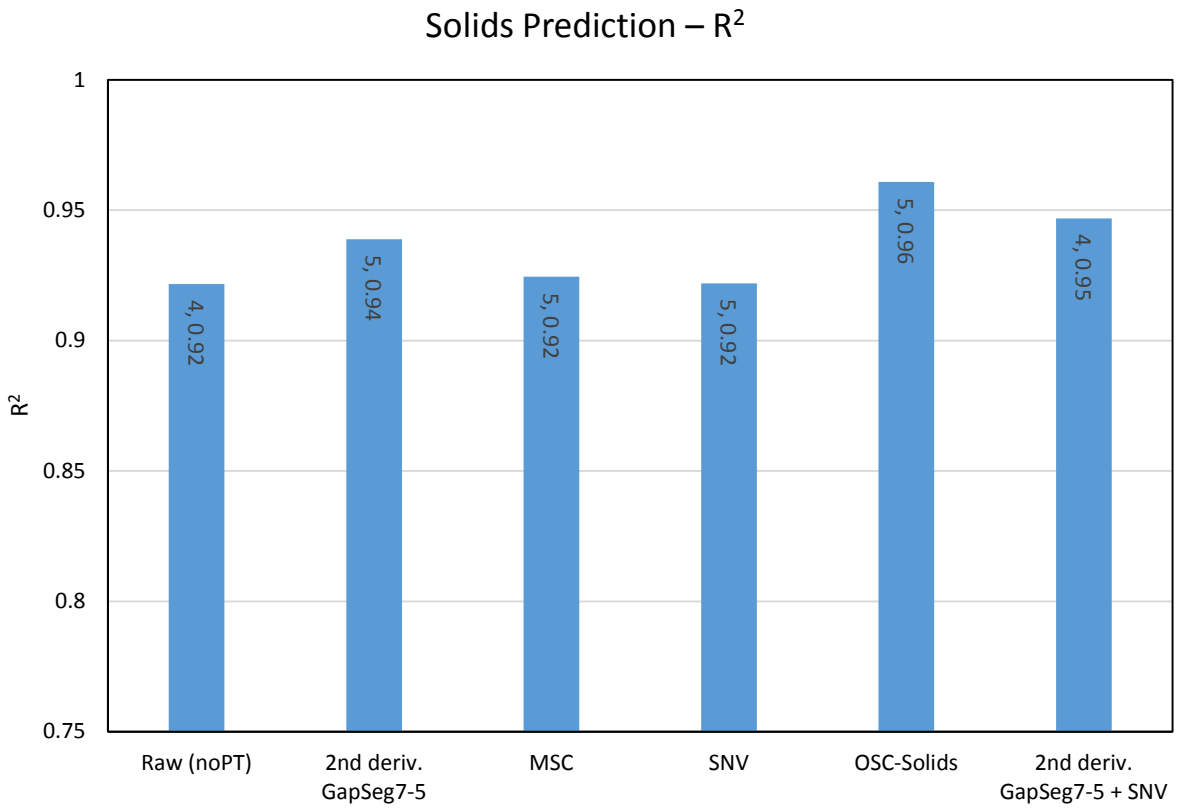

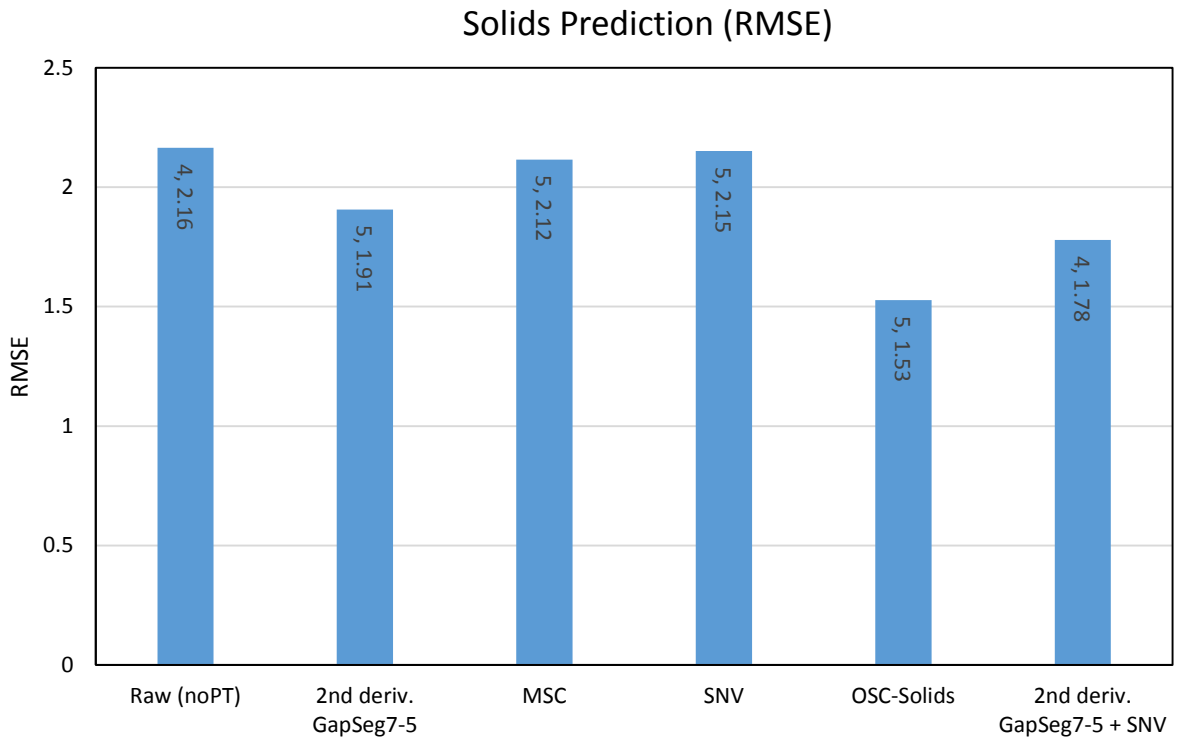

Figure 4.30 Partial least squares analysis of Set 2.

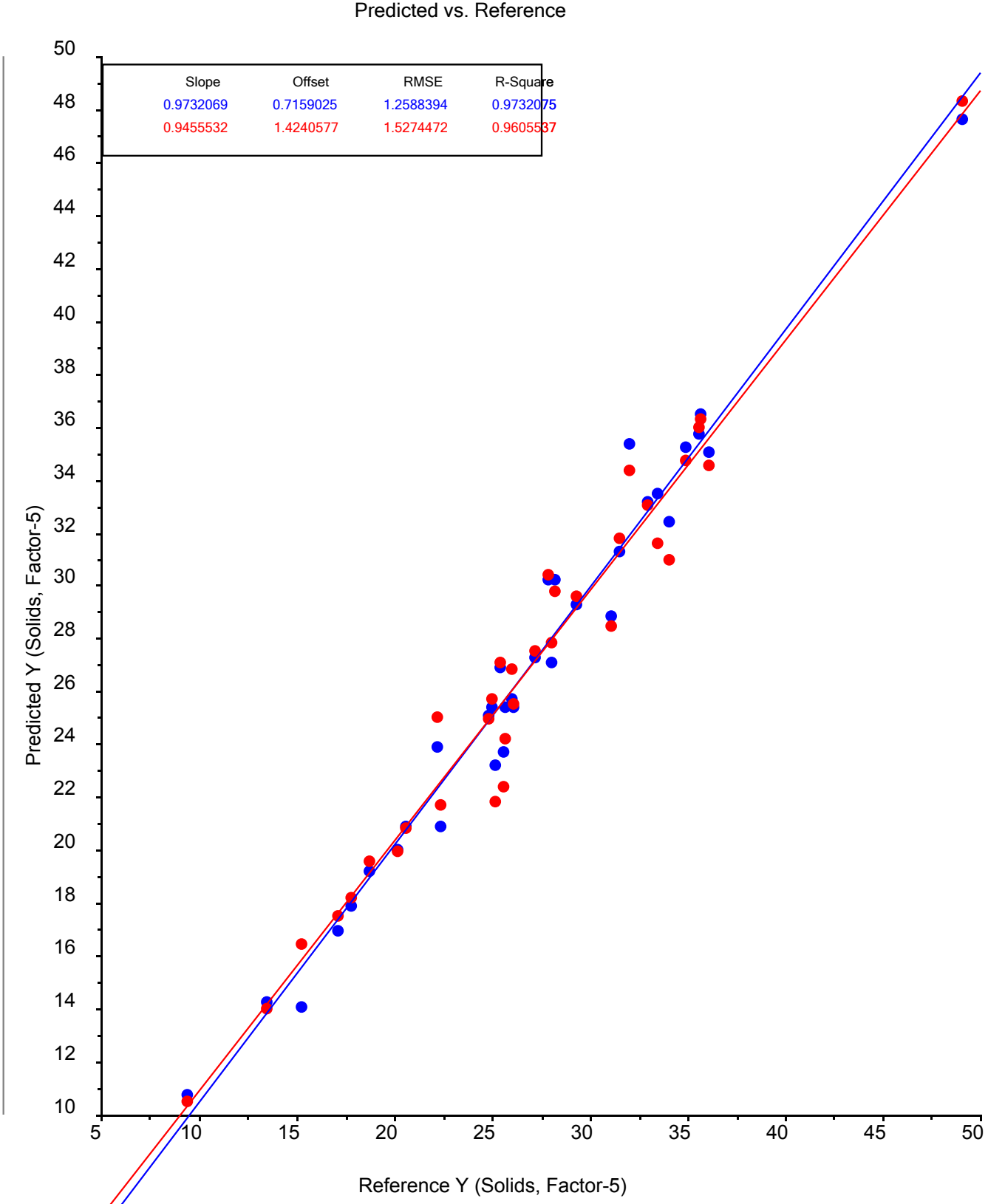

Figure 4.31 Plot of predicted vs reference solids content for the case with OSC spectral pre-treatment (using model recommended 5 factors).

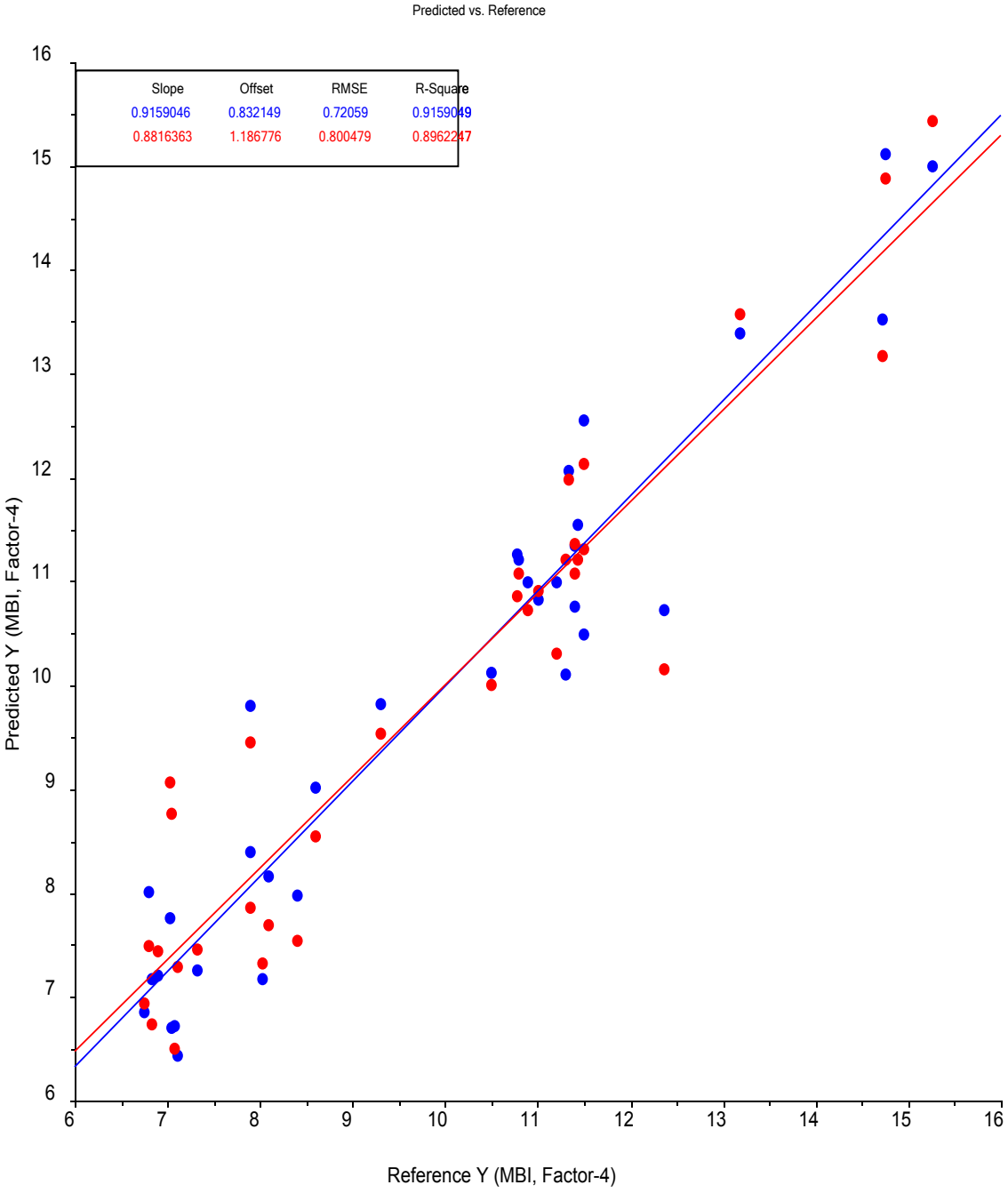

Figure 4.32 Plot of predicted vs reference solids content for prediction of MBI using OSC and 4 factors.

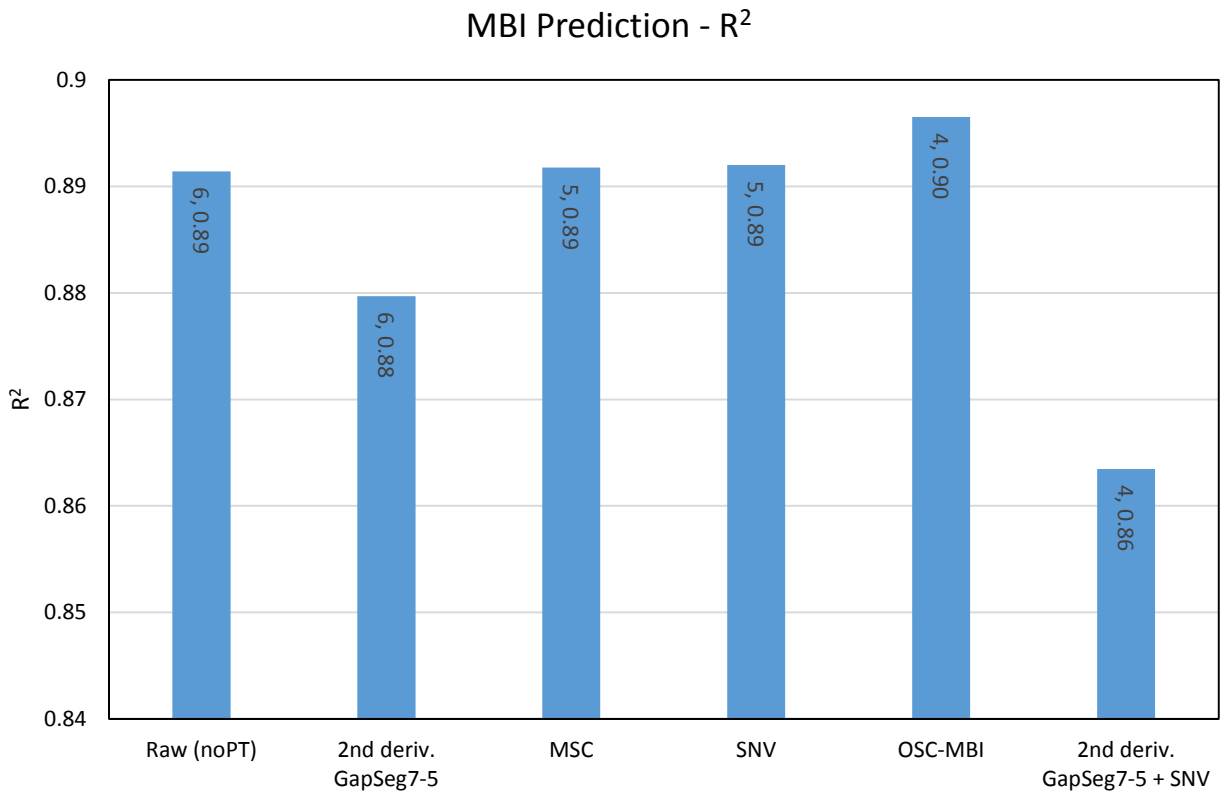

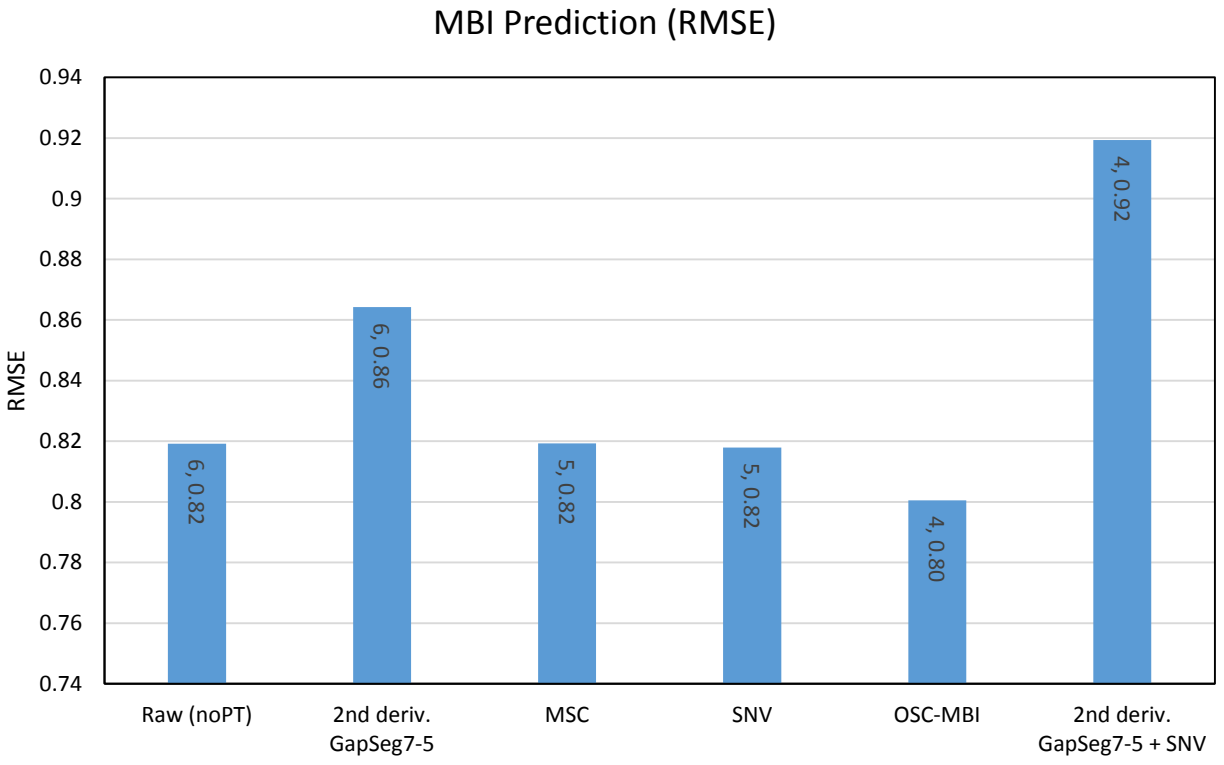

Figure 4.33 Partial least squares analysis of the data Set 2 for prediction of MBI.

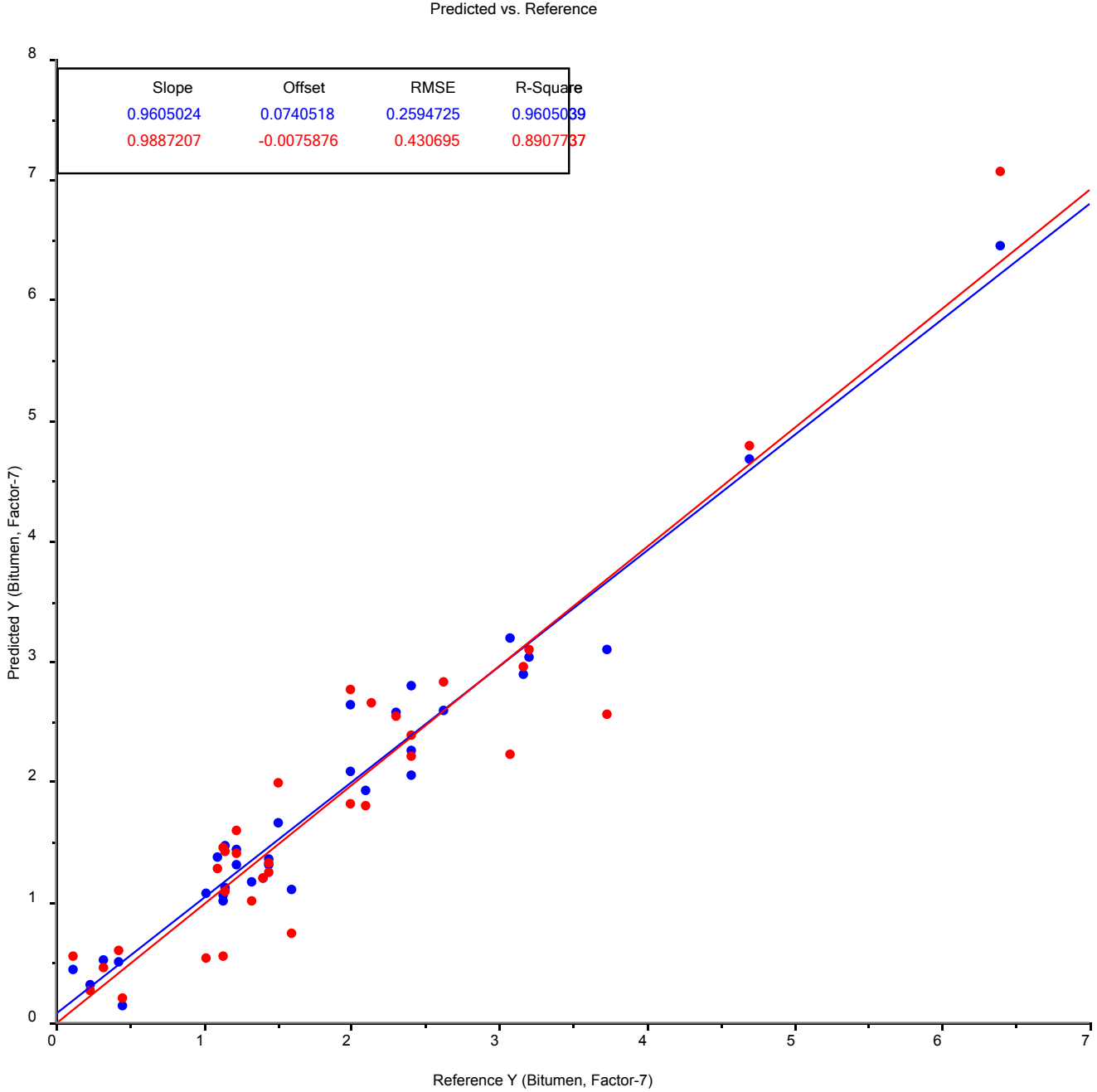

Figure 4.34 Plot of predicted vs reference for bitumen content (OCS using 7 factors).

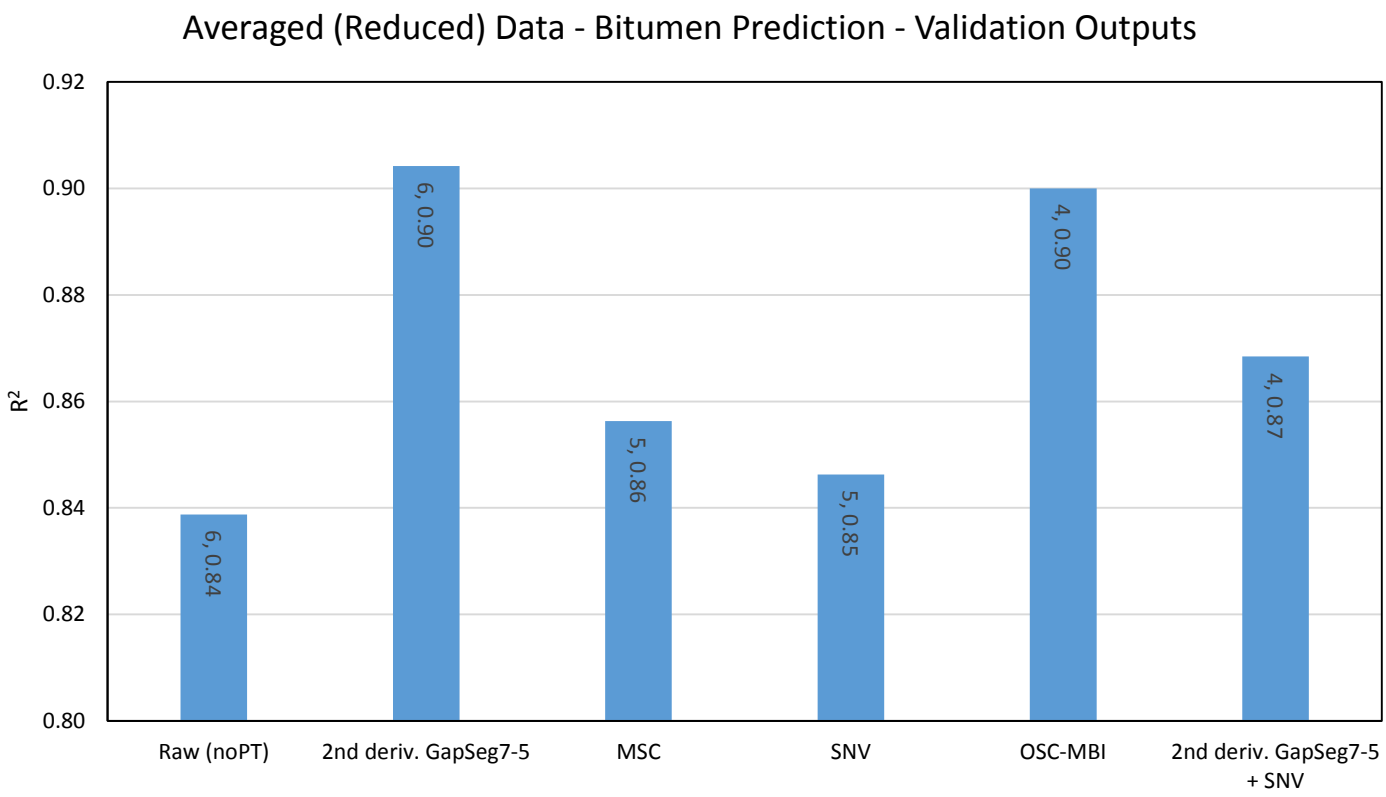

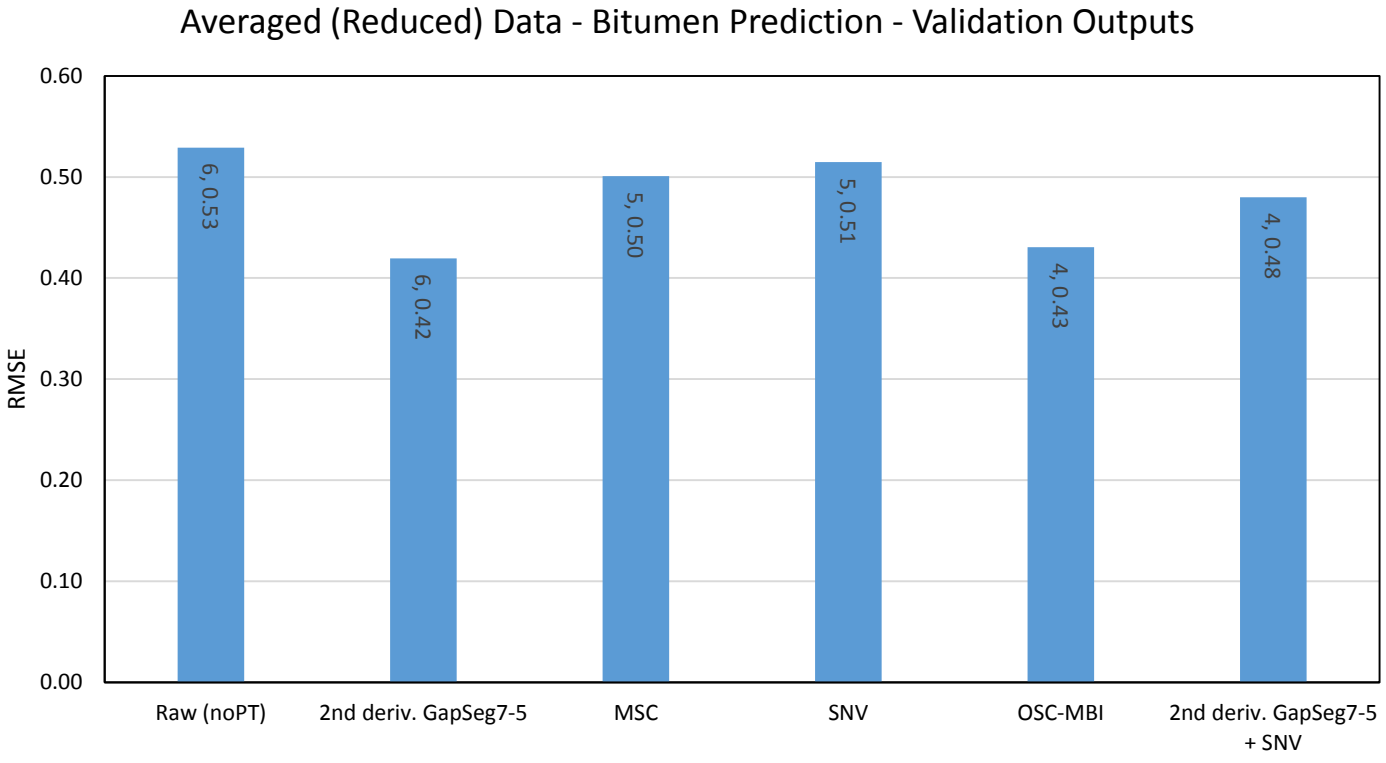

Figure 4.35 PLS results for predicting Bitumen content.

Table 4.1. Mature fine tailing samples investigated and selected properties.

Group	*ID*	*Source*	*Wt% solids*	*Wt % solids -2*	*MBI*	*Wt% bitumen*
1	Pond 2/3	Suncor	49.1	49.1	8.6	6.40
1	Pond 2/3F	Suncor	35.7	35.7	8.4	4.70
1	STP	Suncor	33.5	33.5	11.2	1.10
1	Shell	MRM	34.9	34.9	11.0	1.50
1	Pond 8A	Suncor	32.0	31.6	10.5	
2	S1725	MRM	33.0	33.2	11.5	1.60
2	S1727	MRM	28.2	28.4	6.9	2.40
2	S1729	MRM	31.5	30.4	7.9	2.40
2	S1730	MRM	22.4	21.9	6.8	2.40
2	S1731	MRM	20.6	19.3	9.3	2.10
2	S1734	MRM	27.9	27.8	8.1	2.00
3	ES-4525	MRM	22.2	24.6	12.4	1.22
3	ES-4526	MRM	24.8	25.0	11.4	1.22
3	ES-4528	MRM	25.0	25.5	11.3	1.40
3	ES-4529	MRM	26.1	25.5	10.9	1.13
3	ES-4530	MRM	25.2	25.1	10.8	1.32
3	ES-4364	MRM	13.5	16.8	7.9	1.44
3	ES-4367	MRM	31.1	31.1	7.3	3.73
3	ES-4368	MRM	9.4	13.2	7.1	1.02
3	ES-4370	MRM	20.2	21.2	7.1	1.99
3	ES-4371	MRM	25.7	25.9	7.1	2.30
3	ES-4372	MRM	29.3	29.6	6.8	2.62
3	ES-4374	MRM	35.6	36.4	8.0	3.21
3	ES-4375	MRM	34.1	34.0	7.0	3.08
3	ES-4376	MRM	36.1	36.0	6.8	3.17
3	ES-2356	JPM	26.0	25.3	15.3	1.15
3	ES-2787	JPM	28.1	27.8	13.2	1.44
3	ES-2790	JPM	24.4	25.2	14.8	1.13
3	ES-2791	JPM	24.2	25.5	14.7	1.15
4	FFT1_2/27/19	Kearl	17.8	17.8	11.4	0.23
4	FFT3_3/1/19	Kearl	27.2	26.8	11.5	0.12
4	FFT5_3/3/19	Kearl	18.7	18.2	10.8	0.43
4	FFT7_3/5/19	Kearl	17.2	16.9	11.4	0.45
4	FFT9_3/7/19	Kearl	15.3	15.3	11.3	0.32

Table 4.2 Summary of MFT properties

	# of amples	Mean	Std. Dev.	Min.	Max.
Wt% solids	34	26.6	7.8	9.4	49.1
MBI	34	9.9	2.5	6.8	15.3
Wt% bitumen	33	1.9	1.3	0.1	6.4

Table 4.3 MFT properties grouped according to source.

	# of samples	Wt. % solids	Std. Dev.		MBI	Std. Dev.		Wt % bitumen	Std. Dev.
Suncor	4	37.6	7.8		9.7	1.4		4.07	2.71
MRM	21	26.5	7.0		8.7	2.0		2.06	0.79
JPM	4	25.7	1.8		14.5	0.9		1.22	0.15
Kearl	5	19.2	4.7		11.3	0.3		0.31	0.14

Set 1
244 calibration files
100 validation files

	All Data					
	Raw (noPT)	2nd deriv. GapSeg7-5	MSC	SNV	OSC-Solids	2nd deriv. GapSeg7-5 + SNV
PC-1	67.1	60.7	83.3	83.0	94.7	60.7
PC-2	87.7	86.5	92.2	92.0	96.4	86.5
PC-3	95.3	90.6	96.9	96.7	97.4	90.6
PC-4	96.9	93.7	97.9	97.7	98.4	93.7
PC-5	97.9	95.1	98.7	98.6	98.7	95.1
PC-6	98.5	96.3	99.0	98.8		96.3
PC-7	99.1	97.0	99.1	99.2		97.0
# of suggested components	4	6	4	4	3	6
	97.9	96.3	97.9	97.7	97.4	96.3

Set 2
34 calibration files
34 validation files

	Averaged (Reduced) Data					
	Raw (noPT)	2nd deriv. GapSeg7-5	MSC	SNV	OSC-Solids	2nd deriv. GapSeg7-5 + SNV
PC-1	70.9	62.7	84.3	84.0	96.0	62.7
PC-2	88.9	88.5	93.2	93.0	97.4	88.5
PC-3	96.5	92.3	97.6	97.4	98.4	92.3
PC-4	97.6	95.4	98.5	98.3	99.0	95.4
PC-5	98.4	96.7	99.2	99.0	99.2	96.7
PC-6	99.0	97.9	99.4	99.3	99.3	97.9
PC-7	99.4	98.4	99.6	99.5	99.5	98.4
# of suggested components	4	6	3	3	2	6
	97.6	97.9	97.6	97.4	97.4	97.9

Table 4.4 Principal component analysis of the data **Set 1** (244 calibration and 100 validation files) and data **Set 2** (34 calibration files and 34 validation files) in the 4000 to 700 cm^{-1} region. Results are presented for several pre-processing treatments. "Raw" data means no pre-processing was performed.

Solids Prediction - Validation Outputs - R^2 (reduced)

Number of components	Raw	2D_GapSeg7-5	MSC	SNV	OSC-Solids	2D GapSeg7-5 + SNV
#0	0	0	0	0	0	0
#1	0.65	0.80	0.65	0.65	0.80	0.84
#2	0.79	0.83	0.80	0.80	0.93	0.88
#3	0.81	0.89	0.85	0.85	0.92	0.94
#4	**0.92**	0.92	0.91	0.91	0.94	**0.95**
#5	0.93	**0.94**	**0.92**	**0.92**	**0.96**	0.95
#6	0.94	0.94	0.93	0.93	0.97	0.95
#7	0.95	0.94	0.93	0.93	0.97	0.96

Solids Prediction - Validation Outputs - RMSE (reduced)

Number of components	Raw	2D_GapSeg7-5	MSC	SNV	OSC-Solids	2D GapSeg7-5 + SNV
#0	7.69	7.69	7.69	7.69	7.69	7.69
#1	4.57	3.48	4.55	4.54	3.48	3.04
#2	3.57	3.21	3.44	3.44	2.10	2.70
#3	3.34	2.59	3.02	3.03	2.12	1.95
#4	**2.16**	2.13	2.37	2.37	1.81	**1.78**
#5	2.09	**1.91**	**2.12**	**2.15**	**1.53**	1.65
#6	1.95	1.94	2.03	2.04	1.40	1.72
#7	1.80	1.86	2.07	2.07	1.38	1.61

Table 4.5 Partial least squares analysis of Set 2 prediction of solids content using various pre-treatments.

MBI Prediction - Validation Outputs - R^2 (reduced)

Number of components	Raw	2D_GapSeg7-5	MSC	SNV	OSC-Solids	2D GapSeg7-5 + SNV
#0	0.00	0.00	0.00	0.00	0.00	0.00
#1	0.23	0.15	0.21	0.22	0.64	0.23
#2	0.42	0.29	0.42	0.42	0.85	0.33
#3	0.48	0.65	0.62	0.65	0.88	0.75
#4	0.78	0.84	0.79	0.83	**0.90**	**0.86**
#5	0.86	0.87	**0.89**	**0.89**	0.89	0.86
#6	**0.89**	**0.88**	0.90	0.90	0.87	0.88
#7	0.90	0.88	0.90	0.90	0.87	0.88

MBI Prediction - Validation Outputs - RMSE (reduced)

Number of components	Raw	2D_GapSeg7-5	MSC	SNV	OSC-Solids	2D GapSeg7-5 + SNV
#0	2.48	2.48	2.48	2.48	2.48	2.48
#1	2.18	2.29	2.21	2.20	1.52	2.19
#2	1.89	2.09	1.90	1.90	0.98	2.04
#3	1.79	1.47	1.53	1.46	0.86	1.25
#4	1.19	1.00	1.14	1.02	**0.80**	**0.92**
#5	0.93	0.91	**0.82**	**0.82**	0.84	0.92
#6	**0.82**	**0.86**	0.78	0.79	0.89	0.85
#7	0.80	0.86	0.80	0.78	0.91	0.86

Table 4.6 Partial least squares (PLS) analysis of **Set 2** for prediction of MBI using different pre-treatments.

Bitumen Prediction - Validation Outputs - R^2 (reduced)

Number of components	Raw	2D_GapSeg7-5	MSC	SNV	OSC-Bitumen	2D GapSeg7-5 + SNV
#0	0.00	0.00	0.00	0.00	0.00	0.00
#1	0.45	0.29	0.43	0.43	0.72	0.38
#2	0.59	0.50	0.66	0.66	0.83	0.51
#3	0.68	0.70	0.72	0.71	0.84	0.76
#4	0.81	0.86	0.80	0.80	0.82	0.85
#5	**0.84**	0.86	0.84	**0.85**	0.83	**0.87**
#6	0.82	0.89	**0.86**	0.85	0.86	0.86
#7	0.82	**0.90**	0.84	0.84	**0.90**	0.88

Bitumen Prediction - Validation Outputs - RMSE (reduced)

Number of components	Raw	2D_GapSeg7-5	MSC	SNV	OSC-Bitumen	2D GapSeg7-5 + SNV
#0	1.30	1.30	1.30	1.30	1.30	1.30
#1	0.97	1.10	0.98	0.98	0.70	1.02
#2	0.84	0.92	0.77	0.77	0.54	0.91
#3	0.75	0.72	0.70	0.70	0.52	0.65
#4	0.57	0.50	0.58	0.58	0.59	0.51
#5	**0.53**	0.50	0.52	**0.51**	0.56	**0.48**
#6	0.57	0.45	**0.50**	0.51	0.51	0.51
#7	0.58	**0.42**	0.53	0.53	**0.43**	0.47

Table 4.7 Partial least squares analysis of **Set 2** in the 4000 to 700 cm^{-1} region for various pre-treatments.

APPENDIX I: SUBSAMPLING MFTS FROM SOURCE BUCKETS

1. PURPOSE

1.1 This standard operating procedure describes collecting uniform MFT subsamples and specimen for the purpose of laboratory testing from the buckets where MFT is usually stored in the lab or shipped in.

2. SCOPE

2.1 MFTs usually have bituminous blobs and a sheen of oil that tends to float to the surface. Therefore, for consistent sampling, subsamples and test specimen must be collected after through mixing of the bucket using either an engineering paint shaker or manually before opening the lid. Further stirring using magnetic stirrer during subsampling is usually necessary after opening the bucket and during subsampling particularly for MFTs with low solids content and viscosity.

3. SAMPLE HANDLING

3.1 Refer to relevant MSDS information.
3.2 MFTs should not be stored in an area exposed to extreme heat/cold for extended periods of time.
3.3 It is best to inspect MFTs periodically and note if the MFT generates gas and pushes material out of the storage buckets.
3.4 Sample should not be left uncovered for a long period of time that might lead to drying or left exposed to the elements or dust. Do your best to minimize contamination of the main sample stockpile.

4. MATERIALS AND EQUIPMENT

4.1 Magnetic stirrer
4.2 2 in stir bar
4.3 Beaker or container of appropriate size for subsample
4.4 Engineering paint shaker suitable for the size of the source buckets
4.5 Alconox or Sparkleen
4.6 Sponge and/or brush for cleaning
4.7 Acetone
4.8 Metal Spatula 8”

5. REAGENTS

5.1 N/A

6. STANDARDS

6.1 N/A

7. ENVIRONMENT, HEALTH AND SAFETY

7.1 Wear standard laboratory personal protective equipment (PPE) as defined by the Laboratory Organizational Rules.
7.2 Refer to the appropriate material safety data sheets (MSDS) for additional information.
7.3 It is the responsibility of the lab technician to read any manuals available for equipment they are using to determine any potential dangers.

8. INTERFERENCES

8.1 NA

9. QUALITY CONTROL

9.1 NA

10. PROCEDURE

10.1 Inspect the bucket prior to mixing for damage, insecure lid, etc. and make sure MFT will not leak during mixing.
10.2 Fasten the container to the paint shaker and mix for 5 minutes. In case a paint shaker is not available the buckets can be mixed manually. In that case shake the bucket for 5 minutes while holding the bottom of the bucket up.
10.3 Place the bucket on the counter and open the lid. Inspect the bottom of the container by scraping it with the spatula or glass rod. If there is still a thick layer of unmixed mud sticking to the bottom, repeat the mixing process. If an engineering paint mixer is used, the mixing is very efficient, and it is unlikely that the mixing has to be repeated.
10.4 After opening the lid, if there is not a visible oil sheen or excess of bitumen blobs on the surface, transfer required amount of MFT into your beaker for your experiment (This is usually the case if the MFT has high solids content and is viscous enough). Otherwise, place the container on a magnetic stirrer with the stir bar and mix till a vortex can be seen on the surface. Once the vortex disperses the oil and bitumen blobs, MFT can be subsampled in a consistent manner at this point.

11. CALCULATIONS AND DATA REPORTING

11.1 NA

12. TEST METHOD VALIDATION

12.1 N/A

13. PREVENTIVE MAINTENANCE

13.1 Cleaning the MFT subsample container
13.1.1. Add appropriate amount of Alconox or Sparkleen to water in a separate beaker or container.
13.1.2. First rinse the glassware and stir bar that are contaminated with MFT using water to get rid of solids as much as possible. Soak sponges in the Alconox mix and clean using this sponge.
13.1.3. Rinse with water 3 times. Rinse again with DI-water 3 times.

13.1.4. If there is any difficult bitumen still on the equipment pour some Acetone on the brush and scrub carefully to remove. Then rinse again with DI-water.

14. REFERENCES

14.1 N/A

15. REVISION HISTORY

15.1 N/A

APPENDIX II: HATR SPECTROSCOPY

1. PURPOSE

1.1 This standard operating procedure describes the process and settings used for collecting FTIR spectra of MFT specimen using the Horizontal Attenuated Total Reflection technique (HATR).

2. SCOPE

2.1 In this case, FTIR spectra were obtained using a Thermo Scientific 6700 FTIR spectrometer using an MCT detector. However, the fundamental aspects are the same and other researchers should be able to use this SOP with other spectrometers with HATR cell.
2.2 A method for obtaining consistent specimen for the FTIR machine is discussed.

3. SAMPLE HANDLING

3.1 Refer to relevant MSDS information.

4. MATERIALS AND EQUIPMENT

4.1 Magnetic stirrer
4.2 2 inch stir bar
4.3 250 mL Beaker or Erlenmeyer
4.4 Watch glass to cover the beaker/Erlenmeyer
4.5 5 mL or 10 mL mechanical pipette
4.6 Appropriate disposable pipette tips for the pipette
4.7 Alconox or Sparkleen
4.8 Sponge and/or brush for cleaning
4.9 Ethanol
4.10 DI water
4.11 Lint free wipes
4.12 Cotton swaps or Q-tips

5. REAGENTS

5.1 N/A

6. STANDARDS

6.1 N/A

7. ENVIRONMENT, HEALTH AND SAFETY

7.1 Wear standard laboratory personal protective equipment (PPE) as defined by the Laboratory Organizational Rules.
7.2 Refer to the appropriate material safety data sheets (MSDS) for additional information.
7.3 It is the responsibility of the lab technician to read any manuals available for equipment they are using to determine any potential dangers.

8. INTERFERENCES

8.1 NA

9. QUALITY CONTROL

9.1 NA

10. PROCEDURE

10.1 Setting up the FTIR machine:

10.1.1. MCT/A detector needs to be cooled. Therefore, use Liquid Nitrogen and turn on the air purge to the machine and wait until the energy picked up by the sensor is stable.
10.1.2. KBr beam splitter is used in the examples described in the SOP
10.1.3. IR light source is used in the examples described in the SOP
10.1.4. Horizontal ATR cell with ZnSe window is used in the examples described in the SOP
10.1.5. Wavenumbers within 650 and 4000 range is used in the examples described in the SOP
10.1.6. Aperture of 50 and screen wheel of 20% is used in the examples described in the SOP
10.1.7. Using these settings with the spectrometer used, provides the detector with acceptable range of input energy.
10.1.8. A total of 64 scans were co-added at 2 cm-1 resolution for each spectrum and a reference background was obtained from an empty cell prior to each test. Because of the heterogeneous nature of MFT each MFT is tested 10x replicates.

10.2 Samples:

10.2.1. Pour 200 mL of MFT in a beaker or Erlenmeyer (please refer to the SOP on "Subsampling MFTs from source buckets" to ensure the subsample is representative of the MFT in the source bucket).
10.2.2. Place the container on a magnetic stirrer with the stir bar and adjust the speed until a vortex can be seen on the surface. Once the vortex disperses the oil and bitumen blobs, consistent MFT specimen can be collected with a pipette.
10.2.3. Set the mechanical pipette to its maximum volume capacity, fill the pipette tip and empty back into the beaker 3 times. This will ensure that the inner surface of the pipette tip is covered with MFT. Experience showed that oil and bitumen in the MFT tend to coat the inner surface of the pipette tip quickly, causing the FTIR spectra to show lower organic bands in the first pour if a clean pipette tip is used.
10.2.4. Once the tip is rinsed with the MFT, use the same tip for the rest of the test repeats of the same MFT.

10.3 Collecting FTIR spectra:

10.3.1. Collect background spectra with an empty cell before MFT is poured in HATR cell trough.
10.3.2. Take ~2.5mL of MFT using the mechanical pipette

10.3.3. Clean the tip of the pipette in case there are wet bitumen droplets hanging from the pipette
10.3.4. Pour the specimen into the HATR trough by dispensing and moving the pipette tip from one side of the trough to the next at a consistent rate. (Make sure that the pipette tip does not touch the HATR cell window at any moment otherwise bitumen can be smeared on the window and the spectra will show higher organic bands)
10.3.5. Collect the spectra with the specimen.

10.4 Cleaning the HATR cell:
10.4.1. Take the HATR cell trough out of the FTIR machine.
10.4.2. Pour MFT out by tilting the trough into a sink or a large beaker and use a wash bottle with DI water to rinse the trough until MFT particles are washed away.
10.4.3. Pour 1 mL of ethanol in the trough and use lint free wipes to clean the window thoroughly. A cotton swap might be used for the corners that are harder to wipe.
10.4.4. If necessary, repeat cleaning with ethanol until the window is clean
10.4.5. During this stage it is essential to make sure none of the MFT, water or Ethanol contaminates the other side of the window or go inside the HATR cell chamber.

11. CALCULATIONS AND DATA REPORTING

11.1 NA

12. TEST METHOD VALIDATION

12.1 N/A

13. PREVENTIVE MAINTENANCE

13.1 Cleaning the 250 mL beaker and watch glass
13.1.1. Add appropriate amount of Alconox or Sparkleen to water in a separate beaker or container.
13.1.2. First rinse the glassware and stir bar that are contaminated with MFT using water to get rid of solids as much as possible. Soak sponges in the Alconox mix and clean using this sponge.
13.1.3. Rinse with water 3 times. Rinse again with DI-water 3 times.
13.1.4. If there is any difficult bitumen still on the equipment pour some Acetone on the spot and on a brush and scrub carefully to remove. Then rinse again with DI-water.

13.2 Keeping the HATR cell clean after the test
13.2.1 Care must be taken in making sure that the FTIR chamber is not contaminated with water, solvents or MFT

14. REFERENCES

14.1 N/A

15. REVISION HISTORY

15.1 N/A

APPENDIX III: COLLECTED MFT SPECTRA

Figure AIII.1. ATR-FTIR spectra of ES2356 in the 4000 to 700 cm-1 region. Each individual spectrum is shown in gray and the averaged spectrum is represented by the dashed black line.

Figure AIII.2. ATR-FTIR spectra of ES2787 in the 4000 to 700 cm-1 region. Each individual spectrum is shown in gray and the averaged spectrum is represented by the dashed black line.

Figure AIII.3. ATR-FTIR spectra of ES2790 in the 4000 to 700 cm-1 region. Each individual spectrum is shown in gray and the averaged spectrum is represented by the dashed black line.

Figure AIII.4. ATR-FTIR spectra of ES2791 in the 4000 to 700 cm-1 region. Each individual spectrum is shown in gray and the averaged spectrum is represented by the dashed black line.

Figure AIII.5. ATR-FTIR spectra of ES4364 in the 4000 to 700 cm-1 region. Each individual spectrum is shown in gray and the averaged spectrum is represented by the dashed black line.

Figure AIII.6. ATR-FTIR spectra of ES4367 in the 4000 to 700 cm-1 region. Each individual spectrum is shown in gray and the averaged spectrum is represented by the dashed black line.

Figure AIII.7. ATR-FTIR spectra of ES4368 in the 4000 to 700 cm-1 region. Each individual spectrum is shown in gray and the averaged spectrum is represented by the dashed black line.

Figure AIII.8. ATR-FTIR spectra of ES7370 in the 4000 to 700 cm-1 region. Each individual spectrum is shown in gray and the averaged spectrum is represented by the dashed black line.

Figure AIII.9. ATR-FTIR spectra of ES4371 in the 4000 to 700 cm-1 region. Each individual spectrum is shown in gray and the averaged spectrum is represented by the dashed black line.

Figure AIII.10. ATR-FTIR spectra of ES4372 in the 4000 to 700 cm-1 region. Each individual spectrum is shown in gray and the averaged spectrum is represented by the dashed black line.

Figure AIII.11. ATR-FTIR spectra of ES4374 in the 4000 to 700 cm-1 region. Each individual spectrum is shown in gray and the averaged spectrum is represented by the dashed black line.

Figure AIII.12. ATR-FTIR spectra of ES4375 in the 4000 to 700 cm-1 region. Each individual spectrum is shown in gray and the averaged spectrum is represented by the dashed black line.

Figure AIII.13. ATR-FTIR spectra of ES4376 in the 4000 to 700 cm-1 region. Each individual spectrum is shown in gray and the averaged spectrum is represented by the dashed black line.

Figure AIII.14. ATR-FTIR spectra of ES4525 in the 4000 to 700 cm-1 region. Each individual spectrum is shown in gray and the averaged spectrum is represented by the dashed black line.

Figure AIII.15. ATR-FTIR spectra of ES4526 in the 4000 to 700 cm-1 region. Each individual spectrum is shown in gray and the averaged spectrum is represented by the dashed black line.

Figure AIII.16. ATR-FTIR spectra of ES4528 in the 4000 to 700 cm-1 region. Each individual spectrum is shown in gray and the averaged spectrum is represented by the dashed black line.

Figure AIII.17. ATR-FTIR spectra of ES4529 in the 4000 to 700 cm-1 region. Each individual spectrum is shown in gray and the averaged spectrum is represented by the dashed black line.

Figure AIII.18. ATR-FTIR spectra of ES4530 in the 4000 to 700 cm-1 region. Each individual spectrum is shown in gray and the averaged spectrum is represented by the dashed black line.

Figure AIII.19. ATR-FTIR spectra of FFT#1 in the 4000 to 700 cm-1 region. Each individual spectrum is shown in gray and the averaged spectrum is represented by the dashed black line.

Figure AIII.20. ATR-FTIR spectra of FFT#3 in the 4000 to 700 cm-1 region. Each individual spectrum is shown in gray and the averaged spectrum is represented by the dashed black line.

Figure AIII.21. ATR-FTIR spectra of FFT#5 in the 4000 to 700 cm-1 region. Each individual spectrum is shown in gray and the averaged spectrum is represented by the dashed black line.

Figure AIII.22. ATR-FTIR spectra of FFT#7 in the 4000 to 700 cm-1 region. Each individual spectrum is shown in gray and the averaged spectrum is represented by the dashed black line.

Figure AIII.23. ATR-FTIR spectra of FFT#9 in the 4000 to 700 cm-1 region. Each individual spectrum is shown in gray and the averaged spectrum is represented by the dashed black line.

Figure AIII.24. ATR-FTIR spectra of 2/3 in the 4000 to 700 cm-1 region. Each individual spectrum is shown in gray and the averaged spectrum is represented by the dashed black line.

Figure AIII.25. ATR-FTIR spectra of 2/3F in the 4000 to 700 cm-1 region. Each individual spectrum is shown in gray and the averaged spectrum is represented by the dashed black line.

Figure AIII.26. ATR-FTIR spectra of 8A in the 4000 to 700 cm-1 region. Each individual spectrum is shown in gray and the averaged spectrum is represented by the dashed black line.

Figure AIII.27. ATR-FTIR spectra of SHELL in the 4000 to 700 cm-1 region. Each individual spectrum is shown in gray and the averaged spectrum is represented by the dashed black line.

Figure AIII.28. ATR-FTIR spectra of STP in the 4000 to 700 cm-1 region. Each individual spectrum is shown in gray and the averaged spectrum is represented by the dashed black line.

Figure AIII.29. ATR-FTIR spectra of S1725 in the 4000 to 700 cm-1 region. Each individual spectrum is shown in gray and the averaged spectrum is represented by the dashed black line.

Figure AIII.30. ATR-FTIR spectra of S1727 in the 4000 to 700 cm-1 region. Each individual spectrum is shown in gray and the averaged spectrum is represented by the dashed black line.

Figure AIII.31. ATR-FTIR spectra of S1729 in the 4000 to 700 cm-1 region. Each individual spectrum is shown in gray and the averaged spectrum is represented by the dashed black line.

Figure AIII.32. ATR-FTIR spectra of S1730 in the 4000 to 700 cm-1 region. Each individual spectrum is shown in gray and the averaged spectrum is represented by the dashed black line. Figure AIII.33. ATR-FTIR spectra of S1731 in the 4000 to 700 cm-1 region. Each individual spectrum is shown in gray and the averaged spectrum is represented by the dashed black line.

Figure AIII.33. ATR-FTIR spectra of S1731 in the 4000 to 700 cm-1 region. Each individual spectrum is shown in gray and the averaged spectrum is represented by the dashed black line.

Figure AIII.34. ATR-FTIR spectra of S1734 in the 4000 to 700 cm-1 region. Each individual spectrum is shown in gray and the averaged spectrum is represented by the dashed black line.

Raw Spectra – Appendix III

Plus averaged curve in dashed black line

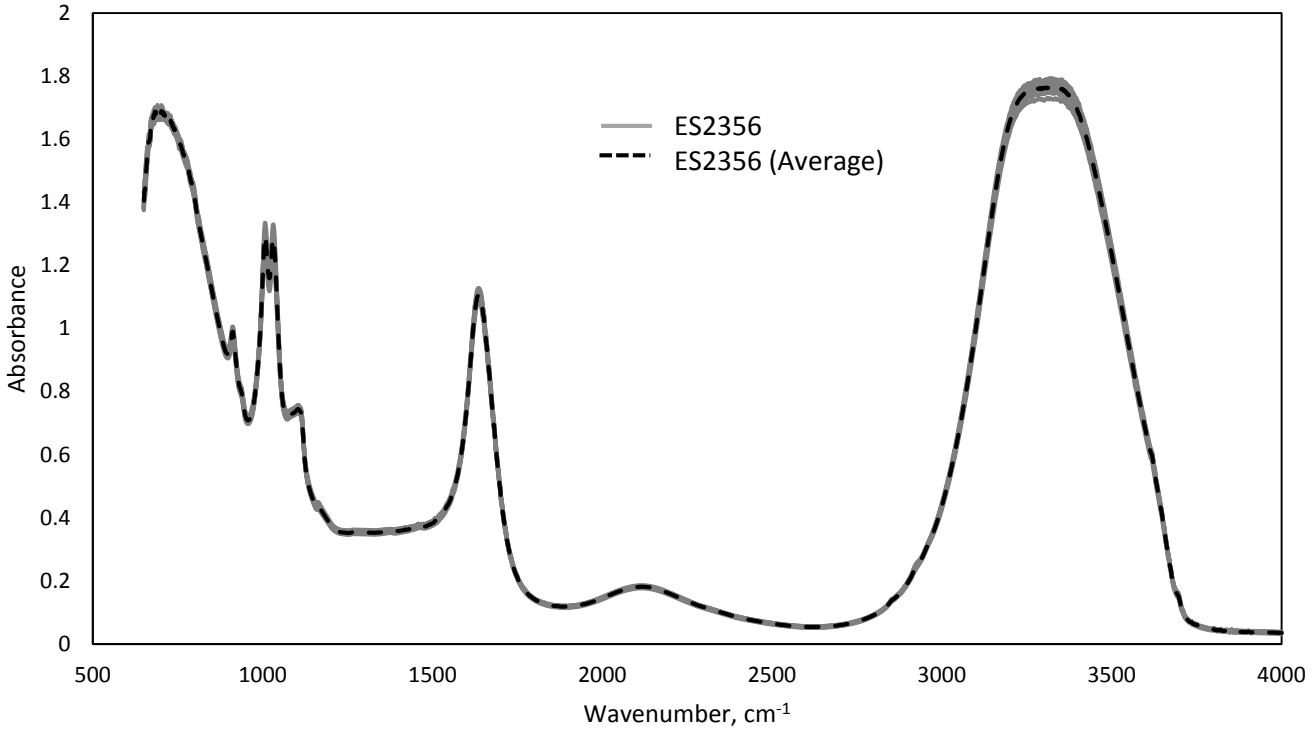

Figure AIII.1. ATR-FTIR spectra of ES2356 in the 4000 to 700 cm-1 region. Each individual spectrum is shown in gray and the averaged spectrum is represented by the dashed black line.

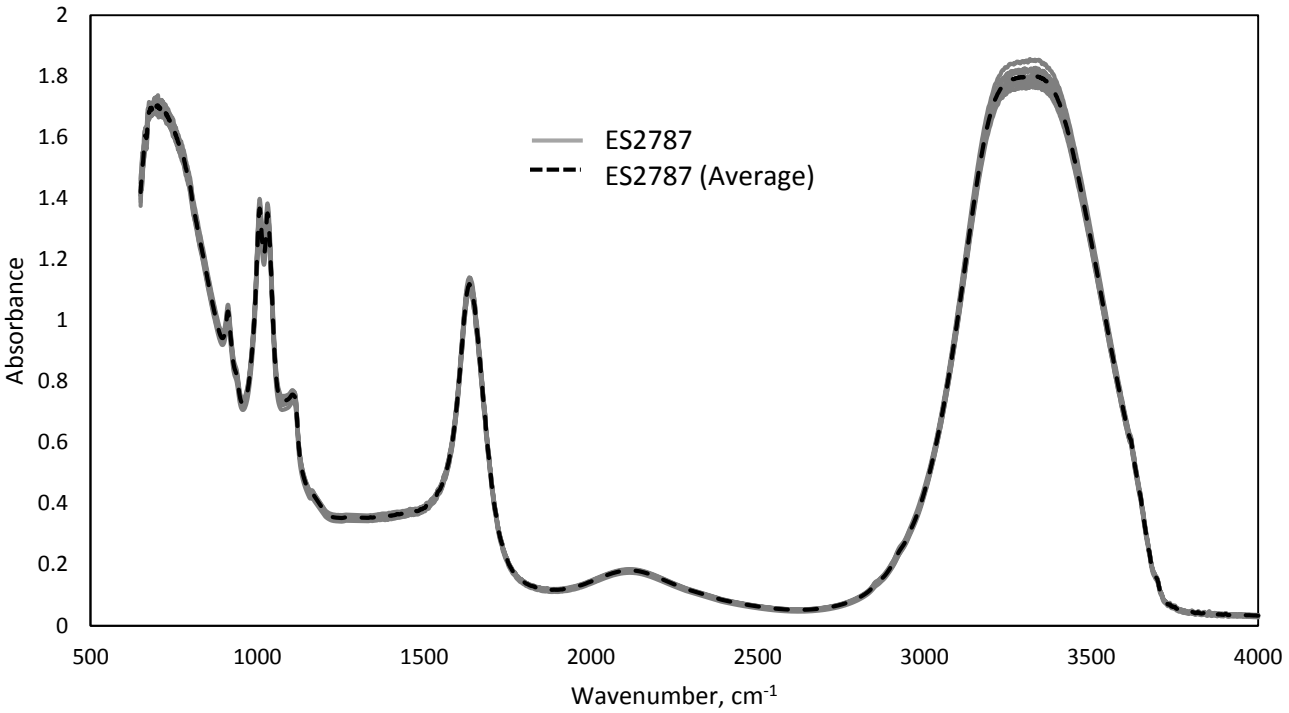

Figure AIII.2. ATR-FTIR spectra of ES2787 in the 4000 to 700 cm-1 region. Each individual spectrum is shown in gray and the averaged spectrum is represented by the dashed black line.

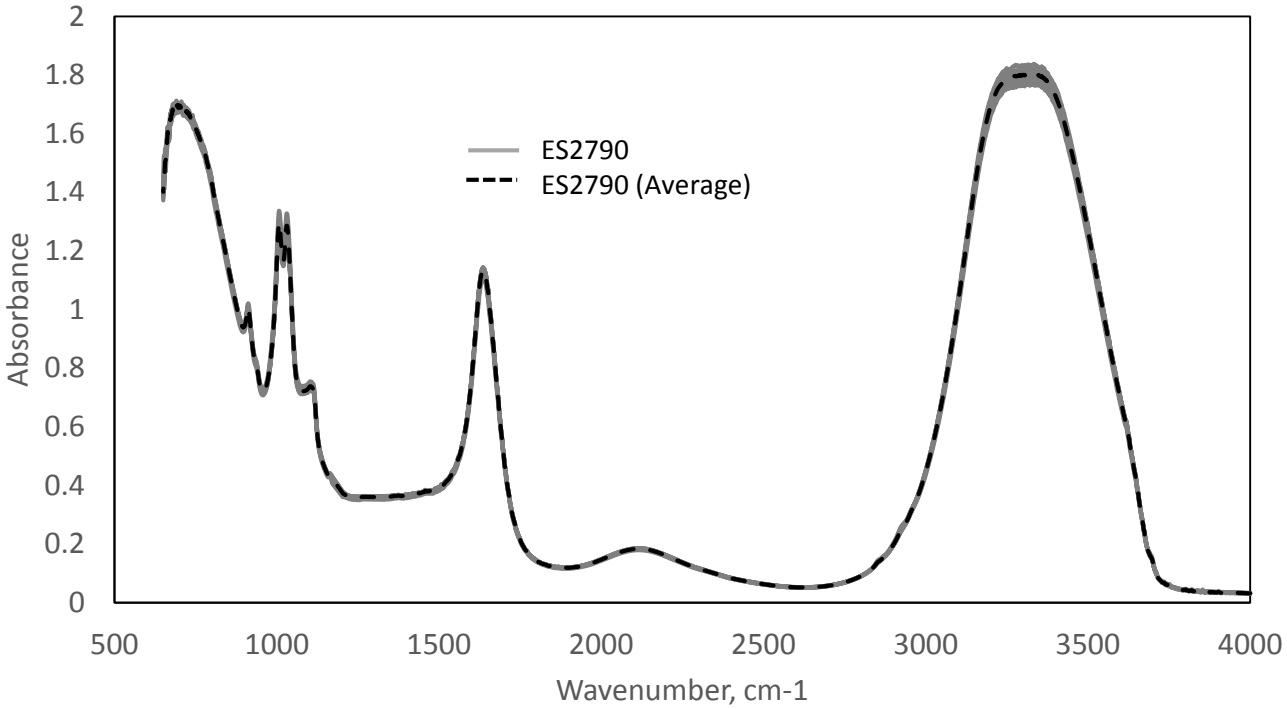

Figure AIII.3. ATR-FTIR spectra of ES2790 in the 4000 to 700 cm-1 region. Each individual spectrum is shown in gray and the averaged spectrum is represented by the dashed black line.

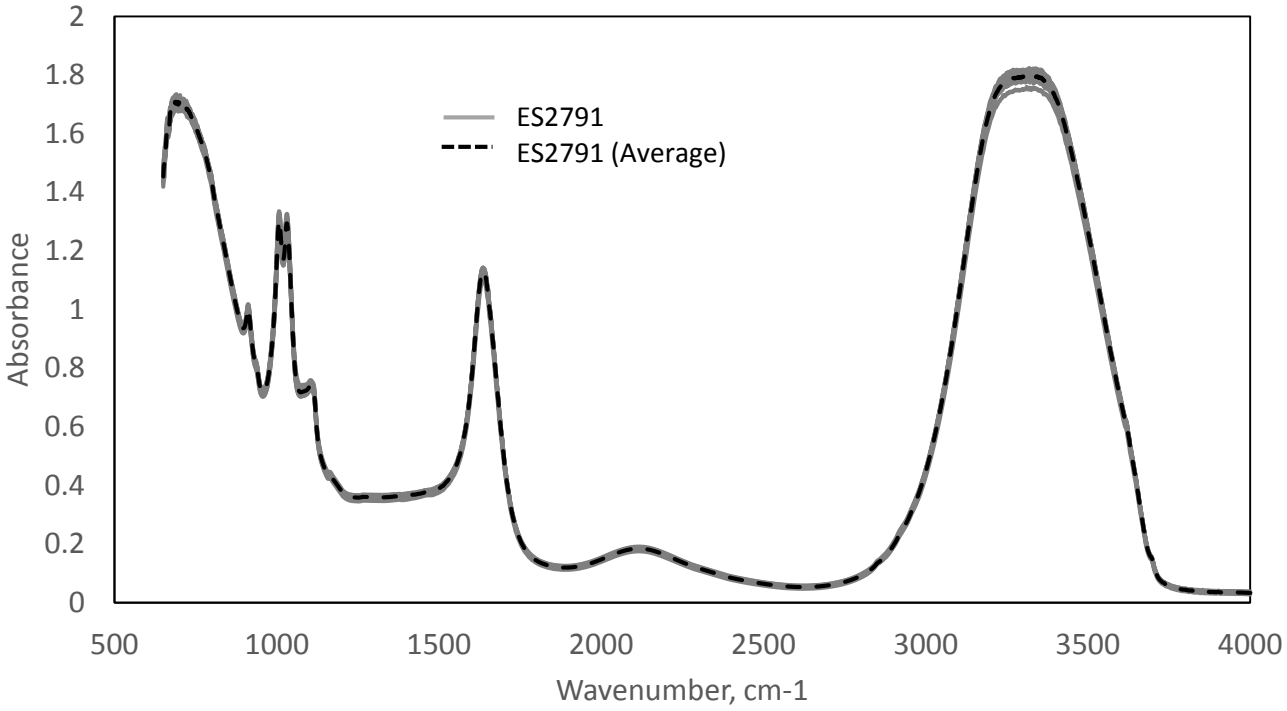

Figure AIII.4. ATR-FTIR spectra of ES2791 in the 4000 to 700 cm-1 region. Each individual spectrum is shown in gray and the averaged spectrum is represented by the dashed black line.

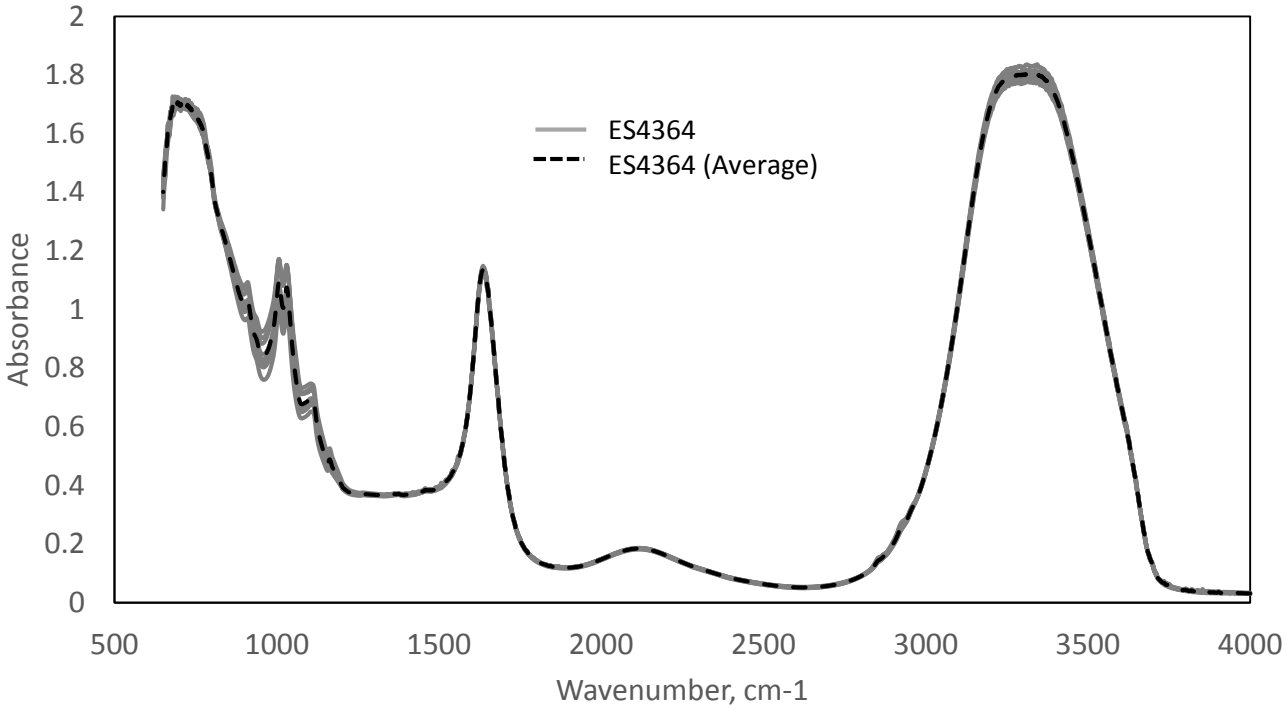

Figure AIII.5. ATR-FTIR spectra of ES4364 in the 4000 to 700 cm-1 region. Each individual spectrum is shown in gray and the averaged spectrum is represented by the dashed black line.

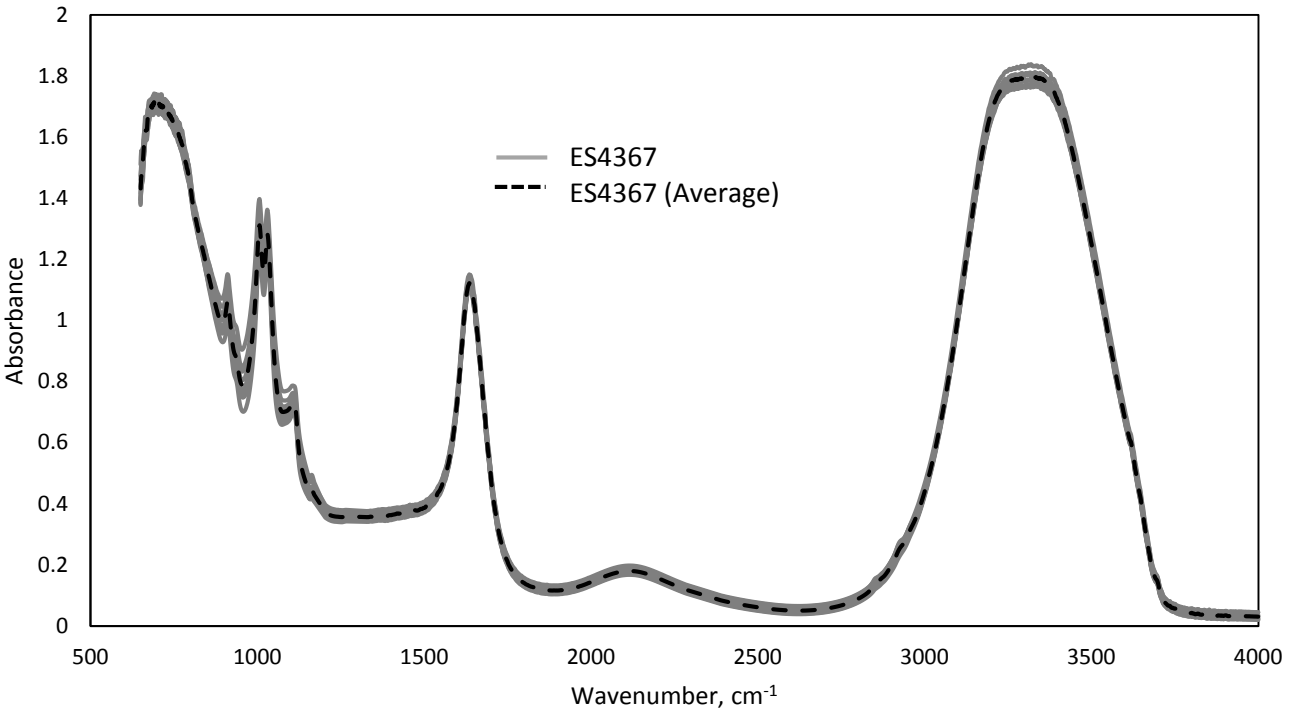

Figure AIII.6. ATR-FTIR spectra of ES4367 in the 4000 to 700 cm-1 region. Each individual spectrum is shown in gray and the averaged spectrum is represented by the dashed black line.

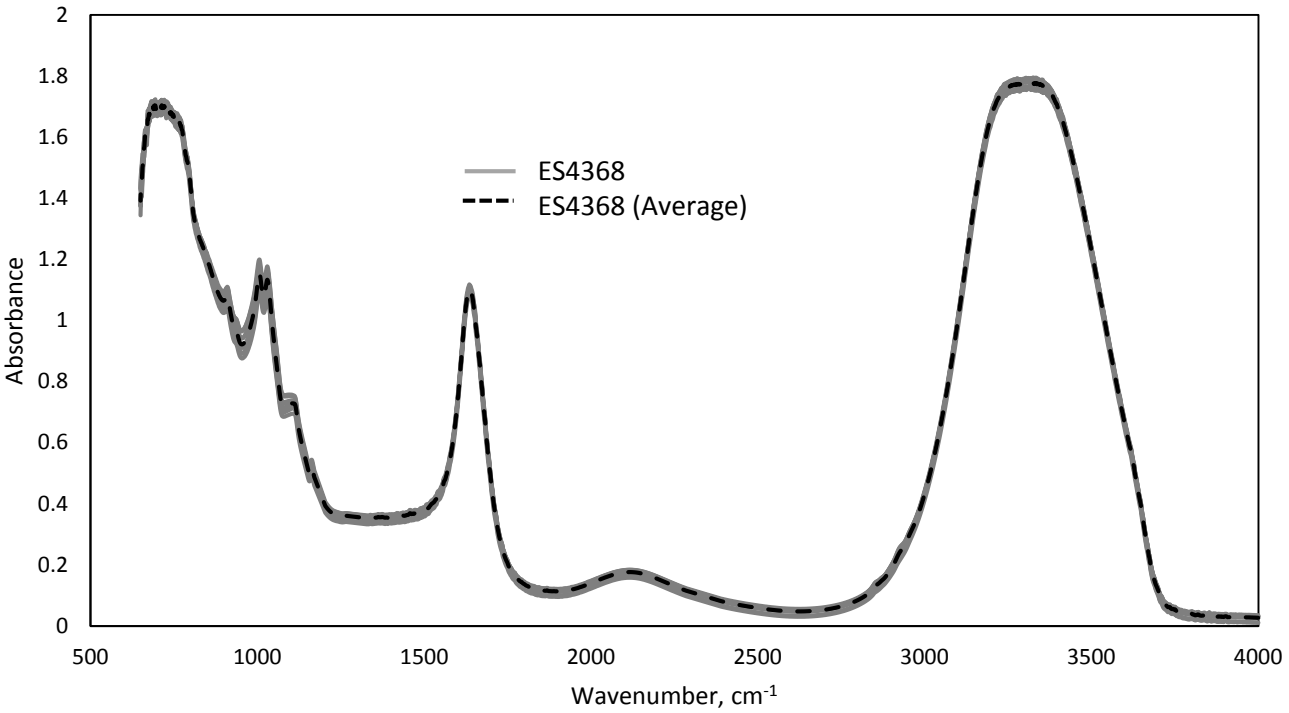

Figure AIII.7. ATR-FTIR spectra of ES4368 in the 4000 to 700 cm-1 region. Each individual spectrum is shown in gray and the averaged spectrum is represented by the dashed black line.

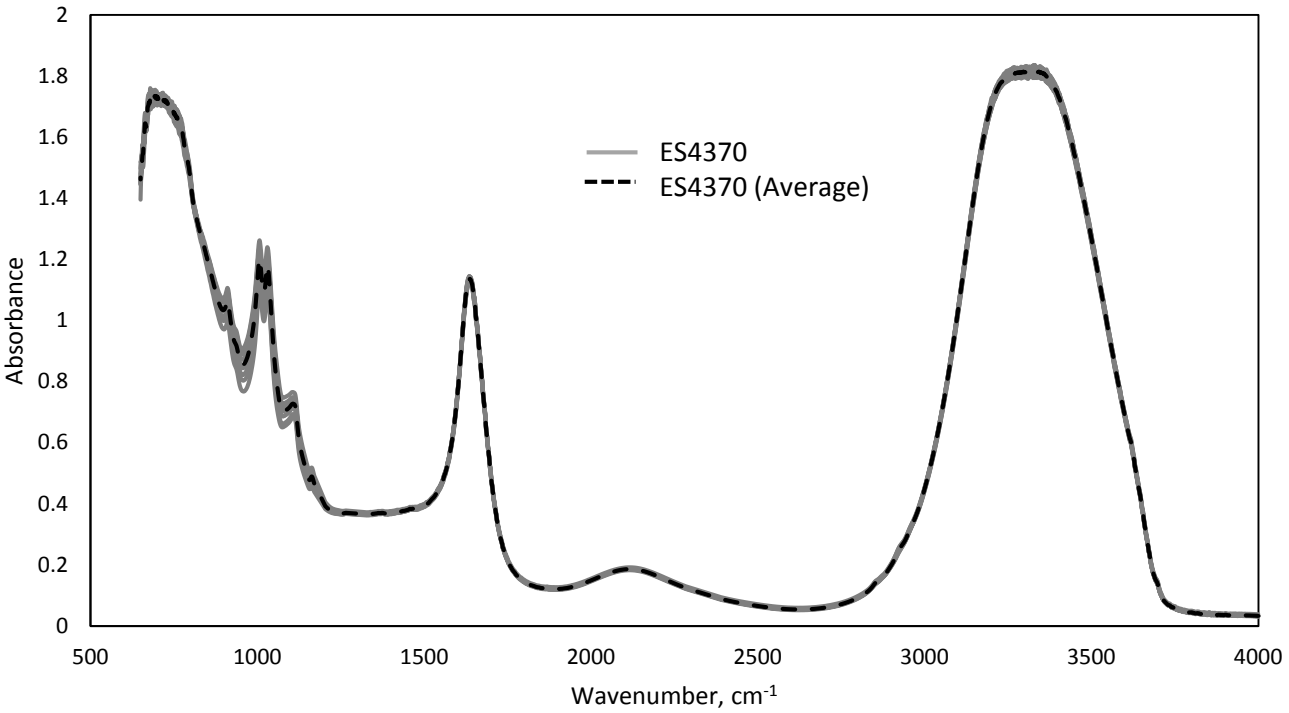

Figure AIII.8. ATR-FTIR spectra of ES7370 in the 4000 to 700 cm-1 region. Each individual spectrum is shown in gray and the averaged spectrum is represented by the dashed black line.

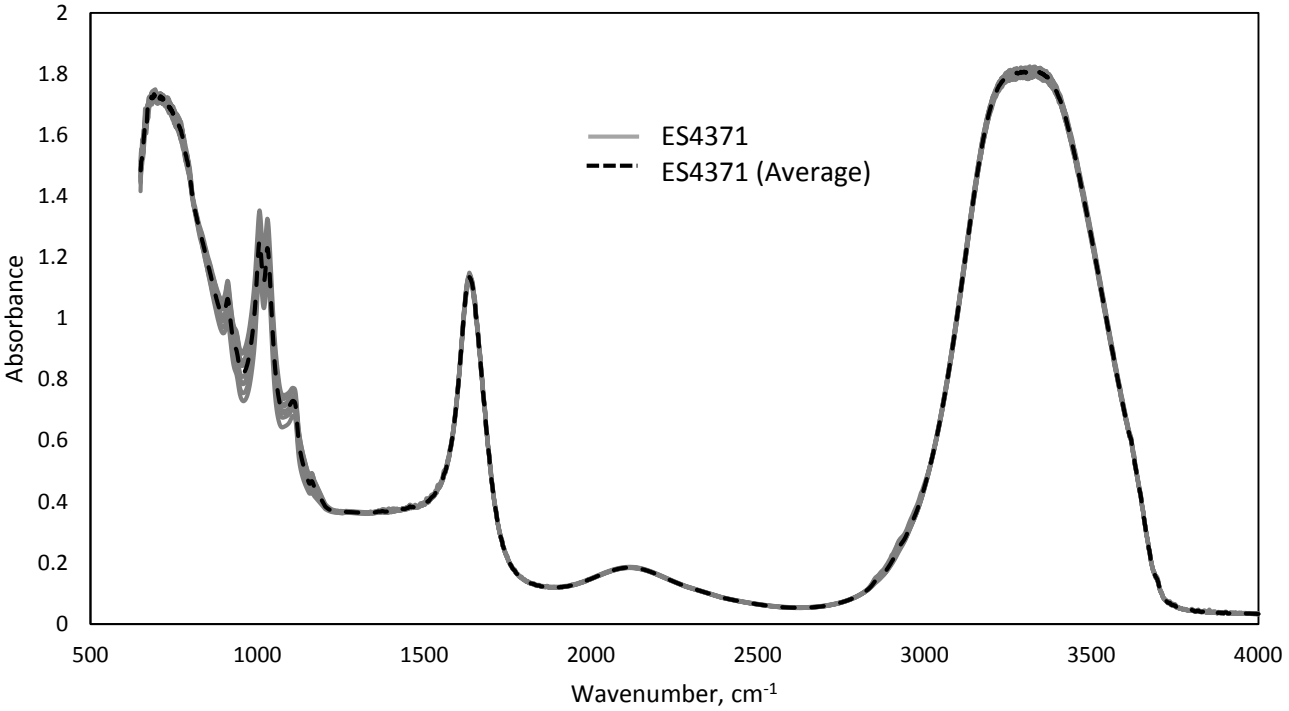

Figure AIII.9. ATR-FTIR spectra of ES4371 in the 4000 to 700 cm-1 region. Each individual spectrum is shown in gray and the averaged spectrum is represented by the dashed black line.

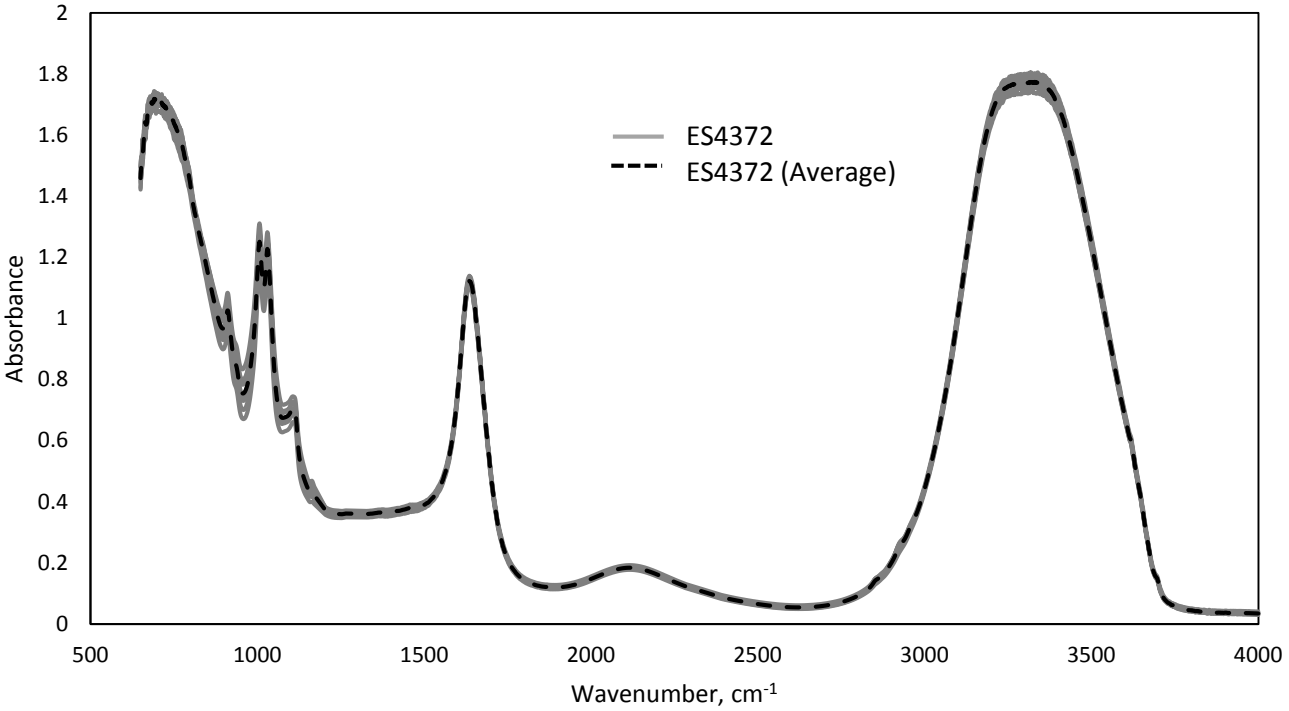

Figure AIII.10. ATR-FTIR spectra of ES4372 in the 4000 to 700 cm-1 region. Each individual spectrum is shown in gray and the averaged spectrum is represented by the dashed black line.

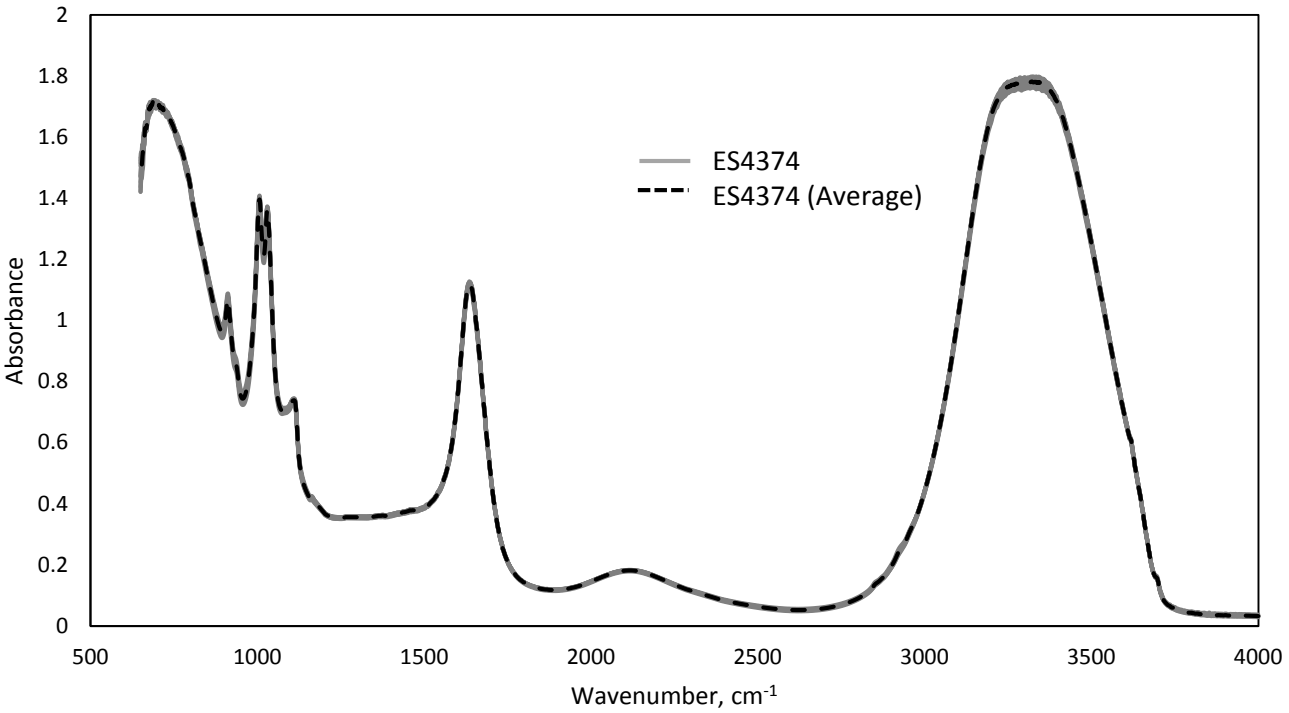

Figure AIII.11. ATR-FTIR spectra of ES4374 in the 4000 to 700 cm-1 region. Each individual spectrum is shown in gray and the averaged spectrum is represented by the dashed black line.

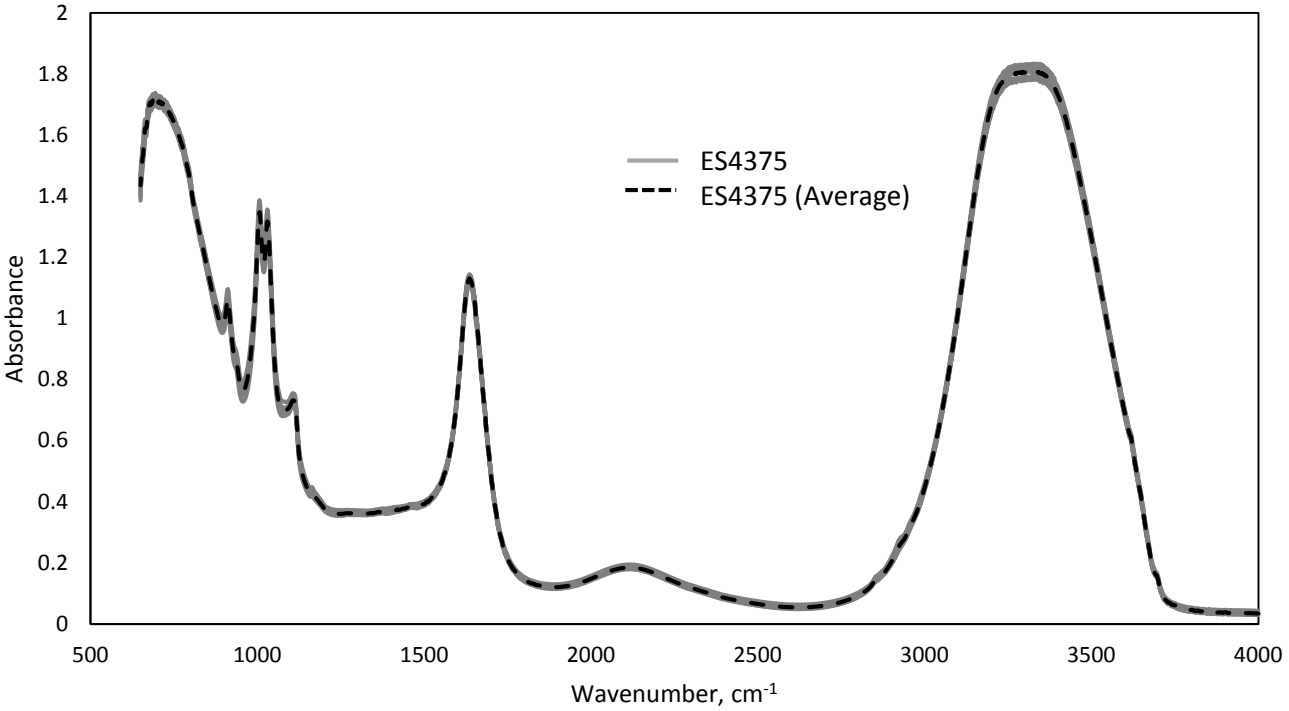

Figure AIII.12. ATR-FTIR spectra of ES4375 in the 4000 to 700 cm-1 region. Each individual spectrum is shown in gray and the averaged spectrum is represented by the dashed black line.

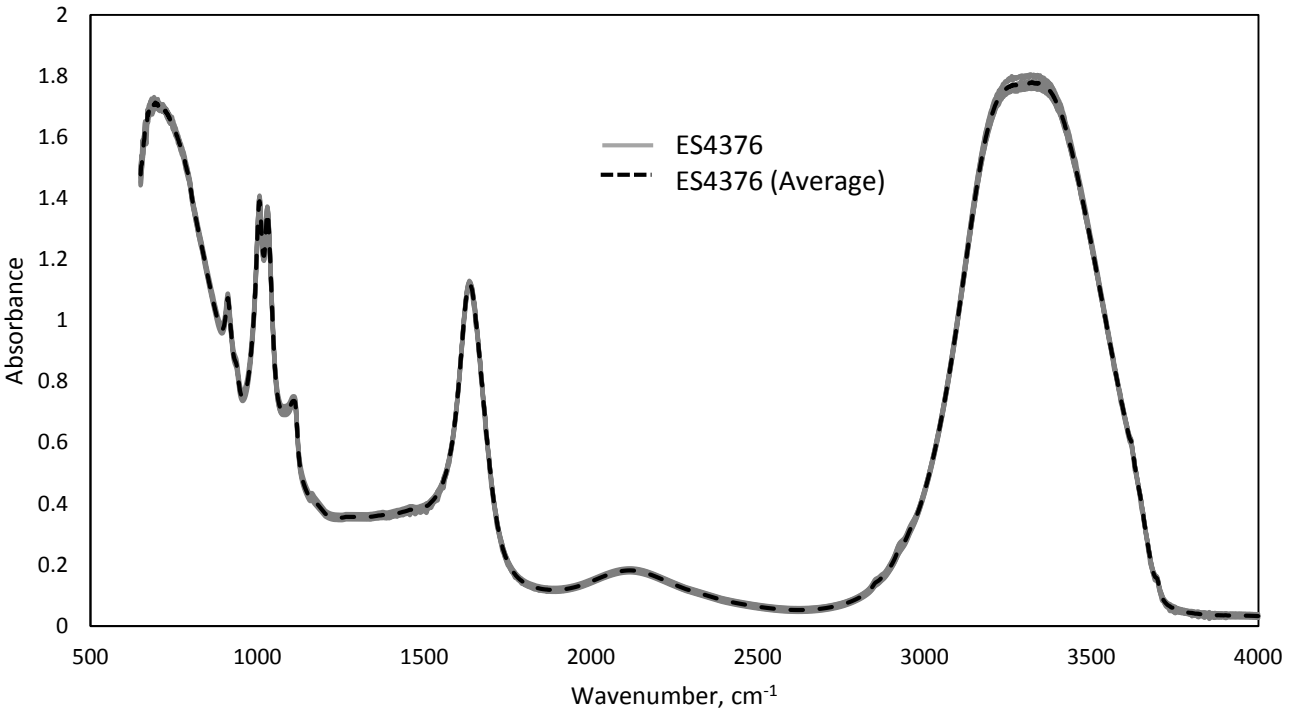

Figure AIII.13. ATR-FTIR spectra of ES4376 in the 4000 to 700 cm-1 region. Each individual spectrum is shown in gray and the averaged spectrum is represented by the dashed black line.

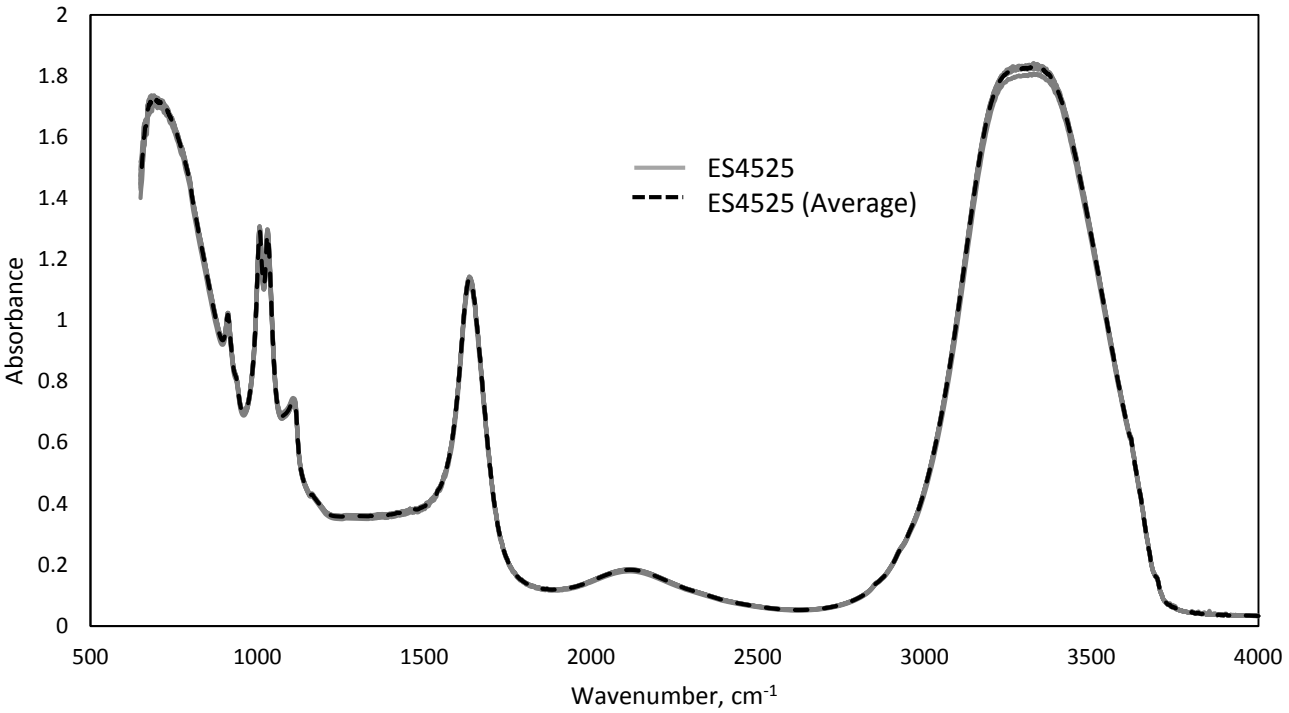

Figure AIII.14. ATR-FTIR spectra of ES4525 in the 4000 to 700 cm-1 region. Each individual spectrum is shown in gray and the averaged spectrum is represented by the dashed black line.

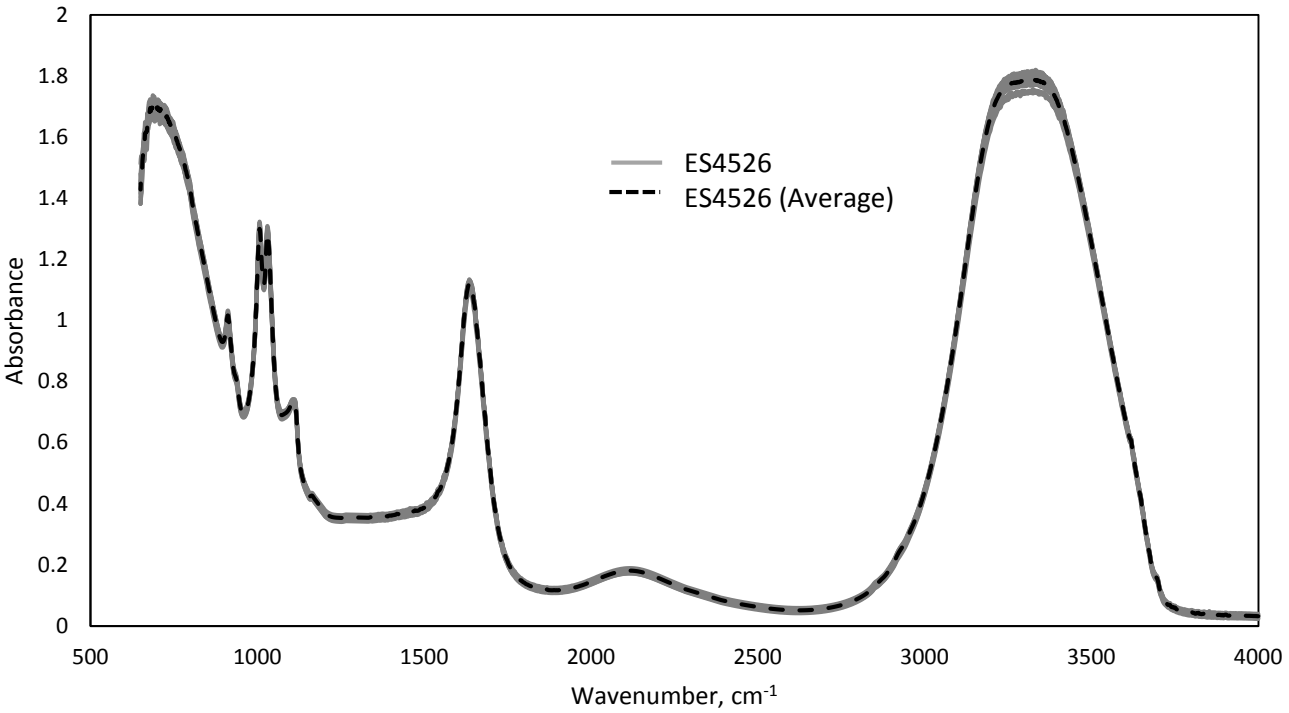

Figure AIII.15. ATR-FTIR spectra of ES4526 in the 4000 to 700 cm-1 region. Each individual spectrum is shown in gray and the averaged spectrum is represented by the dashed black line.

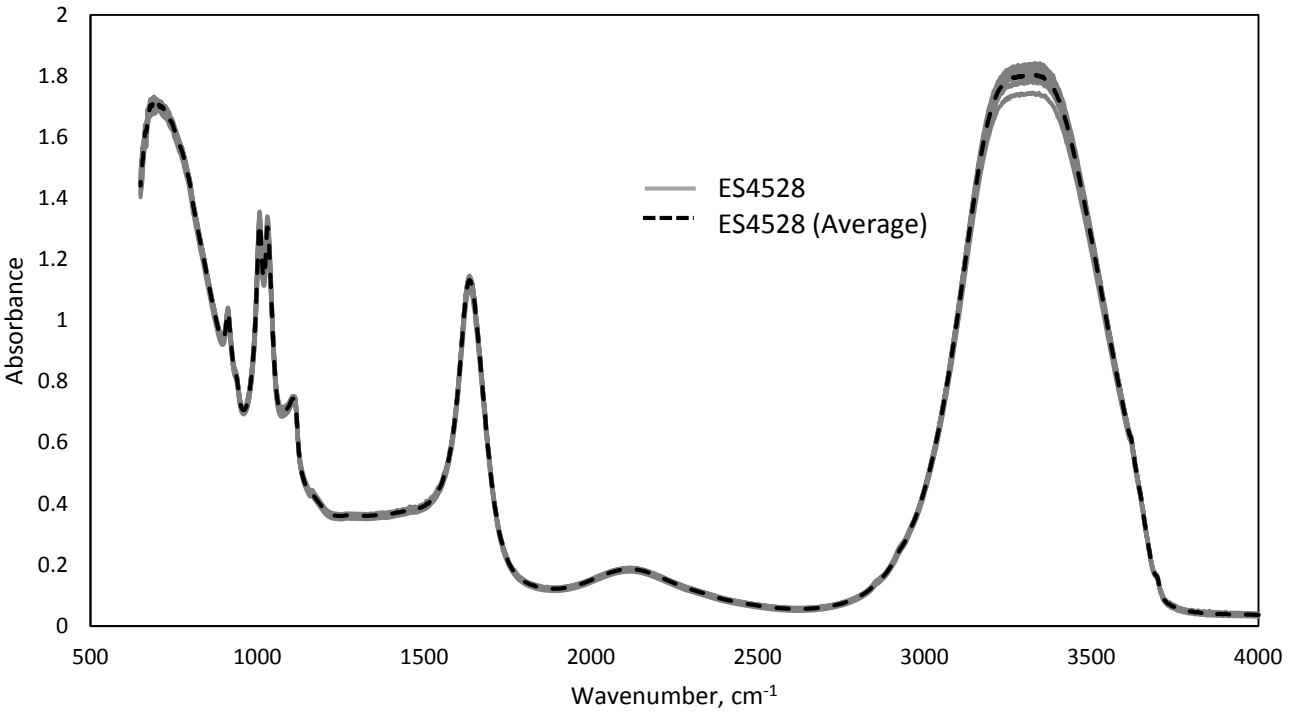

Figure AIII.16. ATR-FTIR spectra of ES4528 in the 4000 to 700 cm-1 region. Each individual spectrum is shown in gray and the averaged spectrum is represented by the dashed black line.

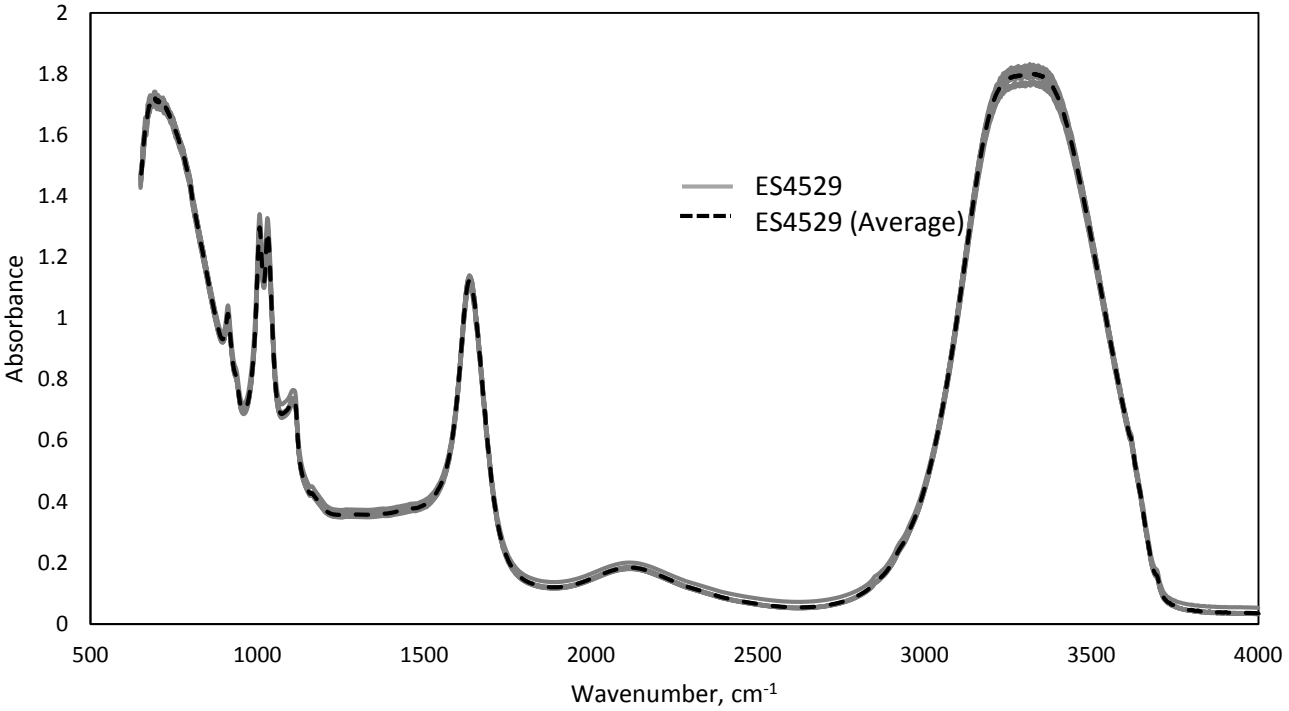

Figure AIII.17. ATR-FTIR spectra of ES4529 in the 4000 to 700 cm-1 region. Each individual spectrum is shown in gray and the averaged spectrum is represented by the dashed black line.

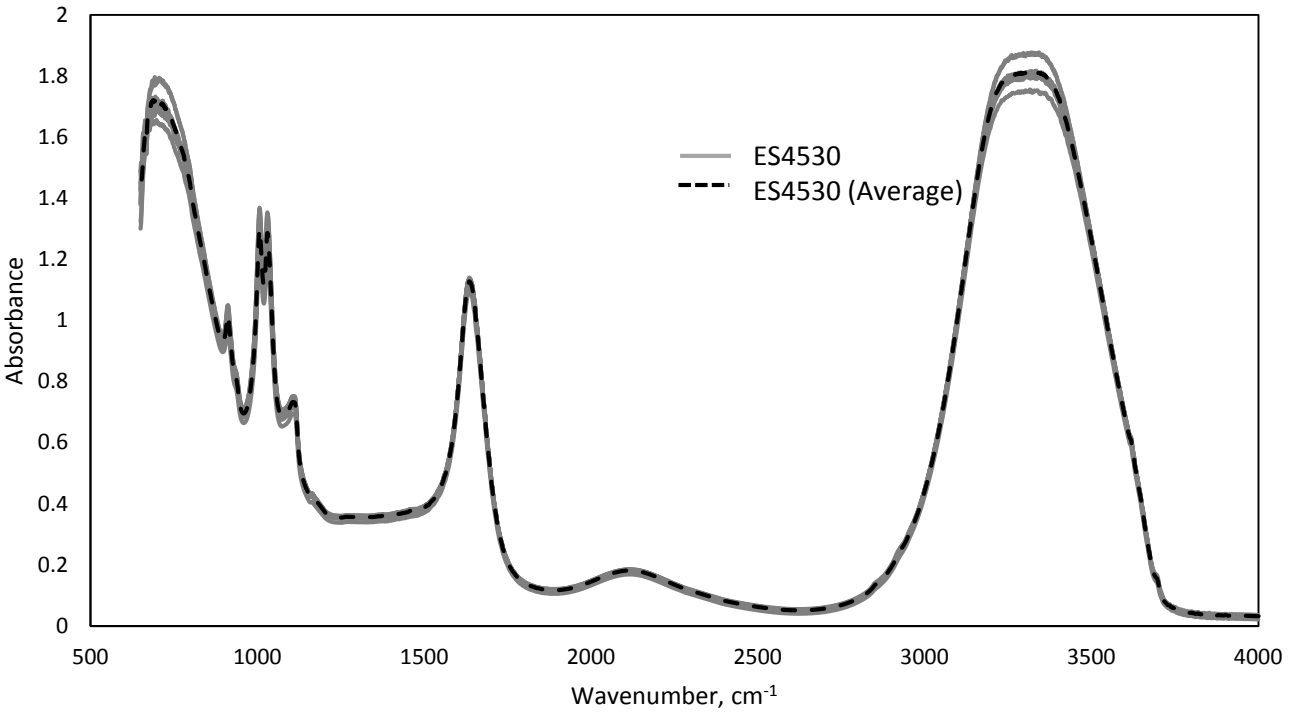

Figure AIII.18. ATR-FTIR spectra of ES4530 in the 4000 to 700 cm-1 region. Each individual spectrum is shown in gray and the averaged spectrum is represented by the dashed black line.

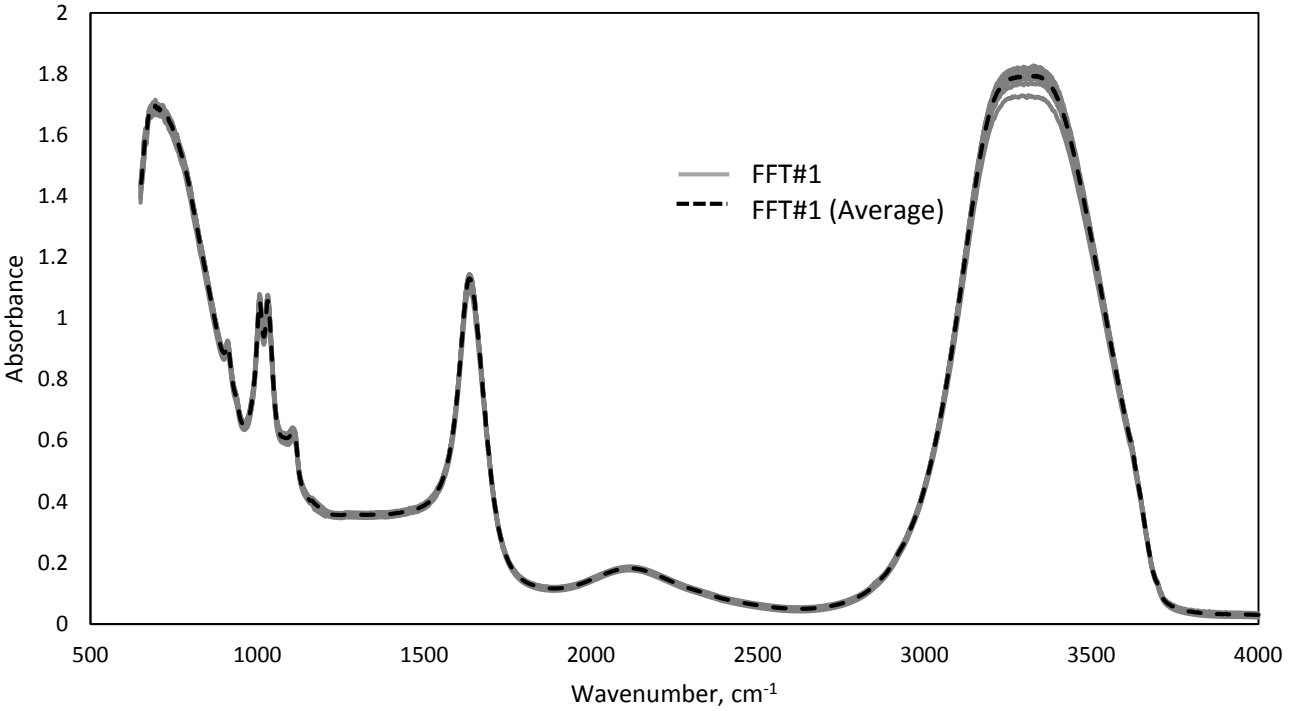

Figure AIII.19. ATR-FTIR spectra of FFT#1 in the 4000 to 700 cm-1 region. Each individual spectrum is shown in gray and the averaged spectrum is represented by the dashed black line.

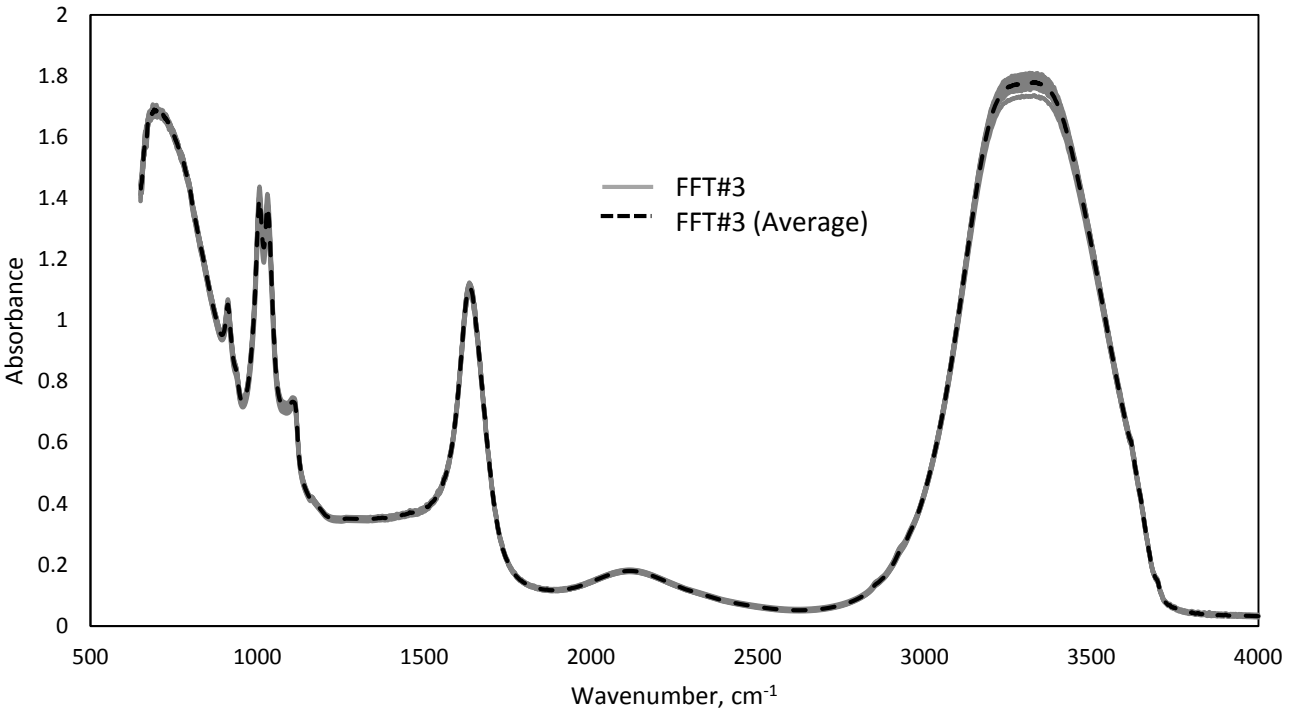

Figure AIII.20. ATR-FTIR spectra of FFT#3 in the 4000 to 700 cm-1 region. Each individual spectrum is shown in gray and the averaged spectrum is represented by the dashed black line.

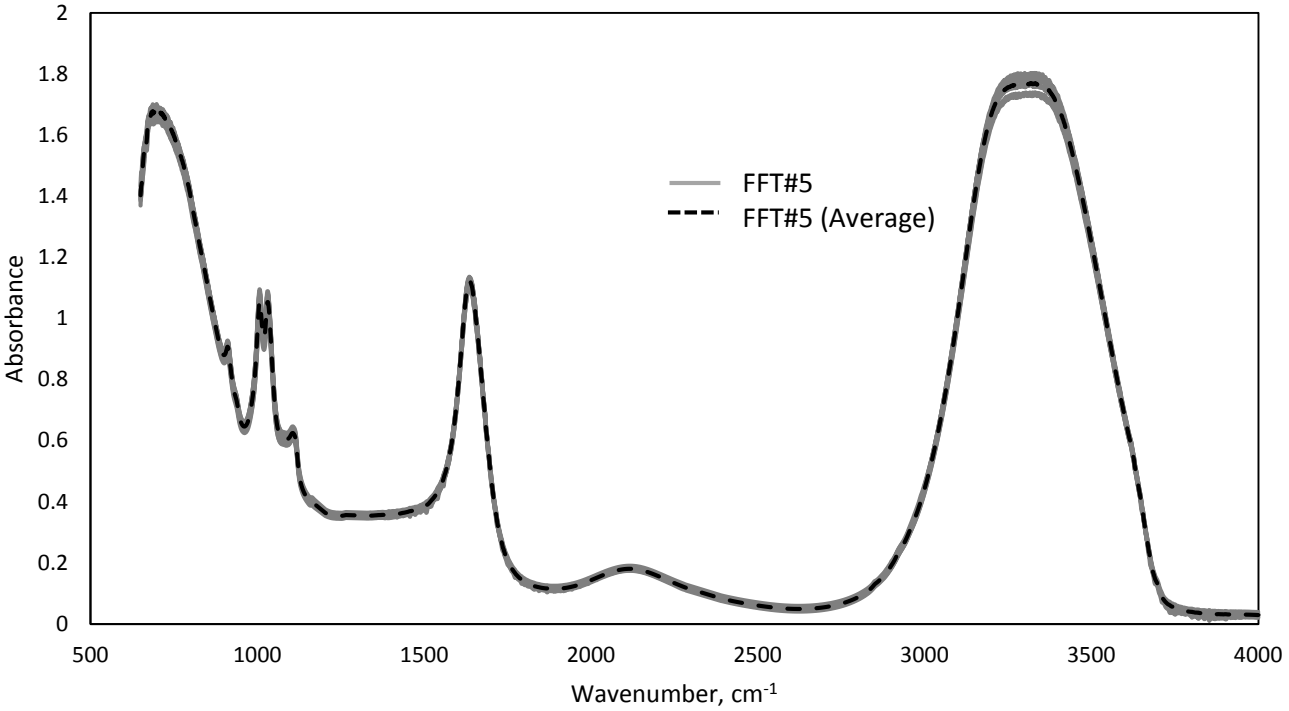

Figure AIII.21. ATR-FTIR spectra of FFT#5 in the 4000 to 700 cm-1 region. Each individual spectrum is shown in gray and the averaged spectrum is represented by the dashed black line.

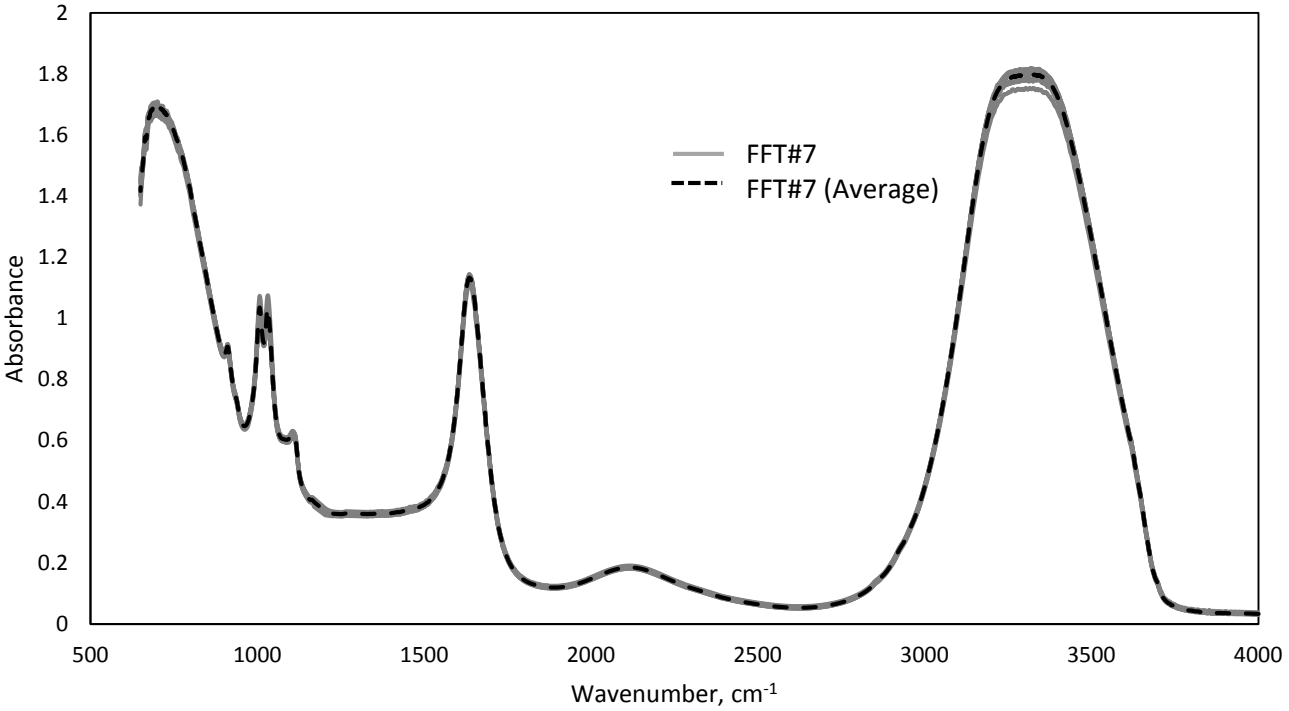

Figure AIII.22. ATR-FTIR spectra of FFT#7 in the 4000 to 700 cm-1 region. Each individual spectrum is shown in gray and the averaged spectrum is represented by the dashed black line.

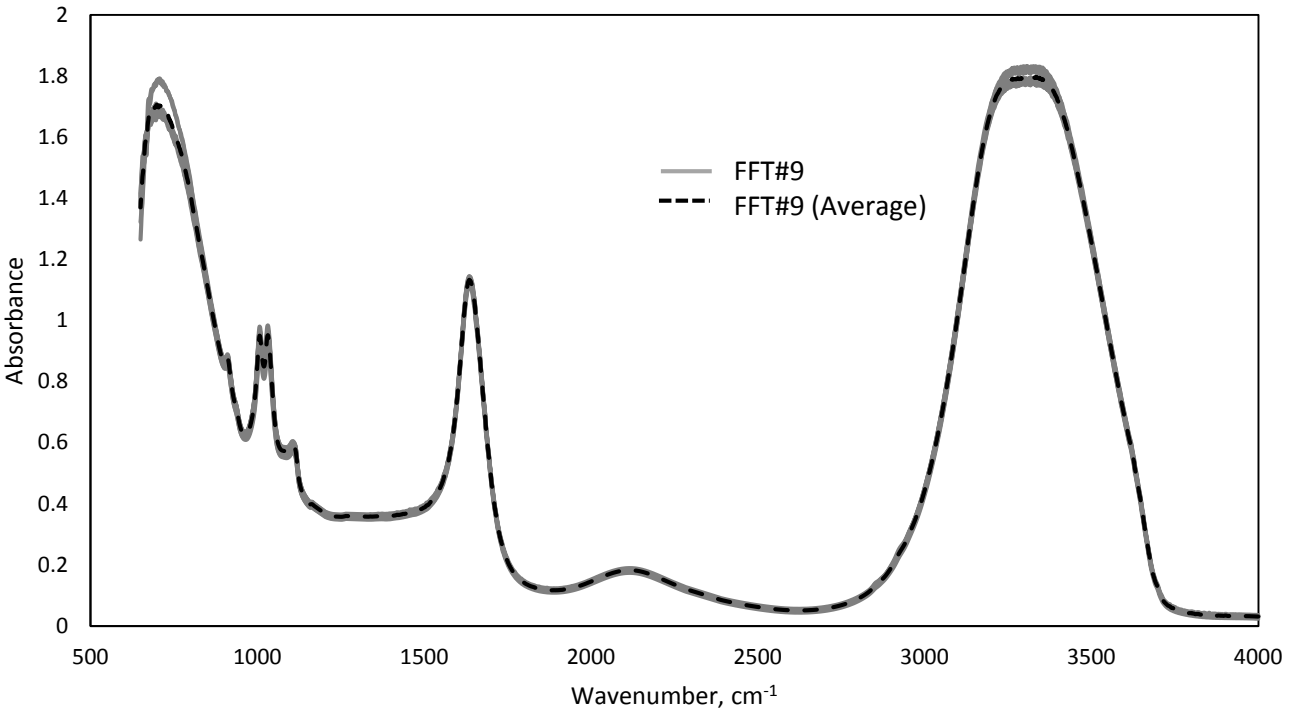

Figure AIII.23. ATR-FTIR spectra of FFT#9 in the 4000 to 700 cm-1 region. Each individual spectrum is shown in gray and the averaged spectrum is represented by the dashed black line.

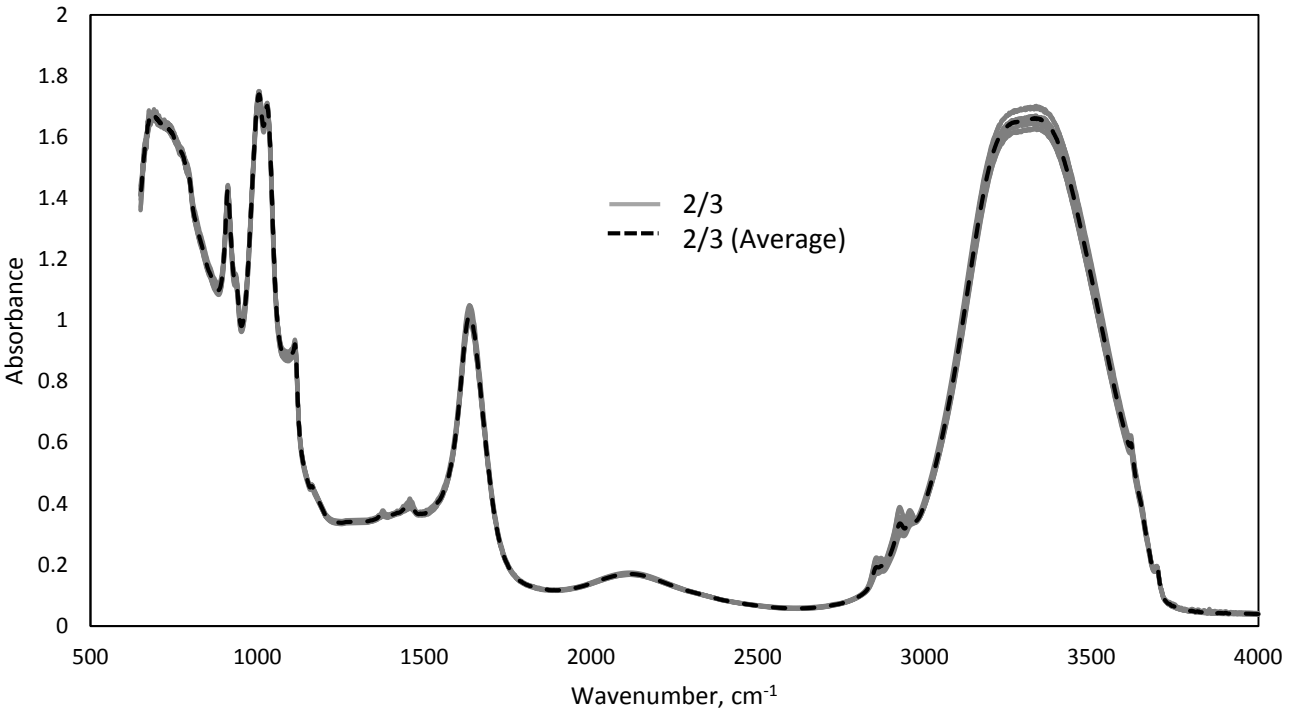

Figure AIII.24. ATR-FTIR spectra of 2/3 in the 4000 to 700 cm-1 region. Each individual spectrum is shown in gray and the averaged spectrum is represented by the dashed black line.

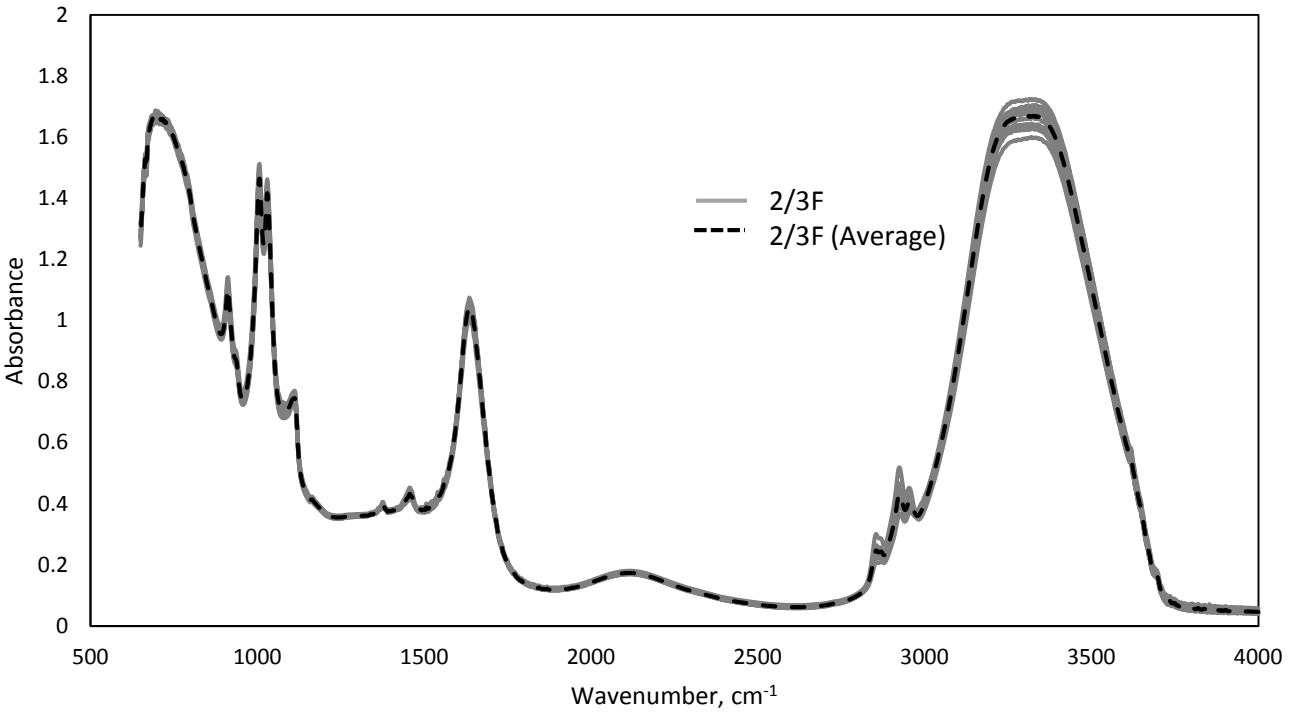

Figure AIII.25. ATR-FTIR spectra of 2/3F in the 4000 to 700 cm-1 region. Each individual spectrum is shown in gray and the averaged spectrum is represented by the dashed black line.

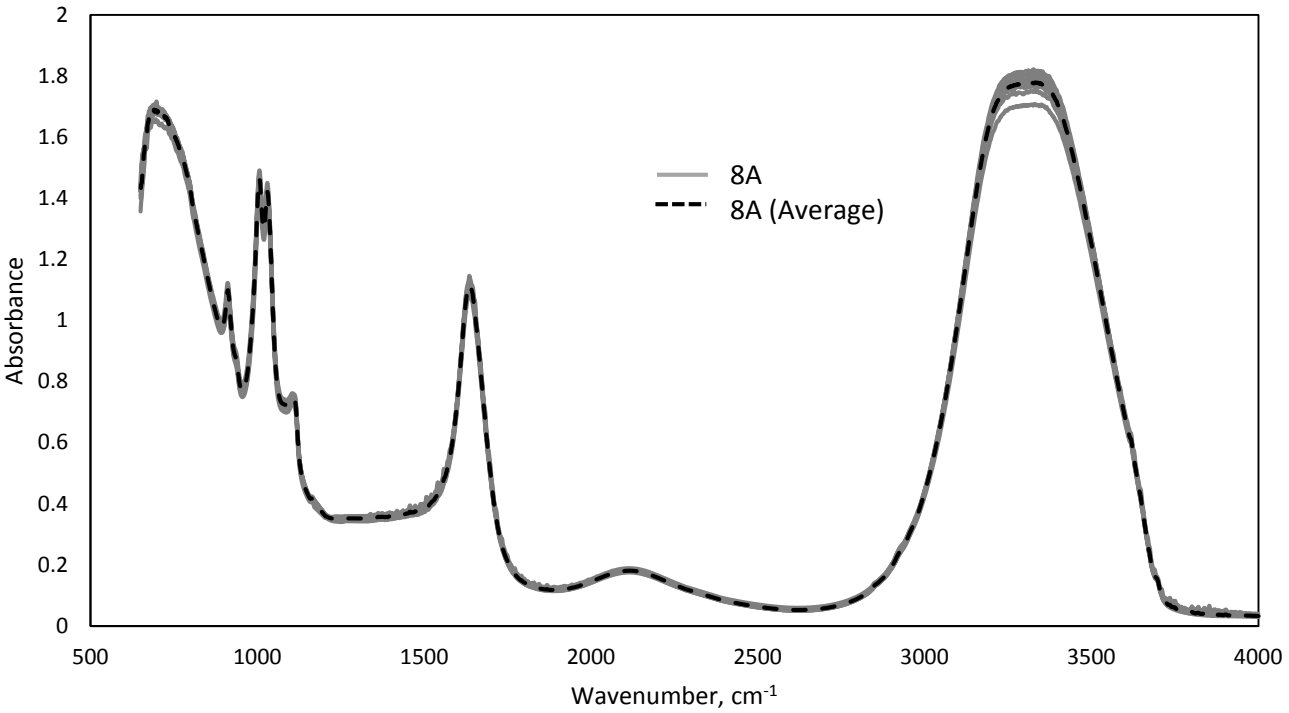

Figure AIII.26. ATR-FTIR spectra of 8A in the 4000 to 700 cm-1 region. Each individual spectrum is shown in gray and the averaged spectrum is represented by the dashed black line.

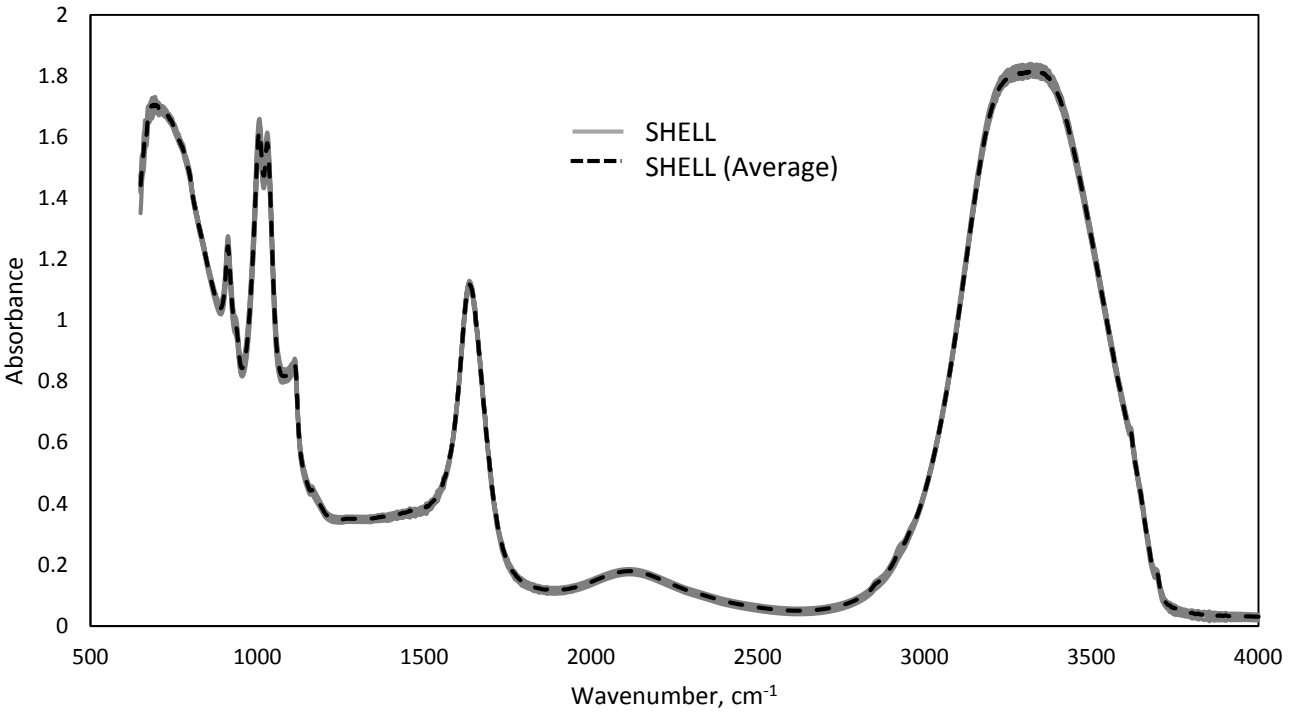

Figure AIII.27. ATR-FTIR spectra of SHELL in the 4000 to 700 cm-1 region. Each individual spectrum is shown in gray and the averaged spectrum is represented by the dashed black line.

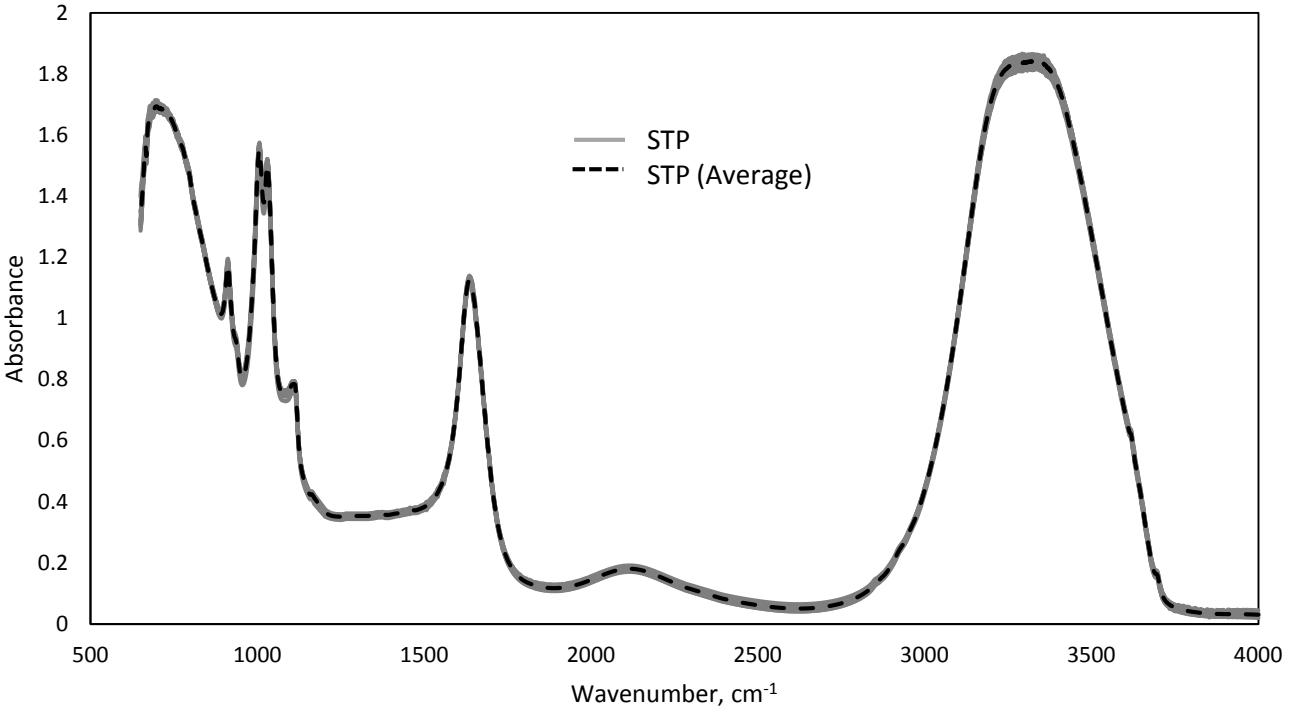

Figure AIII.28. ATR-FTIR spectra of STP in the 4000 to 700 cm-1 region. Each individual spectrum is shown in gray and the averaged spectrum is represented by the dashed black line.

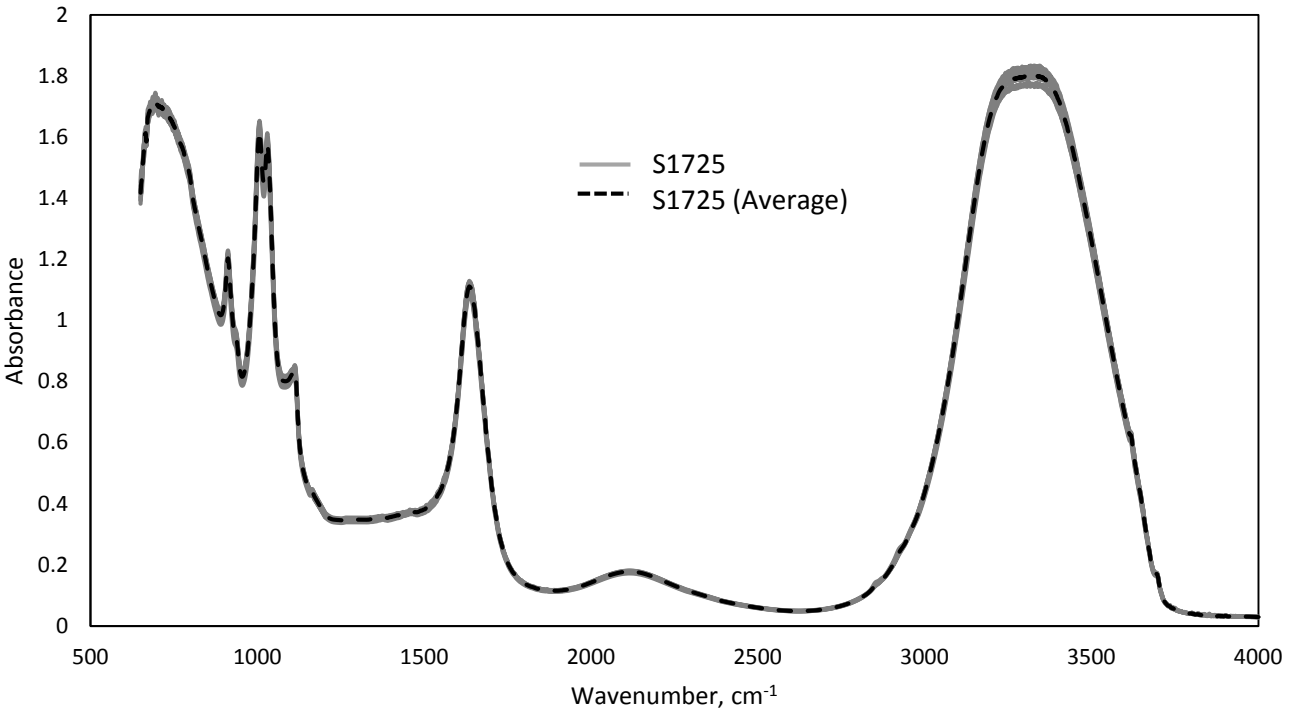

Figure AIII.29. ATR-FTIR spectra of S1725 in the 4000 to 700 cm-1 region. Each individual spectrum is shown in gray and the averaged spectrum is represented by the dashed black line.

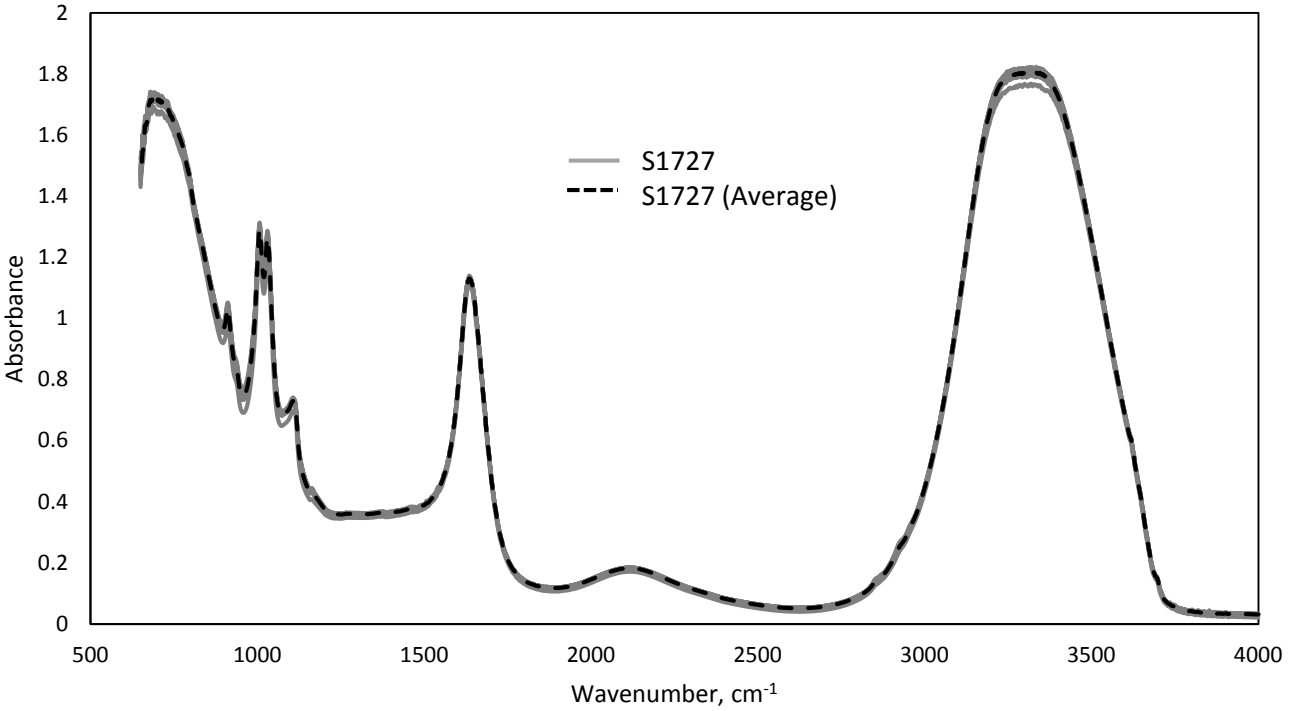

Figure AIII.30. ATR-FTIR spectra of S1727 in the 4000 to 700 cm-1 region. Each individual spectrum is shown in gray and the averaged spectrum is represented by the dashed black line.

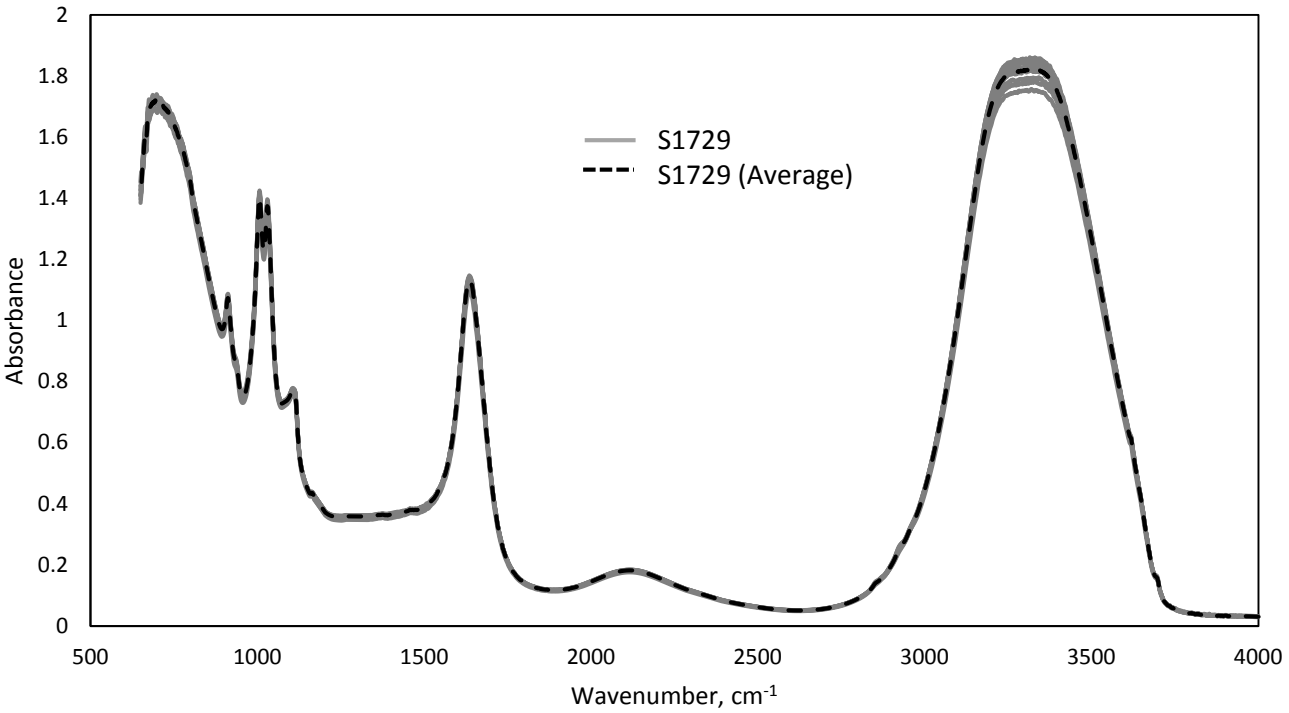

Figure AIII.31. ATR-FTIR spectra of S1729 in the 4000 to 700 cm-1 region. Each individual spectrum is shown in gray and the averaged spectrum is represented by the dashed black line.

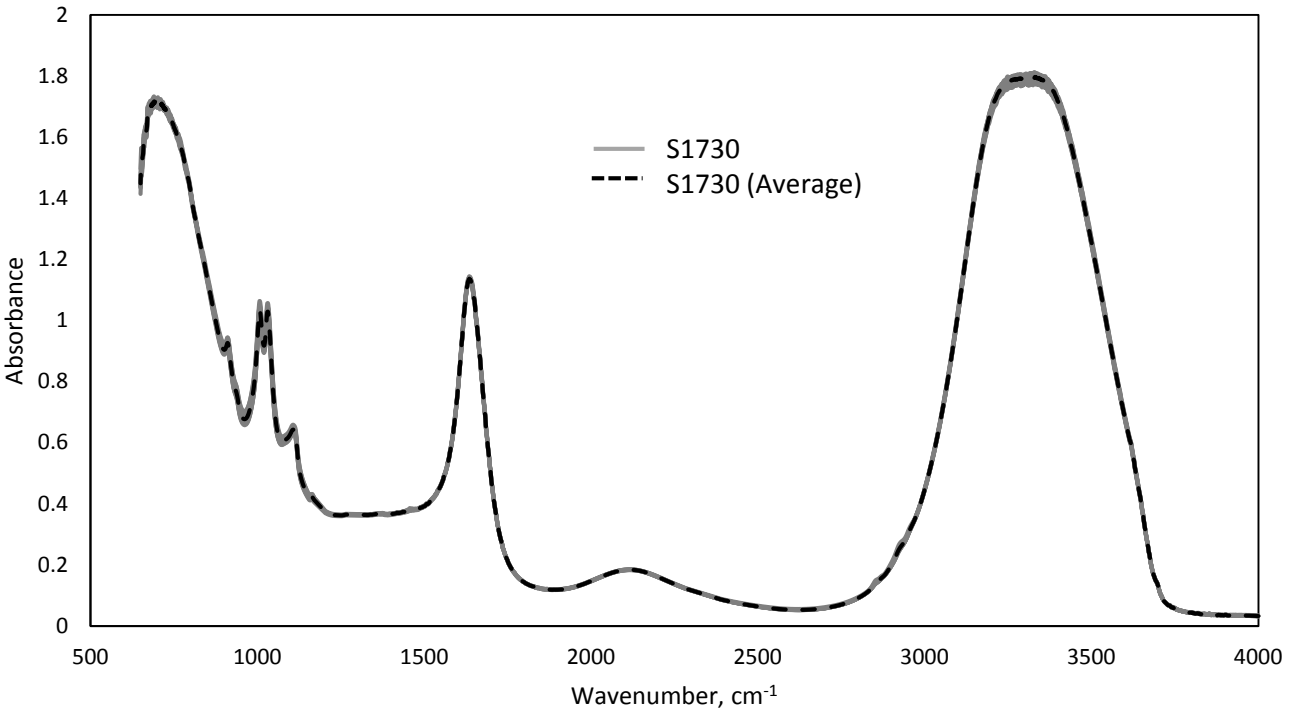

Figure AIII.32. ATR-FTIR spectra of S1730 in the 4000 to 700 cm-1 region. Each individual spectrum is shown in gray and the averaged spectrum is represented by the dashed black line.

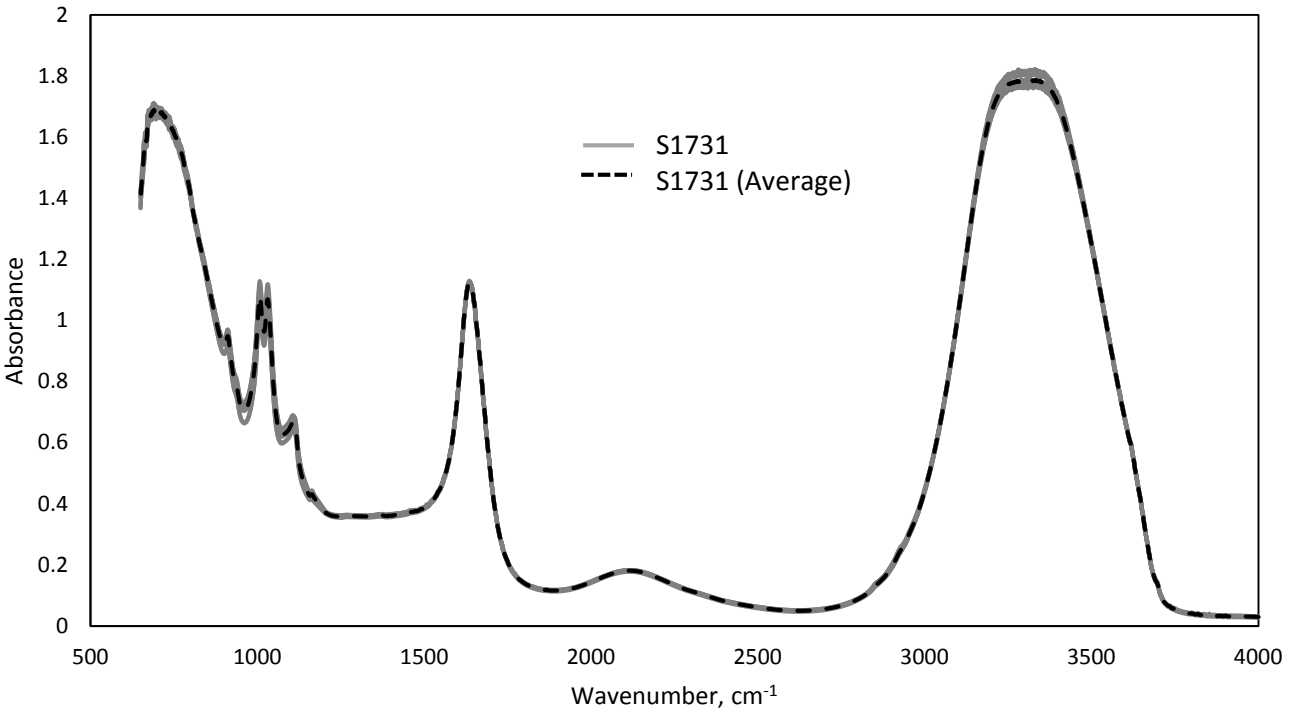

Figure AIII.33. ATR-FTIR spectra of S1731 in the 4000 to 700 cm-1 region. Each individual spectrum is shown in gray and the averaged spectrum is represented by the dashed black line.

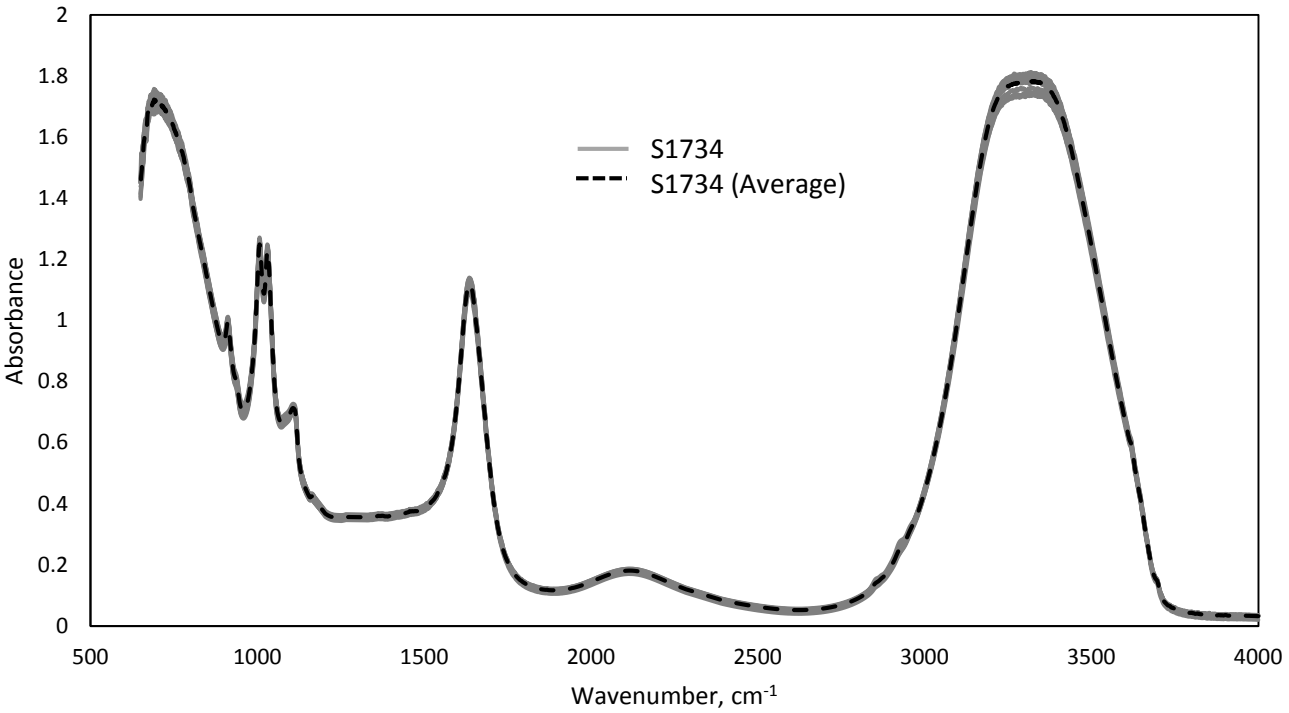

Figure AIII.34. ATR-FTIR spectra of S1734 in the 4000 to 700 cm-1 region. Each individual spectrum is shown in gray and the averaged spectrum is represented by the dashed black line.